AN ABSTRACT OF THE DISSERTATION OF

Bhuvana S. Doddapaneni for the degree of Doctor of Philosophy in Pharmacy presented on June 9, 2016

Title: Development of Micellar and Nanoparticle Structures based on Polyester Diblock Copolymer Platform for the Treatment of Metastatic Tumors

Abstract approved:

Adam W. G. Alani

Poor aqueous solubility of a large number of newly discovered chemical entities is posing a significant challenge for the formulation industry and is delaying their drug development. The number of formulation techniques available to solubilize these poorly soluble molecules is very limited. In addition to that, traditional formulation methods involve the use of surfactants such as Cremophor EL and polysorbate 80 that trigger unwanted toxicities and the lack of proper targeting moieties is further hampering their *in vivo* efficacy. The search for alternate drug delivery systems that overcome these limitations and toxicity issues has therefore led to the use of polyester based diblock copolymers. Polyester based diblock copolymers have garnered tremendous interest in the past two decades for their applications in drug delivery. These block copolymers comprise of a hydrophilic and hydrophobic segments and they readily self-assemble into micellar and nanoparticle structures in aqueous solvents. The ability to modify their surface properties by mixing different copolymers along with their capability to load multiple poorly soluble drug entities into their hydrophobic cores have made them highly sought after in the formulation industry. The polyesters are biodegradable and are approved by the FDA for use in drug delivery purposes. This work encompasses the development of a micellar and a nanoparticle formulation using polyester based diblock copolymers for the delivery of multiple chemotherapeutic agents and imaging applications. The lack of a delivery system

that can achieve substantial lymphatic accumulation has motivated us in developing a poly (ethylene glycol)-*block*-poly (ε-caprolactone) [PEG-*b*-PCL] nanoparticle system that can simultaneously load three drugs at therapeutically relevant concentrations and also achieve significant lymphatic accumulation, courtesy of its modified surface properties. The efficacy of the developed nanoparticle system was evaluated in its ability to reduce the proliferation of melanocytes in metastatic melanoma mice models. We were able to develop locally acting and centrally acting drug loaded nanoparticles that effectively reduced melanocyte proliferation. We then wanted to demonstrate the diagnostic applications of these nanostructures and therefore developed a methoxy poly (ethylene glycol)-*block*-poly (lactic acid) mPEG-*b*-PLA micelle formulation that encapsulates a nerve specific fluorophore BMB. The micellar formulation of BMB achieved significantly higher nerve specific accumulation and fluorescence intensity when compared to its traditional formulation in DMSO and also prevented the unwanted side effects occurring from the formulation excipients. The micellar BMB formulation was a first of its kind as no previous nerve visualization techniques were clinically approved. Finally, we also developed a mPEG-*b*-PLA micellar formulation that encapsulates two drugs that target the major pathways involved in ovarian cancer and prevent tumor progression by exhibiting synergistic effects. The combination therapy proved more beneficial in reducing the tumor burden in animal models compared to the individual drugs and also reduced the development of drug resistance by inhibiting multiple pathways.

We have thus effectively demonstrated the therapeutic and diagnostic applications of micellar and nanoparticle platforms developed from polyester based diblock copolymers in treating metastatic diseased states.

Development of Micellar and Nanoparticle Structures based on Polyester Diblock Copolymer Platform for the Treatment of Metastatic Tumors

by

Bhuvana S. Doddapaneni

A DISSERTATION

submitted to

Oregon State University

in partial fulfillment of

the requirements for the

degree of

Doctor of Philosophy

Presented June 9, 2016

Commencement June 2017

Doctor of Philosophy dissertation of Bhuvana S. Doddapaneni presented on June 9, 2016.

APPROVED:

Major Professor, representing Pharmacy

Dean of the College of Pharmacy

Dean of the Graduate School

I understand that my dissertation will become part of the permanent collection of Oregon State University libraries. My signature below authorizes the release of my dissertation to any reader upon request.

Bhuvana S. Doddapaneni, Author

ACKNOWLEDGEMENTS

It would be highly unfair on my part to only mention a thank you note for my advisor Dr Adam W. G. Alani. I learnt in leaps and bounds both personally as well as professionally in my journey through graduate school and I firmly believe that none of this would have been possible without your support. I feel privileged to be graduating from your lab and I would like to extend my heartfelt gratitude for being patient with me during tough times and for guiding me throughout. A special mention of thanks to Dr Deepa Rao for all the help and guidance in scientific writing and publishing.

I would like to thank my committee members Dr Oleh Taratula, Dr Mark Christensen, Dr Arup Indra and Dr Julie Greenwood for providing me with valuable insights and for guiding me in completing my projects. I would like to also acknowledge Olena for our collaboration project. Getting through graduate school becomes easier with friendly colleagues around. Thank you Canan, Duc, Sharmin, Adel and Jeff for making the journey less stressful.

I would specially like to acknowledge Debra Peters for her support throughout my graduate program and also the College of Pharmacy for providing financial support.

A special shout out to my dad, mom, and brother for always being there during the tough times.

Last but not the least, I have a huge list of friends to thank without whom I would have never made this far. Thank you Vijay, Ramya, and a few others for constantly motivating me and all others who have patiently supported me through all these years. Also, thanks to Cynthia Jain for her efforts in proofreading the dissertation.

CONTRIBUTION OF AUTHORS

Chapter 1

Written by Bhuvana S. Doddapaneni with editing help from Dr Adam Alani.

Chapter 2

Dr Adam Alani and Bhuvana S. Doddapaneni designed majority of the experiments with expert suggestions about animal models from Dr Arup Indra. Bhuvana S. Doddapaneni worked on most of the experiments with help from Sergiy in isolating the lymph nodes and staining them accordingly. Sharmin was responsible for breeding the melanoma models. Dr Deepa Rao helped with suggestions and in preparing the manuscript. Dr Raid G. Alany provided valuable inputs throughout the project.

Chapter 3

The experiments were designed by Dr Adam Alani in collaboration with Dr Summer Gibbs. Kayla M. Hackmann and Bhuvana S. Doddapaneni did majority of the work and are both listed as equal contributors to this project. Igor helped with the cell work. Kayla and Connor did most of the animal work.

Chapter 4

The manuscript was written by Bhuvana S. Doddapaneni and the experiments were planned together with Dr Adam Alani. Kinser Reed helped with *in vitro* cell viability studies. Adel helped with the animal work. Dr Deepa provided valuable inputs and was actively involved in preparing the manuscript with Bhuvana S. Doddapaneni.

Chapter 5

Written by Bhuvana S. Doddapaneni and edited by Dr Adam Alani.

TABLE OF CONTENTS

Page

TABLE OF CONTENTS (Continued)

TABLE OF CONTENTS (Continued)

TABLE OF CONTENTS (Continued)

LIST OF FIGURES

LIST OF FIGURES (Continued)

LIST OF TABLES

DEDICATION

I would like to dedicate this dissertation to my family for their constant support and encouragement throughout the journey.

CHAPTER 1

INTRODUCTION

Bhuvana S. Doddapaneni

1.1 INTRODUCTION TO POLYESTER DIBLOCK COPOLYMERS

Recent advances in polymer chemistry has enabled us to use polymeric platforms for the delivery of poorly soluble substances. Polymers comprise of macromolecular chains obtained from the polymerization of multiple repeating subunits of small molecules called monomers [1]. Some of the naturally occurring polymers include DNA, cellulose and proteins while they can also be synthesized using polymerization reactions [1]. Block copolymers in particular, consisting of two or more blocks of monomers polymerized into a single polymer chain are further classified into diblock and triblock copolymers based on the number of blocks used in the polymerization reaction [2-4]. The diblock copolymers (DBCP) are synthesized using living polymerization reaction wherein a reactive terminal of the first monomer interacts only with a second monomer forming a new reactive terminal that has an additional second monomer attached to it thereby preventing the occurrence of side reactions [5]. The amphiphilic DBCP are composed of hydrophilic (water soluble) and hydrophobic (water insoluble) subunits that spontaneously aggregate into different nanostructures when they come in contact with selective solvents [6]. The ratio of hydrophobic to hydrophilic block length and the molecular weights of the block copolymers are touted to be the primary factors that determine the size and morphology of the nanostructures [7]. This property of the DBCP to form nanostructures upon solvent contact distinguishes them from the other graft or random copolymers. The hydrophobic segment of the DBCP constitutes the core of the nanostructures and acts as a reservoir for solubilizing poorly soluble hydrophobic drugs while the hydrophilic segment forms a shell or corona around the hydrophobic core [7]. The DBCP’s aggregate in an entropically favored mechanism wherein all the hydrophobic blocks with similar properties merge together forming the core while the hydrophilic blocks accumulate around the core forming the corona thereby keeping the free energy at minimum [8]. Polyethylene glycol (PEG) is highly preferred as the hydrophilic subunit in a majority of the amphiphilic DBCP’s although a few studies reported the use of Dextran, chitosan, and poly (N-vinyl pyrrolidone) (PVP) as PEG alternatives [9, 10]. The popularity of PEG can be attributed to its properties such as being non-toxic, having a high chain flexibility and being electrically neutral. PEG has a high aqueous solubility and therefore forms a strong water bound barrier on the nanocarrier’s surface preventing its interactions with opsonins or blood components *in vivo*. This in turn increases the circulation time of the nanocarriers as they go undetected by the reticulo-endothelial system [7]. PEGylation also increases the particle size thereby reducing renal excretion as the larger size of the nanocarriers prevents their glomerular filtration thus further prolonging the circulation time [11]. The nanocarriers also exhibit a small size (10 - 100 nm), courtesy of which they can extravasate through the leaky vasculature found in a large number of tumors and inflamed tissues (Enhanced Permeation and Retention effect) (EPR) thereby limiting drug exposure to healthy tissues and avoiding unwanted side effects [12]. Thus PEGylated nanocarriers can be passively targeted to tumors via the EPR effect [13]. Majority of the hydrophobic core forming polymer blocks belonged to polyesters such as poly(L-lactide) (PLA), poly-ƹ – caprolactone (PCL), and poly(lactide-co-glycolic acid) (PLGA) although other classes such as polyethers, poly amino acids and lipids have also been reported to be used [14] The major advantage of using polyesters is that they undergo hydrolysis *in vivo* and degrade into non-toxic monomers. PLA is FDA approved for its use as a biodegradable polymer while PCL also exhibits good biodegradability and a low toxicity profile [15]. Multiple studies have reported the use of these polyesters as core forming blocks in DBCP’s [16]. These core forming blocks are biocompatible and they self-assemble in aqueous solvents to form nanostructures. Micelles, nanoparticles and polymersomes comprise the majority of nanostructures obtained from DBCP’s upon their solvent exposure [7]. The type of nanostructure obtained is primarily decided by the ratio of hydrophilic to hydrophobic block lengths and molecular weights. Monodisperse micelles are obtained upon aqueous exposure of the DBCP when the molecular weight of the hydrophilic block is higher than that of the hydrophobic block. The copolymer readily undergoes self-assembly and disperses in water to form small uniform micelles spontaneously [17]. Meanwhile if the molecular weight of the hydrophobic block is higher than the hydrophilic block, the polymer becomes more and more water insoluble and therefore cannot undergo self-assembly to form micelles. In this case, an alternate method of preparation such as nanoprecipitation needs to be employed to form nanoparticles with solid-core like properties [18]. DBCP also form polymersomes that can deliver hydrophilic drugs by encapsulating them in the aqueous core and the external bilayer of these polymersomes comprise of DBCP's [7] A vast library of DBCP's can be synthesized by modifying the chemical composition, molecular weight, and architecture of the monomers thereby providing flexibility in the block copolymer design [8]. DBCP's have been highly sought after in the past decade for drug delivery applications because of the ability to design nanocarriers to your preference and also for the wide range of applications that come from these designed nanocarriers.

1.2 MICELLES

Amphiphilic DBCP molecules upon contact with aqueous solvents spontaneously self-assemble into a wide range of nanostructures that have different sizes and shapes. The molecules comprise of a hydrophilic and a hydrophobic head that exhibit different solubilities in aqueous solvents. The DBCP molecules exist in a freely dispersed state in aqueous media at low concentrations of the polymer [14]. Increasing the polymer concentration spontaneously increases the free energy of the system due to the unfavorable interactions occurring between the hydrophobic segments and the surrounding aqueous solvent molecules [14]. When the concentration of the polymer reaches a particular value termed as “critical micellar concentration” (CMC), the amphiphilic molecules self-assemble into colloidal structures called micelles wherein the hydrophobic segments aggregate together to form the core and the hydrophilic segments form the corona thereby minimizing the unfavorable interactions of the core with the aqueous molecules and decreasing the free energy of the system [7,19] The difference in the solubilities of the hydrophilic and the hydrophobic segments drives the process of micellization. There are two components involved in the formation of a micelle, an attractive force that promotes the association of the micelles and a repulsive force that prevents unlimited growth of the formed micelles [17]. It is at the CMC that the process of association begins. The micelles are thermodynamically stable at polymer concentrations above the CMC, while they disassemble spontaneously at concentrations below the CMC [20]. The aggregated molecules that form the micelle are in a dynamic equilibrium with the unimers in the bulk solution promoting a continuous exchange of unimers thereby forming a mobile fluid-like core. [21] The micelles exhibit a core-shell architecture wherein the core is used for solubilizing hydrophobic drugs while the shell is comprised of the hydrophilic segments and protects the core from unwanted interactions with blood components. [21]

Block copolymer micelles usually represent a size range of 10 – 100 nm exhibiting a core-corona architecture. [8, 22] The size of the micelles is majorly governed by the molecular weights of the polymer blocks and the ratios of the hydrophilic to the hydrophobic segments. The micelles have a spherical shape when the hydrophilic block length is larger than the hydrophobic block length while they exhibit non-spherical structures that include rod shaped or lamellae if the hydrophobic block length is larger than the hydrophilic block length [7]. The stability of these micelles is majorly determined based on the CMC of the di-block polymers. Micelles with a lower CMC can withstand dilution to a greater extent and are therefore more stable thermodynamically when compared to micelles with higher CMC values. Multiple techniques such as dye solubilization, surface tension, light scattering and fluorescence have been used in various studies to determine the CMC's of DBCP's [8, 14]. The typical CMC values of diblock copolymers usually ranges from 10^{-6} to 10^{-7}M. There are multiple factors that affect the CMC, but the composition of the core forming blocks exhibit the highest impact on CMC. The core of the micelles acts as a reservoir for solubilizing hydrophobic drugs. Poorly soluble compounds can be incorporated into these hydrophobic cores thereby significantly increasing their aqueous solubilities. The rate of drug release from these micelles can be fine-tuned and is dependent on various factors such as the diffusion and the partition co-efficient of the drugs, their hydrophobicity and the viscosity of the core [23]. The hydrophobic core is surrounded by a corona that comprises of the hydrophilic segments. These segments upon interacting with the aqueous solvents form brush like conformations on the surface that sterically prevent or suppress opsonization by the blood components.

Polymeric micelles can be categorized into three types based on the intermolecular forces governing the separation of the hydrophobic core from the aqueous atmosphere. The first category named "Conventional micelles" involves the formation of micelles by simple hydrophobic interactions between the core and the corona blocks in an aqueous environment [22]. "Polyion complex micelles" comprise the second category wherein electrostatic interactions between two oppositely charged moieties allows for the formation of polymeric micelles [24]. The structure and the size of the micelle coronas formed depend on the strength of the electrostatic and vanderwaals forces. The third category named "Noncovalently connected polymeric micelles" are formed from homopolymer chains that have their core and corona connected non-covalently by interactions such as hydrogen bonding or metal-ligand interactions [25]. The disassembly of these micelles spontaneously upon injecting *in vivo* (dilution) has triggered the interest for developing alternate strategies that are more stable upon dilution. The core and shell crosslinked micelles provide the solution wherein cross linkable groups are synthesized and used in the formation of micelles. These cross linked micelles are resistant to disassembly unless they are triggered by an external or internal stimuli [26]. Micelles can be further classified into passively targeted and actively targeted micelles. Passive targeting involves accumulation of the micelles in the tumor site via the Enhanced Permeation and retention effect (EPR) wherein the micelles courtesy of their size escape through the leaky vasculature and accumulate in the tumor tissue [12]. Actively targeted micelles release the drug cargo only at the target site by means of an internal stimuli such as pH, enzyme release, or targeting moiety or by an external stimuli such as temperature, ultrasound or magnetic field [27, 28]. The use of polyester diblock copolymers for drug delivery has tremendously increased in the past decade because of their biodegradable properties and also being approved by the FDA. PEGylated Poly (lactic) acid (PLA) and PEG-PCL comprise the two majorly used polyester based diblock copolymers for formulating active and passively targeted micelles. A micellar formulation of Paclitaxel (Genexol PM) is showing promising results in clinical trials in the U.S and has already been approved for use in Europe and Korea. Wang et al conjugated a peptide to Maleimide-PEG-PLA that actively targets the $\alpha v\beta 3$ integrin overexpressed in angiogenesis [29]. In another study, Z. Wang et al loaded curcumin in PEG-PLA copolymers by using a pH labile hydrazone bond [30]. This micelle releases the drug through the cleavage of the hydrazine bond specifically at the target tumor site in the presence of acidic pH. Thermosensitive micelles have also been developed wherein the micelles undergo structural changes upon exposure to increased temperature and thereby deposit the cargo at the tumor site. The temperature can be increased by using ultrasound techniques to disrupt the micellar structures [25].

Micelles can be prepared using different techniques but proper care needs to be taken in selecting a procedure for loading hydrophobic drugs as supersaturation can lead to stability issues and precipitation of solubilized drugs. The selection of a drug loading procedure mainly depends on the physicochemical properties of the block copolymer [19]. There are five different techniques majorly used in formulating micelles. The simplest technique of them all is the direct dissolution method in which the polymer and the drugs are dissolved in an aqueous solvent to spontaneously form micelles. This technique is commonly employed in forming Polyion complex micelles and is also useful in the case of moderate hydrophobic copolymers wherein the block copolymer and the drug is fairly soluble in water [24]. Amphiphilic copolymers that are not readily soluble in water need different techniques that employ organic solvents for solubilizing the copolymer or the drug or both. The solvent removal procedure plays a pivotal role in determining the mechanism of micelle formation. Dialysis is the second method in which the polymer and the drug are dissolved in a water-miscible organic solvent and the mixture is placed in a dialysis bag and is dialyzed against water. The slow removal of the organic phase triggers micellization. The solvent casting method involves evaporating the organic solvent to yield a thin polymer-drug film that can be rehydrated with a heated aqueous solvent to form polymeric micelles. This method can be used instead of the dialysis method to yield faster and reproducible micelles [8]. The fourth method involves the use of a water immiscible organic solvent wherein an oil in water (O/W) emulsion technique is employed to form polymeric micelles. Micelles prepared using all of the above methods are required to be sterilized and freeze dried before they can be injected. Therefore, a latest method was developed in which a water/*tert*-butanol (TBA) mixture is used for solubilizing the polymer and the drug. This mixture can be lyophilized to spontaneously remove the solvents thereby forming a polymer-drug cake that can be readily reconstituted in an injectable vehicle [8].

1.3 NANOPARTICLES

Polymeric nanoparticles prepared from amphiphilic diblock copolymers exhibit a core-shell structure similar to the polymeric micelles but the core of the nanoparticles is “frozen” and is composed of dense polymer matrix when compared with a fluid like core in the micelles [7]. The polymeric nanoparticles are usually represented as matrix type solid colloidal particles. The equilibrium conditions for nanoparticles is different from that of the micelles. The nanoparticles with the frozen cores can be formed when the core forming block either has a very high glass transition temperature or it is highly solvent hating with the solvent medium in which the particle is dispersed [31]. The copolymer is usually dissolved in an organic solvent and then mixed into aqueous phase to form nanoparticles that rearrange such that the core comprises of the hydrophobic segments in organic solvent surrounded by the corona or the shell in aqueous solvent [18]. So far, the self-assembly involves free exchange of unimers representing an equilibrium process similar to that of the micelles. When the organic solvent is evaporated from the system by substituting with an aqueous solvent, the volume fraction of the organic solvent reduces and reaches a critical volume fraction wherein the hydrophobic segment becomes glass. This state of the core is considered “frozen” and the free exchange of block copolymer molecules is not allowed after this stage [32]. The formation of nanoparticles can be kinetically controlled using several factors such as the solvent contents, pH and temperature. The molecular weight of the hydrophobic block needs to be longer than the hydrophilic block in order to maintain a “frozen” state [7]. The natural polymers that can form polymeric nanoparticles include Chitosan, Gelatin, and Sodium alginate while a large number of synthetic polymers have also been synthesized for making nanoparticles [10]. The corona of these synthetic nanoparticles is usually made of hydrophilic segments such as PEG, PVP, or polysaccharides while the core is usually made up of hydrophobic segments that include polyesters like PLA, PLGA, PCL and poly(alkyl cyanoacrylate) PACA, polyglycolides (PGA), poly malic acid, and poly(cyano acrylate) PCA [32,33]

The typical size range of polymeric nanoparticles varies from 50 – 200 nm and it varies based on the properties of the block copolymers and the kinetic control variables involved in their preparation [33]. The size ratio of the core to the shell dictates the morphology of the nanoparticles into either “crew-cut” or the “core-corona” type [7]. Poorly soluble drug moieties can be incorporated into the core of the nanoparticles at therapeutically relevant concentrations. The drug moieties can be entrapped, dissolved, encapsulated, chemically bound or adsorbed inside the polymer matrix. The surface of the nanoparticles has been modified to prepare different types of nanoparticles. In one study, fibronectin targeting CLT-1 peptide was conjugated to the PEG-PLA nanoparticle to actively target tumors expressing fibronectin [34]. In another study, Nguyen-Van Cuong conjugated folic acid to the PEG chain of a PEG-PCL copolymer to target breast and ovarian cancers [35]. Stimuli responsive nanoparticles have also been extensively used to deliver cargo to specific tumor sites [36].

Polymeric nanoparticles are usually prepared by the dispersion of drug in preformed polymers. There are six different techniques that can be used to form polymeric nanoparticles. The first technique “Solvent evaporation” involves two steps wherein an emulsion of the polymer solution is formed in the first step and the polymer solvent is evaporated to form the nanoparticles in the second step [37]. This method is particularly suitable for lipophilic drugs. The second method “nanoprecipitation or the solvent displacement” method involves the solubilization of the polymer and the drug in a water miscible organic solvent, which is then added to an aqueous phase [18]. The organic solvent diffuses into the aqueous phase forming nanoparticles that are stabilized by surfactant molecules. The third method “Emulsification/solvent diffusion” involves saturation of the polymer dissolved in partially water soluble solvent with water to ensure thermodynamic equilibrium [37]. The resulting polymer-water saturated solvent phase is emulsified in an aqueous solution to form the nanoparticles. This technique yields high encapsulation efficiencies and produces reproducible batches. The fourth technique named “salting out” depends on the separation of water miscible solvents by using the salting out effect from aqueous solutions. The polymer drug mixture dissolved in a solvent is emulsified into an aqueous gel that is further diluted with water to separate the organic phase and form nanostructures. The fifth method “dialysis” is a simple method in which the polymer dissolved in an organic solvent is placed in a dialysis tube with a MWCO and is dialyzed against a non-solvent [37]. All of the above techniques involve the use of an organic solvent in different stages of the formulation and therefore to avoid organic solvents, a sixth technique “supercritical fluid technology” was developed wherein the solute is dissolved in a super critical fluid and the solution is rapidly expanded across a nozzle into air resulting in homogenous nucleation and well-dispersed particles [37].

1.4 APPLICATIONS OF MICELLES AND NANOPARTICLES

Amphiphilic diblock copolymers spontaneously self-assemble into various nanostructures upon contact with aqueous solvents. Micelles and nanoparticles have a lot of similar applications and therefore will be referred to as nanostructures hereafter for the rest of this discussion.

Polyester based diblock copolymers usually have PEG as the hydrophilic segment and polyester as the hydrophobic segment. PEGylation is the process of covalently linking PEG chain to other molecules thereby encapsulating the molecules and providing a vast range of advantages. The PEG chains form brush like conformations around the core of the micelles and nanoparticles and protect the encapsulated cargo from interactions with blood components, preventing their recognition by the reticulo endothelial system (RES) thereby prolonging their circulation times [9]. The PEG coating also prevents the opsonization of these micelles and nanoparticles. The increased circulation times of these nanoplatforms help achieve increased accumulations in the target tissue. The size of the micelles range from 10 – 100 nm while the nanoparticles belong to the 50 – 200 nm size range [7]. These nanostructures have a molecular weight > 50 kDa thereby avoiding renal excretion and also are small enough (< 200 nm) to bypass the filtration by interendothelial cells in the spleen. These micelles and nanoparticles can be passively targeted to the tumor site courtesy of their nano size that they can easily extravasate through the leaky vasculature associated with the diseased states. This phenomenon termed the “Enhanced Permeation and Retention” effect (EPR) has been thoroughly exploited in targeting polymeric micelles and nanoparticles to various tumor states [13].

The core of the nanostructures usually comprises of a hydrophobic block that acts as a reservoir for the solubilization of poorly soluble drugs. This phenomenon of incorporating poorly soluble drugs into hydrophobic environments with greater solubility in a solution is termed solubilization [38]. The therapeutic potential of many drug candidates could not be elucidated because of solubility issues and therefore improving their aqueous solubilities by incorporating them in polymeric nanostructures can help unwind their tremendous potential. The formulation process of these nanostructures involves complete evaporation of the organic solvents and therefore they exhibit a better safety profile when compared with existing formulations. The ability of these nanostructures to deposit the cargo in the tumor site further reduces the systemic toxicity as the healthy tissues are not being exposed to the chemotherapeutic drugs [19]. The nanostructures retain the drug for a longer period of time, courtesy of crosslinked structures and increased lengths of the hydrophobic segments and therefore help maintain a sustained or delayed release profile of the encapsulated drugs rather than dose dumping into systemic circulation. This in turn improves the bioavailability of these drugs and therefore the drugs exhibit a better pharmacokinetic profile [39]. The maximum tolerated doses of the encapsulated drugs have been reported to increase by at least 3 fold upon incorporation in these nanostructures when compared to the free drug indicating the ability to deliver much higher doses of the drugs with much less toxicity [15].

The nanostructures provide us with a platform that can be modified according to our preference for drug delivery purposes. This flexibility in designing various delivery platforms makes the block copolymers a popular research topic [6]. The surface charge on the nanostructures can be controlled by modifying the mixing ratios of various block copolymers involved in the nanostructure formation. The charged nanostructures along with their nano size range can be used to effectively target lymphatic system [33]. Surface modifications also include attaching a ligand that is overexpressed in a particular diseased state such that these nanostructures are specifically targeted to that particular tumor thereby achieving active targeting. Multiple studies have reported the use of polyester based nanostructures in targeting specific diseased states by attaching the corresponding ligands or chemo attractants [34]. A wide range of stimuli sensitive polymeric nanostructures have been developed in the past decade that employ either external or internal stimuli for releasing the cargo from the nanostructures. The internal stimuli-sensitive structures release the cargo based on changes in the pH, or redox potential of the environment while the external stimuli include the use of light-sensitive and ultrasound sensitive polymeric structures [25]. These features further increase the potential of these delivery platforms in actively targeting the drug cargo to the tumor site.

The major drawback of the current chemotherapeutic strategies is the development of drug resistance upon treatment with available formulations. Tumors upregulate multiple alternate pathways when one particular pathway is targeted by using a chemotherapeutic agent [20]. The lack of a delivery system that can deliver multiple drugs at therapeutic concentrations has been a long standing problem in cancer chemotherapy. Newer treatment strategies were developed that involved the use of multiple drugs that act synergistically on different mechanisms involved in a particular tumor and prevent their progression [40]. The nanostructures formed from the polyester diblock copolymers have a tremendous potential in solubilizing these multiple drugs and also in delivering them to tumor specific regions via active and passive targeting. The development of these nanostructures have opened up the avenues for combination therapy as the hydrophobic cores of these structures provide an excellent environment for solubilizing multiple drugs at therapeutically relevant concentrations [33,41]. The ability to co-deliver multiple drugs simultaneously has led to development of formulations that could effectively suppress the drug resistance in multiple tumor subtypes. These structures can also be modified for site specific release of their cargo and therefore provide an excellent drug delivery platform for combination therapy [25].

Finally, the nanostructures can also be used for diagnostic applications wherein a fluorophore or a contrast agent can be incorporated into the core of these structures and thereby can be effectively delivered to the target sites [42]. There is currently no imaging technique that is clinically approved to improve nerve visualization in surgical treatments. The ability of these nanostructures to load significant amounts of the dye/fluorophore into their hydrophobic core regions along with their long circulation properties help localize the dye in these nerves and provides excellent nerve visualization that in turn makes surgical operations easier and with fewer instances of nerves getting damaged [43,44].

1.5 REFERENCES

[1] X. Song, Q. Ma, Z. Cai, R. Tanaka, T. Shiono and R. B. Grubbs, *Macromol Rapid Commun*, 2016, **37**, 227-231.
[2] A. B. Kutikov and J. Song, *ACS Biomater Sci Eng*, 2015, **1**, 463-480.
[3] T. Wang, X. Tang, J. Han, Y. Ding, W. Guo and M. Pei, *Macromol Biosci*, 2016, **16**, 774-783.
[4] D. G. Abebe, R. Kandil, T. Kraus, M. Elsayed, O. M. Merkel and T. Fujiwara, *Macromol Biosci*, 2015, **15**, 698-711.
[5] A. K. Mohanty, U. Jana, P. K. Manna and G. P. Mohanta, *Prog Biomater*, 2015, **4**, 89-100.
[6] M. Muller and D. W. Sun, *Phys Rev Lett*, 2013, **111**, 267801.
[7] K. Letchford and H. Burt, *Eur J Pharm Biopharm*, 2007, **65**, 259-269.
[8] G. Gaucher, M. H. Dufresne, V. P. Sant, N. Kang, D. Maysinger and J. C. Leroux, *J Control Release*, 2005, **109**, 169-188.
[9] R. Gref, M. Luck, P. Quellec, M. Marchand, E. Dellacherie, S. Harnisch, T. Blunk and R. H. Muller, *Colloids Surf B Biointerfaces*, 2000, **18**, 301-313.
[10] A. Kumar, A. Vimal and A. Kumar, *Int J Biol Macromol*, 2016, DOI: 10.1016/j.ijbiomac.2016.05.054.
[11] F. Ahmed and D. E. Discher, *J Control Release*, 2004, **96**, 37-53.
[12] J. I. Hare, T. Lammers, M. B. Ashford, S. Puri, G. Storm and S. T. Barry, *Adv Drug Deliv Rev*, 2016, DOI: 10.1016/j.addr.2016.04.025.
[13] M. Mullner, D. Mehta, C. J. Nowell and C. J. Porter, *Chem Commun (Camb)*, 2016, DOI: 10.1039/c6cc00447d.
[14] S. R. Croy and G. S. Kwon, *Curr Pharm Des*, 2006, **12**, 4669-4684.
[15] G. Gaucher, R. H. Marchessault and J. C. Leroux, *J Control Release*, 2010, **143**, 2-12.
[16] K. Sakai-Kato, N. Nishiyama, M. Kozaki, T. Nakanishi, Y. Matsuda, M. Hirano, H. Hanada, S. Hisada, H. Onodera, H. Harashima, Y. Matsumura, K. Kataoka, Y. Goda, H. Okuda and T. Kawanishi, *J Control Release*, 2015, **210**, 76-83.
[17] M. Yokoyama, *J Drug Target*, 2014, **22**, 576-583.
[18] T. Govender, S. Stolnik, M. C. Garnett, L. Illum and S. S. Davis, *J Control Release*, 1999, **57**, 171-185.
[19] M. Jones and J. Leroux, *Eur J Pharm Biopharm*, 1999, **48**, 101-111.
[20] H. Cho, T. C. Lai, K. Tomoda and G. S. Kwon, *AAPS PharmSciTech*, 2015, **16**, 10-20.
[21] H. Danafar, S. Davaran, K. Rostamizadeh, H. Valizadeh and M. Hamidi, *Adv Pharm Bull*, 2014, **4**, 501-510.
[22] R. Thipparaboina, R. B. Chavan, D. Kumar, S. Modugula and N. R. Shastri, *Colloids Surf B Biointerfaces*, 2015, **135**, 291-308.
[23] Y. Li, X. R. Qi, Y. Maitani and T. Nagai, *Nanotechnology*, 2009, **20**, 055106.
[24] H. J. Kim, M. Zheng, K. Miyata and K. Kataoka, *Methods Mol Biol*, 2016, **1364**, 89-103.

[25] S. Guragain, B. P. Bastakoti, V. Malgras, K. Nakashima and Y. Yamauchi, *Chemistry*, 2015, **21**, 13164-13174.

[26] Y. Zhao, *Langmuir*, 2016, DOI: 10.1021/acs.langmuir.6b01162.

[27] M. C. Jones, M. Ranger and J. C. Leroux, *Bioconjug Chem*, 2003, **14**, 774-781.

[28] X. Zeng, X. Zhou, M. Li, C. Wang, J. Xu, D. Ma and W. Xue, *J Mater Sci Mater Med*, 2015, **26**, 234.

[29] Y. Wang, P. Liu, Y. Duan, X. Yin, Q. Wang, X. Liu, X. Wang, J. Zhou, W. Wang, L. Qiu and W. Di, *Biomaterials*, 2014, **35**, 983-992.

[30] Z. Wang, C. Chen, Q. Zhang, M. Gao, J. Zhang, D. Kong and Y. Zhao, *Eur J Pharm Biopharm*, 2015, **90**, 53-62.

[31] R. Z. Xiao, Z. W. Zeng, G. L. Zhou, J. J. Wang, F. Z. Li and A. M. Wang, *Int J Nanomedicine*, 2010, **5**, 1057-1065.

[32] K. S. Shalaby, M. E. Soliman, G. Bonacucina, M. Cespi, G. F. Palmieri, O. A. Sammour, A. A. El Shamy, L. Illum and L. Casettari, *Pharm Res*, 2016, DOI: 10.1007/s11095-016-1939-8.

[33] B. S. Doddapaneni, S. Kyryachenko, S. E. Chagani, R. G. Alany, D. A. Rao, A. K. Indra and A. W. Alani, *J Control Release*, 2015, **220**, 503-514.

[34] B. Zhang, S. Shen, Z. Liao, W. Shi, Y. Wang, J. Zhao, Y. Hu, J. Yang, J. Chen, H. Mei, Y. Hu, Z. Pang and X. Jiang, *Biomaterials*, 2014, **35**, 4088-4098.

[35] M. Alibolandi, K. Abnous, F. Sadeghi, H. Hosseinkhani, M. Ramezani and F. Hadizadeh, *Int J Pharm*, 2016, **500**, 162-178.

[36] Y. Zhu and L. Liao, *J Nanosci Nanotechnol*, 2015, **15**, 4753-4773.

[37] C. P. Reis, R. J. Neufeld, A. J. Ribeiro and F. Veiga, *Nanomedicine*, 2006, **2**, 8-21.

[38] S. Biswas, P. Kumari, P. M. Lakhani and B. Ghosh, *Eur J Pharm Sci*, 2016, **83**, 184-202.

[39] N. Pippa, S. Pispas and C. Demetzos, *Curr Pharm Des*, 2016, **22**, 2788-2795.

[40] H. C. Shin, A. W. Alani, H. Cho, Y. Bae, J. M. Kolesar and G. S. Kwon, *Mol Pharm*, 2011, **8**, 1257-1265.

[41] X. Gao, B. Wang, Q. Wu, X. Wei, F. Zheng, K. Men, H. Shi, N. Huang, Y. Wei and C. Gong, *J Biomed Nanotechnol*, 2015, **11**, 578-589.

[42] V. P. Torchilin, *Q J Nucl Med*, 1997, **41**, 141-153.

[43] K. M. Hackman, B. S. Doddapaneni, C. W. Barth, I. H. Wierzbicki, A. W. Alani and S. L. Gibbs, *Mol Pharm*, 2015, **12**, 4386-4394.

[44] L. Gibot, A. Lemelle, U. Till, B. Moukarzel, A. F. Mingotaud, V. Pimienta, P. Saint-Aguet, M. P. Rols, M. Gaucher, F. Violleau, C. Chassenieux and P. Vicendo, *Biomacromolecules*, 2014, **15**, 1443-1455.

CHAPTER 2

A three-drug nanoscale drug delivery system designed for preferential lymphatic uptake for the treatment of metastatic melanoma

Bhuvana S. Doddapaneni, Sergiy Kyryachenko, Sharmeen E. Chagani, Raid G. Alany ,
Deepa A. Rao, Arup K. Indra, Adam W. G. Alani

Journal of Controlled Release

Published 11 November 2015

220 (2015): 503 – 514

DOI: 10.1016/j.jconrel.2015.11.013

2.1 ABSTRACT

Metastatic Melanoma has a high mortality rate due to lymphatic progression of the disease. Current treatment is surgery followed by radiation and intravenous chemotherapy. However, drawbacks for current chemotherapeutics lie in the fact that they develop resistance and do not achieve therapeutic concentrations in the lymphatic system. We hypothesize that a three-drug nanoscale drug delivery system, tailored for lymphatic uptake, administered subcutaneously, will have decreased drug resistance and therefore offer better therapeutic outcomes. We prepared and characterized nanoparticles (NP) with docetaxel, everolimus, and LY294002 in polyethyleneglycol-*block*-poly(ε-caprolactone) (PEG-PCL) polymer with different charge distributions by modifying the ratio of anionic and neutral end groups on the PEG block. These NP are similarly sized (~ 48nm), with neutral, partially charged, or fully charged surface. The NP are able to load ~ 2mg/mL of each drug and are stable for 24 h. The NP are assessed for safety and efficacy in two transgenic metastatic melanoma mouse models. All the NP were safe in both models based on general appearance, weight changes, death, and blood biochemical analyses. The partially charged NP are most effective in decreasing the number of melanocytes at both the proximal (sentinel) lymph node (LN) and the distal LN from the injection site. The neutral NP are efficacious at the proximal LN, while the fully charged NP have no effect on either LN. Thus, our data indicates that the NP surface charge and lymphatic efficacy are closely tied to each other and the partially charged NP have the highest potential in treating metastatic melanoma.

2.2 INTRODUCTION

Melanoma is the deadliest form of skin cancer with a very high mortality rate.[1] The standard treatment for early stage diagnosis is surgical removal of the tumor and for late stage surgery followed by radiation and chemotherapy. Tumor metastasis is the major reason for high mortality rates in melanoma. The process begins with the detachment of tumor cells from the adjacent endothelial cells and the basement membrane and is accompanied by the secretion of various cytokines and growth factors. Migration through the lymphatic vasculature is preferred over blood vessels because of reduced flow rates and pressure, easier access to the vessel, and wider vessel lumens.[2] Up to 80% of melanomas metastasize through the lymphatic system.[3] Additionally, tumor cells secrete lymph angiogenic growth factors like Vascular Endothelial Growth Factors that can stimulate lymph angiogenesis and further promote lymphatic migration.[3] These enlarged lymphatic vessels act as a freeway for the metastatic cells to gain access and spread to distal lymph nodes (LN) and organs.

Extensive research over the past two decades has helped us elucidate the driver mutations occurring in different oncogenes involved in the development of metastatic melanoma. The majority studied mutations occur primarily in the BRAF (a serine/threonine protein kinase) genes and have approved targeted therapies for patients in stage IV or unresectable melanoma.[4, 5] However, newer emerging genetic targets include Neuroblastoma –Rat Sarcoma (NRAS) [4-6] and nuclear receptors like Retinoid X Receptor-α (RXRα) genes. [7, 8] In pathological conditions, point mutations at the codon 61 of NRAS (NRASQ^{61K}) gene locks the activated form of NRAS-GTP thereby promoting continuous up regulation of downstream effector proteins and signaling pathways in the malignant melanoma phenotype.[9, 10] Activated NRAS^{Q61K} mutations play a significant role in the development of metastatic melanoma and are the primary driver mutations that are responsible for the spread of the disease in humans.[11, 12] These oncogenic drivers in the NRAS ^{Q61K} promote invasiveness of the malignant cells and have larger nodal involvement when compared to the BRAF mutations.[13] RXRα plays a major role in gene expression and signal transduction and in human melanomas the expression of RXRα is lost as the disease progresses.[14] Animal studies have indicated that the loss of RXRα in skin keratinocytes can lead to the increased melanocyte proliferation and the formation of malignant melanomas.[8, 14] Thus, while therapies targeting the BRAF mutations exist, no such therapeutic approaches are currently available for the NRAS or RXRα mutations. In the current study, we have utilized two melanoma models (1) $NRAS^{Q61K}$ mice with functional RXRα and activated NRAS in the melanocytes [11], and (2) bigenic $NRAS^{Q61K}$ | $RXR\alpha^{ep-/-}$ mice selectively lacking $RXR\alpha$ in epidermal keratinocytes in combination with the activated NRAS. Ablation of $RXR\alpha$ alongside with $NRAS^{Q61K}$ mutations resulted in increased number/size of spontaneous melanomas with reduced latency and increased invasion to draining lymph nodes in the $NRAS^{Q61K}$ | $RXR\alpha^{ep-/-}$ mice.[15]

Currently the FDA has 10 approved drugs for the treatment of metastatic melanoma based on inhibiting BRAF, mitogen-activated protein kinase, tyrosine kinase, or angiogenesis.[16, 17] The major drawback of the current therapy is the inability to deliver therapeutic concentrations to the lymphatic system while avoiding systemic toxicity. The majority of these inhibitors are administered intravenously (IV), resulting in high doses in the systemic circulation with an insufficient dose reaching the lymphatic vasculature. Secondarily, chemo resistance has been noted for the approved drugs when used individually.[18] Tumor cells are also known to induce resistance by up regulating alternate pathways when one of the pathways is blocked by specific inhibitors.[18] Thus, there is a need for a combination therapy that can overcome drug resistance by acting on multiple pathways involved in melanoma as well as a drug delivery system that can be delivered into the lymphatic system.

Molecules and/or drug delivery systems accumulate in the lymphatics based on molecular weight, size, surface charge, and site of administration.[19, 20] A direct correlation between lymphatic absorption and molecular weight indicates that molecules with

MW > 16,000 Da preferentially accumulate into the lymphatics,[21] while, the optimum particle size for lymphatic uptake is between 10-80 nm.[22] Anionic charged particles have higher uptake compared to cationic or neutral particles, possibly due to the slight negative charge of the interstitium at the site of injection.[23] The site of administration also plays a major role in delivering therapeutic payloads to the lymphatics where a higher accumulation of injected formulation in lymphatics is noted when injected subcutaneously (SC) as compared to the IV.[24] Any macromolecules or nanoscale drug delivery systems injected IV are limited to the vascular space and do not partition into the interstitium. Thus, their uptake into the lymphatics is limited.[22, 25] As most chemotherapeutics for the treatment of melanoma are small molecules without the necessary properties for lymphatic uptake, a drug delivery system is needed to achieve the necessary lymphatic accumulation.

Chemotherapeutics like docetaxel (DTX; PubChem CID: 148124), everolimus (EVR; PubChem CID: 6442177), and the experimental compound LY294002 (LY; PubChem CID: 3973) are small molecules with MW ranging from 300 to a 1000 Da with low intrinsic aqueous solubilities (Figure 2a). Each of these molecules acts on different pathways to inhibit tumor proliferation. DTX acts by stabilizing the microtubules, EVR and LY act on mammalian target of rapamycin, mTORC1 and mTORC2, respectively.[26-28] Together, EVR and LY, can completely inhibit the mTOR pathway while LY is also capable of inhibiting the Phosphoinositide 3-Kinase (PI3K) pathway.[27, 28] However, IV or SC administration of these molecules individually or together will lead to systemic absorption with little accumulation in the lymphatic system.

Nanoparticles (NP), prepared with amphiphilic block copolymers, are drug delivery systems that can be modified to target the lymphatic system.[29] These block copolymers are comprised of hydrophilic and hydrophobic domains with varying chain lengths and different end groups that can be used to modulate NP size and charge density.[30] Additionally, polyester-based polymers like polyethylene glycol-*block*-poly (ε-caprolactone) (PEG-PCL) are biodegradable and biocompatible.[30] The NP formulated using these polymers have demonstrated excellent stability, increase the drug circulation time, and are capable of solubilizing poorly water soluble drugs while simultaneously delivering multiple drugs.[30-32] Incorporation of DTX, EVR, and LY into a NP drug delivery system might overcome the chemo resistance issues while simultaneously targeting the lymphatics. Therefore, we hypothesize that DTX, EVR, and LY loaded PEG-PCL NP with specific size and surface charge density, administered SC, will have preferential uptake and accumulation in the lymphatic system and will exert synergistic anti-proliferative effects in clinically relevant melanoma models. Our objectives are to formulate and characterize three-drug loaded NP for the co-delivery of DTX, EVR and LY, and establish to their safety and efficacy in relevant melanoma mouse models.

2.3 MATERIALS AND METHODS

2.3.1 Materials

The polymers, methoxy poly(ethylene glycol)-*block*-poly(ε-caprolactone) (mPEG$_{5000}$-*b*-PCL$_{10000}$) [Mn=15000; PDI = 1.17] and carboxy poly(ethylene glycol)-*block*-poly(ε-caprolactone) COOH-PEG$_{5000}$-*b*-PCL$_{10300}$ [Mn=15300; PDI=1.39] were purchased from Advanced Polymer Materials Inc. (Montreal, CAN). DTX, EVR and LY were purchased from LC laboratories (Woburn, MA). Slide-A-Lyzer™ Dialysis Cassettes, 20K MWCO were obtained from Thermo Scientific Inc (Fairlawn, NJ). A375 human melanoma epithelial cells were obtained from American Type Culture Collection (Manassas, VA). Two metastatic melanoma mice models, *Tyr NRAS*^{Q61K} *RXR*$\alpha^{L2/L2}$ and *Tyr NRAS*^{Q61K} *RXR*$\alpha^{ep-/-}$, were generated according to previous work.[8, 11, 15, 33] CellTiter-Blue® Cell viability Assay was obtained from Promega Inc. (Madison, WI). Fontana-Masson stain kit was purchased from American Mastertech Scientific, Inc. (Lodi, CA). All reagents and supplies were purchased from VWR International, LLC (Radnor, PA) or Fischer Scientific Inc. (Fairlawn, NJ).

2.3.2 Methods

2.3.2.1 Preparation and characterization of three-drug loaded nanoparticles

DTX, EVR and LY three-drug loaded NP were prepared using a solvent evaporation method.[34] Briefly, 40 mg of the PEG-PCL polymers at various concentrations were dissolved in 2 mL of acetone. For neutral NP only mPEG-PCL (neutral NP) was used, while for partially charged NP, a mixture of mPEG: COOHPEG (60:40) (partially charged NP) with PCL was used. For the fully charged NP, 100% COOHPEG-PCL (fully charged NP) was used. Stock solutions of DTX, EVR and LY in acetone were prepared and required concentrations were added to the polymer solution to achieve a final concentration of 2 mg/mL of each drug. The drug polymer solution was transferred into a 10 mL round bottom flask and normal saline, 2 mL, was added followed by removal of the organic solvent using a rotary evaporator. The evaporation cycle was divided into three segments, with the first segment lasting 7 min at 420 mbar, the second for 7 min at 320 mbar and the final segment of 6 min at 200 mbar. The temperature of the water bath was maintained at 45 ^{o}C with a rotation of 100 rpm for the round bottom flask. To ensure complete removal of acetone the nanoparticle suspension placed in a hood for an additional hour to allow for evaporation of any residual acetone. Under these conditions minimal evaporation of normal saline occurs. The final volume was adjusted to 2 mL with saline. The NP were collected in a centrifuge tube and spun at 5,000 rpm for 3 minutes and filtered/sterilized using a 0.2 µm nylon filter prior to use.

NP were characterized for size, surface charge distribution, and drug loading. Particle size was characterized by Dynamic Light Scattering (DLS) using a Malvern Nano ZS (Malvern Instruments Inc, U.K.). All measurements were performed in triplicate and data is presented as the mean z-average diameter ± SD (nm) and polydispersity index (PDI ± SD). Statistical analysis (one way ANOVA) was performed using Graph Pad Prism software to determine statistical significance between the sizes of the empty, partially charged, and fully charged NP. The surface charge was measured using the same instrument and the data of three replicates is presented as mean zeta potential (ζ) ± SD (mV). The drug loading was determined by reverse phase high performance liquid chromatography (RP-HPLC) using a Shimadzu HPLC system consisting of LC-20 AT pump and SPD M20 a diode array detector. The analysis was performed using Zorbax C8 Column (4.6×75 mm, 3.5 µm) in isocratic mode with acetonitrile/water (62/38) containing 0.1% phosphoric acid and 1% methanol at a flow rate of 1 mL/min and an injection volume of 10 µL. Column temperature was maintained at 40 °C. The DTX, LY , and EVR peaks were monitored at 227 nm, 303nm and 279 nm respectively at retention times of 1.7, 2.3 and 5.7 min respectively. The peak purity for each of the compounds was determined at its respective wavelength using the Shimadzu LC Solutions software and based on the peak purity indices for all three compounds of 1.000 no impurities for the three peaks were detected (please refer to the supplemental information section for a more detailed discussion of the peak purity). The log P values for DTX, LY, and EVR are 3.54, 3.33, and 5.9 respectively (Advanced Chemistry Development ACD/Universal LogD Module, Percepta 14.0.0 (Build 1996)). The log D at pH 7.4 for DTX, LY, EVR are 3.54, 3.33. and 4.25 (Advanced Chemistry

Development ACD/Universal LogD Module, Percepta 14.0.0 (Build 1996)). Given the similarity in the log P and log D at pH 7.4 for DTX and LY the retention times for both molecules on the RP-HPLC are within 0.6 min of each other. All measurements were performed in triplicate and loading data are presented as mean drug loading (mg/mL) ± SD. As part of the RP-HPLC quantification residual acetone content was also assessed as a quality control measure and residual acetone content in the nanoparticles was determined to be 11.2 ± 3.6 mg per day, which is well below the United States Pharmacopeia 30 chapter <497> stated limit for a class 3 organic solvent of 50 mg per day.

2.3.2.2 In vitro drug release from the nanoparticles

The three-drug NP were prepared as described above. The release profile of DTX, EVR, and LY from neutral, partially charged, and fully charged NP was evaluated in 10 mM acetate buffer at pH 5.0 and 10 mM phosphate buffer pH 7.4 at 37 °C over 168 h (1 week) under sink conditions by dialysis.[35] Briefly, in three separate dialysis cassettes, for each type of NP, 2.0 mL of the sample was loaded. A MWCO of 20,000 Da was chosen to enable the unhindered diffusion of free drugs along with the unassociated polymer molecules out of the cassette. The cassettes were placed in 2.5 L of acetate or phosphate buffer and the temperature was maintained at 37 ^{o}C for the duration of the experiment. Sink conditions were ensured by changing the buffer every 3 h. Samples of 20 µL were withdrawn at 0, 0.5, 1, 2, 3, 6, 12, 24, 48, 72, 96, 120, 144, and 168 h and were replaced with an equal volume of fresh buffer. Samples were diluted 50 fold in the mobile phase and analyzed by RP-HPLC for drug content. The data is presented as mean % drug release ± SD. Data were curve fitted using a two phase exponential association equation in Graph Pad Prism 5 software. The time required to release 50% of the drug ($t_{1/2}$) in two phases, fast and slow, and the goodness of fit (r^2) values of three replicates are presented. Statistical Analysis using one-way ANOVA with Tukey’s post-test was performed on the release profiles for each drug across the different NP to assess for differences in rates of drug release. Statistical analysis was performed using GraphPad Prism 5 software.

2.3.2.3 In vitro cell viability assay and combination index (CI) analysis

A375 human malignant epithelial melanoma cells were seeded at a density of 5,000 cells/well in 96 well plates and allowed to attach for 12 h at 37 °C. Post-attachment, cells were treated with individual drugs (DTX, EVR, or LY) or two drugs (DTX: EVR, DTX:LY, or EVR:LY) or three drugs (DTX:EVR:LY) dissolved in DMSO at equivalent molar ratios. The concentration range for all three drugs was between 0.01–10,000 nM. The final concentration of DMSO in the wells was 1%. Empty NP and three drug loaded NP cell viability studies were also conducted under similar conditions. Cell viability was determined after 72 h by treatment with 20 μL of CellTiter-Blue® reagent followed by one hour of incubation at 37 °C and fluorescence intensity ($560_{EX}/590_{EM}$) was measured. All measurements were performed in quadruplicate. The mean drug concentration at 50% growth inhibition (IC_{50}) was determined using nonlinear fitting using a log(inhibitor) vs response – variable slope equation in GraphPad Prism (version 5.00 for Windows, GraphPad Software, San Diego California USA). For combinations in DMSO, the concentrations are reported for the most potent drug, usually DTX, except for the EVR: LY group, where they are reported in terms of EVR concentration for direct comparison. The combination effect of DTX: EVR, DTX: LY, EVR: LY, and DTX: EVR: LY in DMSO in A375 cells was evaluated using Compusyn software (Version 1.0, ComboSyn Inc.,U.S.) based on Chou and Talalay median-effect principle.[36] Combination Index (CI) values of <1, 1, or > 1 are indicative of synergy, additivity, or antagonism respectively. The software also generates CI values at various fractions of cells affected (Fa). The Fa value is proportional to the dose and therefore Fa vs CI plots can provide the interactive effects of the combinations over the various doses tested. The data, in quadruplicate, is presented as Fa vs CI plots to correlate the effect of the combinations at different treatment concentrations. CI analysis for NP was not conducted as the individual drugs in NP could not be stably produced to directly compare the individual NP and the combination NP groups for interactive effects.

2.3.2.4 In vivo assessment of safety and efficacy in Tyr NRAS^{Q61K} RXRα$^{L2/L2}$and Tyr NRAS^{Q61K} RXR $^{ep-/-}$ metastatic melanoma mouse models

Tyr NRAS^{Q61K} *RXRα*$^{L2/L2}$ (RXR+) and *Tyr NRAS*^{Q61K} *RXRα*$^{ep-/-}$ (RXR-) metastatic melanoma mouse models with the two major mutations (NRAS^{Q61k} and RXRα) found in human melanoma were used for the *in vivo* studies. The generation of *Tyr NRAS*^{Q61K} mice has been described in detail elsewhere.[8, 11, 12, 33] The mice were housed in ventilated cages with free access to food and water and were maintained at controlled temperature and humidity conditions for the duration of the experiment. Animals that were 8-12 weeks old were sorted into 2 major categories (RXR+ or RXR-). In each category, mice were subdivided into 7 groups with 4 animals per group. The groups included control untreated mice, control empty NP of each charge distribution, and treatment drug loaded NP of each charge distribution for a total of 28 animals per model (n = 56 for both models). Each group, except the untreated group, was treated with empty or three-drug loaded neutral, partially charged, or fully charged NP. Animals were injected SC (every week x 3 cycles) proximal to the inguinal (Figure 11) LN with 150 µL/side (total volume 300 µL) of the empty or three-drug loaded NP. Based on the drug loading in the nanoparticles, the amount of polymer used, and a dose volume of 300 µL per mouse we determined the doses for the three drugs in the treatment group. Thus, each animal received a dose of 20 mg/kg of each drug with a total dose of 60 mg/kg for all three drugs in the treatment groups and the dose of the polymer was approximately 240 mg/kg for all injected NP.

During the study (21 days), mice were monitored for signs of acute toxicity such as noticeable changes in general appearance, loss in median body weight ≥15%, or death. On day 21, 7 days post last injection, mice were euthanized and blood samples were collected, centrifuged at 3,000 x g for 7 min and the plasma samples were submitted for complete blood panel chemistry analysis. The analysis was performed at Oregon State University Veterinary Diagnostic Laboratory. The concentrations of blood urea nitrogen (BUN), creatinine, and alanine transaminase (ALT) values were assessed. BUN and creatinine are surrogate markers for kidney toxicity while ALT is a surrogate marker for liver toxicity.[37-39] The quantified values between the treatment and the control groups for both models were compared by one-way ANOVA with Tukey's multiple comparison post-test at a p-value of 0.05 using Graph Pad prism version 5.00 for Windows to assess organ toxicity. Data are presented as mean parameter value ± S.D of four replicates.

Immediately post-euthanasia and blood collection the inguinal and axillary LN (Figure 2.1) were collected and processed immediately to evaluate the efficacy in terms of reduction in melanocytes in response to the treatment. Briefly, LN were fixed in 4% paraformaldehyde and were embedded in paraffin blocks. For histological studies, 5 µm-thick paraffin sections from mouse LN were rehydrated and Fontana-Masson (FM) staining was performed according to manufacturer’s instructions. FM staining of skin-draining LNs is used as a general label for melanin pigment, which represent pigment-producing (melanocytic) cells, the nuclei are stained pink using a secondary Nuclear Red dye for contrast.[40] All microscopic studies were conducted using Leica DME light microscope and analyzed using Leica Application Suite software, version 3.3.1. Images were taken using 20X objective throughout the study. Post staining, quantifications of *melanin-pigmented area* were performed using Adobe Photoshop CS5 software. The pictures of LN were analyzed independently in a double-blind manner by two investigators, and significance was determined using a student’s two-tailed unpaired t-test as calculated by Graph Pad Prism software. Data are presented as mean # of melanocytes/ pigmented area ± SD in inguinal or axillary LN for four replicates.

All animal work was conducted in compliance with NIH guideline and Institutional Animal Care and Use Committee policy at Oregon State University for End-Stage Illness and Pre-emptive Euthanasia based on Humane Endpoints Guidelines.

2.4 RESULTS AND DISCUSSION

2.4.1 Preparation and characterization of three-drug loaded nanoparticles

Structures for the DTX, EVR, and LY along with a representation of the three-drug loaded NP are depicted in Figure 2.2. DTX, EVR, and LY neutral, partially charged, and fully charged NP are formulated by varying ratios of mPEG-PCL and COOH-PEG-PCL. Based on the RP-HPLC data the three-drug neutral, partially charged, and fully charged NP are able to solubilize approximately 2 mg of each drug and retain each of the drugs at the initial concentrations (within 6%) for 24 h (Figure 2.3). The intrinsic aqueous solubilities of DTX, EVR, and LY are 4 µg/Ml [26], 9.6 µg/mL[27], and 243 µg/mL[28] respectively. Thus, incorporation of these drugs into the NP increased the solubility of DTX, EVR, and LY by 455 fold, 201 fold and 8 fold respectively, thereby achieving therapeutically relevant dosing concentrations for *in vivo* assessment. Our results are consistent with published results, where the incorporation of hydrophobic drugs into amphiphilic diblock copolymers like PEG-PCL increases their aqueous solubility and stability.[41, 42]

The particle sizes and polydispersity index (PDI) for the three-drug neutral, partially charged, and fully charged NP are presented in Table 2.1. The neutral, partially charged, and fully charged NP show unimodal distribution as indicated with PDI values of less than 0.35. After 24 h under refrigeration and at room temperature, the size was re-assessed and no changes are seen in size or distribution (data not shown). No changes in the size over time are indicative of stability as no aggregation of the NP is occurring. Statistical analysis of the size distribution indicates that there is no significant difference between the particle sizes for neutral, partially charged, and fully charged NP. The mean zeta potential for neutral, partially charged, and fully charged NP are also presented in Table 2.1. As anticipated, the magnitude of the charge distribution correlates well with the increasing percentage of the negatively charged COOH-PEG-PCL content in the NP.

Size and surface charge are critical parameters in the selective uptake of NP into the lymphatic system.[20] PEG-PCL diblock copolymers can produce NP of uniform size (around 50 nm) that can selectively pass through the gaps in lymphatic endothelium (30-

100 nm).[43] Additionally, studies have shown that particles with a size above 20 nm accumulate into the lymphatics, however, when the particle size exceeds 100 nm the rate of particle drainage from the interstitum slows significantly.[20] Thus, optimal particle sizes for interstitial drainage and lymphatic accumulation are between 10 – 80 nm.[2] Accordingly, the drug loaded PEG-PCL NP in our study with an average size of 48 nm are expected to preferentially accumulate into the lymphatics. Surface charge is the other key parameter for lymphatic accumulation.[44] It has been widely reported in the literature that anionic NP have a higher uptake into lymphatic vessels when compared to their neutral and cationic counterparts.[2] Other studies have indicated that highly negative charged particles can trigger macrophage uptake.[45] Therefore, we anticipate that based on the surface charge distribution a differential accumulation of the NP in the lymph nodes *in vivo* will occur. Additionally, as all of the NP have similar sizes any differences in lymphatic uptake can be attributed to the difference in surface charge alone.

2.4.2 In vitro drug release from the nanoparticles

The release profiles of DTX, EVR and LY from the three-drug neutral, partially charged, and fully charged NP at pH 5.0 and 7.4 are shown in Figure 2.4 and the final % drug released values are presented in Table 2.2. The highest % release occurred with LY, followed by DTX, and then EVR. Overall, there is no significant difference in the rates of drug release for each drug from NP of different compositions at the same pH (Table 2.2 and Figure 2.4). The release profile of DTX, EVR and LY from the neutral, partially charged, and fully charged NP was almost identical at both pHs and exhibited no statistically significant difference (Table 2.2). The two phase exponential association $t_{1/2}$ and r^2 values for DTX, EVR, and LY release from the neutral, partially, and fully charged NP are presented in Table 2.3. However, the fast an slow half-lives were longer at pH 7.4 as compared to pH 5 as expected due to the higher rate of ester hydrolysis of the PEG-PCL at the lower pH. As seen in Figure 2.4, there is an initial phase involving burst/rapid release of the drugs from the NP followed by a more sustained release pattern at later stages. This biphasic release pattern exhibited by PEG-PCL NP has been well documented in the literature.[46, 47] The initial burst release is primarily driven by the desorption and the diffusion of surface adsorbed drug particles, while the secondary phase of drug release is driven by the erosion of the NP matrix and drug diffusion processes. The inner segment, PCL, is a biodegradable polyester that has a high crystallinity while the outer PEG shell increases the porosity in the PCL matrix and thereby allows the diffusion of drugs from the matrix into the buffer.[48] Thus drug release is governed by diffusion of the drug and erosion/degradation of the NP matrix.[49] Previous studies have demonstrated that solid state interactions between the drug and the hydrophobic block, and the mobility of the hydrophobic block all govern the drug release rate.[46] LY has the fastest drug release from the three-drug NP followed by DTX and then EVR. This may be due to the relative hydrophobicities of these molecules and their potential interaction with the PCL domain. The log D values at pH 7.4 for LY, DTX and EVR are 3.33, 3.54, and 4.25 respectively (Advanced Chemistry Development ACD/Universal LogD Module, Percepta 14.0.0 (Build 1996)).

2.4.3 In vitro cell viability assay and combination index (CI) analysis

The anti-proliferative effects (IC_{50} values) of DTX, EVR, and LY in DMSO individually and in two- and three-drug combinations evaluated in A375 human melanoma cells are presented in Figure 2.5(a). The two-drug combinations and the three-drug combinations in DMSO exhibited strong inhibition of A375 cell proliferation over a wide range of tested doses. Based on the data (Figure 2.5(a)) the two- and three- drug combinations are more potent as compared to the individual drug treatments, with the three-drug combination demonstrating the highest potency at 0.57 nM concentration. The two- and three- drug combinations were also evaluated for interactive effects (synergistic, additive, or antagonistic) using Compusyn software and the data are presented in Figure 2.5(b). The two-drug combination EVR:LY is synergistic at lower concentrations but becomes additive at higher concentrations. The DTX:EVR and DTX:LY combinations are synergistic at all concentrations (Figure 2.5(b)). The three-drug combination is also synergistic at all the fractions affected indicating that the multiple mechanisms of action enhance the potency of the combination beyond what is expected with individual drug treatments alone. The combination neutral, partially charged, and fully charged NP were also evaluated for their respective IC_{50} values and data is presented in Figure 2.5(c). Not surprisingly the NP have a higher IC_{50} values as compared to the drugs/combinations in DMSO. This is due to the fact that the drug must not undergo diffusion from the NP and release is also dependent on the degradation of the NP. Additionally, the cell culture conditions do not mimic the sink conditions one can expect *in vivo* further slowing down the rate of drug release from the NP. Our findings are consistent with other published studies documenting the same phenomena.[50, 51] The empty NP did not affect cell viability (data not shown). CI analysis for NP was not feasible as the individual drugs in NP could not be stably produced to directly compare the individual NP and the combination NP groups for interactive effects.

The two-drug combinations, DTX:EVR and DTX:LY, illustrate the need to target multiple pathways, such as microtubule stabilization and mTOR inhibition. Interestingly, with EVR:LY, which specifically targets mTOR1 and mTOR2, at higher concentrations A357 cells seem to be able to overcome the synergy of this one pathway and maybe up/down regulating others and becoming less susceptible to drug(s) effects. Not surprisingly, the three-drug combination achieves sustained synergistic effects at the highest potency by blocking multiple pathways involved in cancer progression. Cancer cells up regulate alternative mechanisms to induce drug resistance when one particular pathway is blocked.[52] The mTOR pathway is involved in cell growth, proliferation, and survival, and in addition it affects downstream effector proteins which are essential for the protein translation processes.[52] It has been reported previously that the mTOR pathway is highly up regulated in malignant melanoma due to the NRAS mutation [53] and inhibiting the mTOR pathway can have beneficial effects in the treatment regimen.[54] EVR acts on the mTOR1 pathway and it is known that the cancer cells immediately up regulate the mTOR2 pathway to induce drug resistance when the mTOR1 pathway is blocked.[55] LY targets the mTOR2 pathway and also blocks the PI3K/AKT pathway. Thus, when LY is used in combination with EVR, the mTOR cascade is completely blocked.[54] Ablation of RXRα alongside with $NRAS^{Q61K}$ mutations results in an increased number/size of spontaneous melanomas with reduced latency and increased invasion to draining lymph nodes in the

$NRAS^{Q61K}$ | $RXR\alpha^{ep-/-}$ mice).[15] Thus, far there are no drugs targeting this mutation specifically. Therefore, the three drug combination was evaluated in both the RXR+ and RXR- mice to determine the efficacy of the regimen in both. DTX acts by a completely different mechanism where it stabilizes the microtubules and thereby induces apoptosis as a general chemotherapeutic strategy.[56] Thus, the combination of these three drugs can synergistically inhibit proliferation through multiple mechanisms of action as evidenced by the potency and CI for the three-drug combination as compared to individual drugs or the two-drug combinations.

2.4.4 In vivo assessment of safety and efficacy in Tyr $NRAS^{Q61K}$ $RXR\alpha^{L2/L2}$ and Tyr $NRAS^{Q61K}$ $RXR\alpha^{ep-/-}$ metastatic melanoma mouse models

The safety profile of the neutral, partially charged, and fully charged NP has been evaluated in two metastatic melanoma mouse models containing activating $NRAS^{Q61K}$ driver mutation and with or without RXRα protein (RXR+ or RXR-), which develop melanoma with different latency and with LN metastasis as described elsewhere.[15] None of the mice in either model died or exhibited abnormal behavioral changes during the duration of the study. Changes in the weight, during the course of the study, for the neutral, partially charged, and fully charged NP, with or without the three drugs are presented in Figure 2.6. Based on the data, none of the groups in either model demonstrated weight loss ≥ 15% indicating that neither the empty NP nor the three-drug NPs produce acute toxicity at 20 mg/kg dose of each drug (total 60 mg/kg dose) and 240 mg/kg of the NP polymer.

The blood biochemical values for BUN, Creatinine, and ALT, for all the groups in each model are presented in Figures 2.7 – 2.9. BUN, Creatinine, and ALT values in RXR+ and RXR- treated with empty neutral or three-drug neutral NP indicates that there are no statistically significant differences between the treatment groups and the untreated and vehicle controls (Figure 2.7). Similar results were seen with the partially charged (Figure 2.8) and fully charged (Figure 2.9) NP groups. BUN, and creatinine levels are indicators of kidney function.[38] In cases of renal toxicity, levels of BUN and/or creatinine are elevated.[38] ALT is present in all tissues throughout the entire body, but is particularly concentrated in liver, bile duct, kidney, and bone.[39] Elevated ALT levels are usually indicative of liver toxicity.[39] Based on the behavioral observations, weight data (Figure 2.5), and the biochemical estimations (Figure 2.7 – 2.9) no acute toxicity is observed with either the empty or three-drug loaded NP.

The effectiveness of the treatment in the two different models of metastatic melanoma mouse models is established using Fontana Masson (FM) staining of the LN followed by quantification of pigment areas covered with invading melanocytes in the draining LN using Adobe Photoshop CS5 software. The melanocyte covered pigmented area (black stain) between the empty NP and the three-drug NP for the same charge distribution were compared to quantify the efficacy, in terms of decrease in the number of invasive, malignant melanocytes in the LNs.

A representative microscopic data set from the inguinal and axillary LN is presented in Figure 2.9 for RXR+ and RXR- mice treated with neutral, partially charged, and fully charged empty or three-drug NP. The reduction in the transformed melanocytes covered pigmented area is dependent on the uptake and trafficking of the differently charged NP in the lymphatic system. As seen in figure 2.10(a), with three-drug neutral NP as compared to empty neutral NP a reduction in melanocytes area in the inguinal LN (proximal to the injection sites) is seen in both models (RXR+ and RXR-), however, no change in pigmented melanocytes area was noted in the axillary LN (distal from the injection sites). Thus, indicating that the efficacy of the drug loaded neutral particles is limited to the inguinal LN in both models. Analysis of melanocyte covered pigmented area indicates a statistically significant difference ($p = 0.0003$) at the inguinal LN of both the RXR+ and RXR- groups (Figure 2.11 (a & b)), but no difference is observed at the axillary LN. One possible explanation is that the NP remained at the site of injection after dosing and showed efficacy only at the proximal inguinal LN. One of the ways by which particles traffic into the lymphatic system is through charge repulsion between the NP and the interstitium at the site of injection.[44] For the neutral NP the magnitude of the surface charge may not be large enough to induce electrostatic repulsions to allow for distal trafficking through the lymphatics. Additionally, studies by others have shown that neutral NP tend to aggregate at the site of injection which may also confirm our findings that the particles do not track distally into the lymphatics but show efficacy regionally.[57]

In comparing the three-drug partially charged NP to empty partially charged NP (Figure 2.10(b)), a decrease in melanocytes at both the inguinal and the axillary LN in both models is noted. These results indicate that the three-drug partially charged NP are efficacious at both the proximal (inguinal) and distal (axillary) LN as referenced from the site of injection for both the models. Analysis of melanocyte covered pigmented area indicates a statistically significant difference at both the inguinal ($p < 0.0001$) and the axillary ($p < 0.0001$) LN in both the mouse models upon treatment with the three-drug partially charged NP (Figure 2.11(c & d)). The lymphatic vessels and the interstitium have a slight negative charge because of the presence of glycosaminoglycans and the electrostatic repulsions between these and the partially charged NP (surface charge of -19 mV) may be responsible for the deeper movement of the particles into the lymphatic system.[44] The ability of these NP to track into the distal LN may provide an excellent opportunity to target advanced stages of metastatic melanoma and improve patient outcomes.

Comparing the staining in empty fully charged and three-drug fully charged NP (Figure 2.10(c)), no difference at either the inguinal or the axillary LN is observed in both models. Thus, establishing that the fully charged NP did not have appreciable accumulation in either of the two LN studied. Analysis of melanocyte covered pigmented area indicates no difference between empty and three-drug fully charged NP at both the inguinal and axillary LN in both models (Figure 2.11(e & f)). The data indicates that highly negatively charged particles did not tract into either the regional or distal LN (Figure 2.10c, 2.11e & f). Previously published literature has suggested that highly negatively charged particles are rapidly taken up and sequestered by macrophages.[45] The high anionic charge on these NP also tends to attract serum proteins resulting in the formation of a protein corona that promotes the release of signals for macrophage uptake.[45] For example, anionic polystyrene nanoparticles have 4 times higher uptake by macrophages in serum as compared to uptake from buffer solutions indicting the role of serum proteins in the uptake mechanism and kinetics.[45] Research has also indicated that highly anionic nanoparticles resemble bacteria in their surface charge and therefore interact preferentially with phagocytic cells.[58] Additional studies in the future to characterize the immune responses triggered by the different NPs may shed light about the involvement of immune cells, including the macrophages, in the lymphatic tracking of these NP.

We have used two different animal models in this study containing mutations in NRAS and/or RXRα to elucidate the effectiveness of our developed drug delivery system and to characterize the efficacy and toxicity of our formulated NP.[4-8, 11] The *Tyr* $NRAS^{Q61K}RXR\alpha^{L2/L2}$ (RXR+) mice represent a model with increased latency to develop invasive melanoma while *Tyr* $NRAS^{Q61K}RXR\alpha^{ep-/-}$ (RXR-) bigenic mice, selectively lacking RXRα in the epidermis alongside with the activating NRAS mutation in the melanocytes, represent a metastatic melanoma model where melanoma cells readily migrate and invade the lymphatics.[9, 33]Analysis of melanocyte covered pigmented area comparing RXR+ and RXR- for the three-drug NP with same charge distribution indicates that no statistically significant difference is demonstrated (Figures 2.10 & 2.11). Thereby indicating that the NP retained efficacy across the two different melanoma models. Future studies using fluorescent dye loaded NP will be performed to obtain further insight about the biodistribution of these NP while simultaneously tracking their lymphatic movement and accumulation.

2.5 CONCLUSION

In summary, we have developed and characterized a three-drug (DTX, EVR and LY) NP that acts synergistically *in vivo* in two different melanoma mouse models. Our results indicate that the effect of the three-drug neutral NP is proximal to the site of injection, while the three-drug partially charged NP track further into the lymphatic system reaching more distal LNs. In contrast, the three-drug fully charged NP have minimal effects on the proximal or distal LN. The three-drug combination neutral and partially charged NP are highly effective in treating melanoma in both models and provide the basis for a novel therapeutic option treating metastatic melanoma that is targeted to the site of action, i.e. the lymphatic system.

2.6 ACKNOWLEDGEMENTS

This study was supported by Oregon State University-Startup fund.

2.7 REFERENCES

[1] J.A. Lo, D.E. Fisher, The melanoma revolution: from UV carcinogenesis to a new era in therapeutics. Science 346(6212) (2014) 945-949. 10.1126/science.1253735

[2] G.M. Ryan, L.M. Kaminskas, C.J. Porter, Nano-chemotherapeutics: maximising lymphatic drug exposure to improve the treatment of lymph-metastatic cancers. J Control Release 193 (2014) 241-256. 10.1016/j.jconrel.2014.04.051

[3] A. Alitalo, M. Detmar, Interaction of tumor cells and lymphatic vessels in cancer progression. Oncogene 31(42) (2012) 4499-4508. 10.1038/onc.2011.602

[4] I.C. Glitza, M.A. Davies, Genotyping of cutaneous melanoma. Chin Clin Oncol 3(3) (2014) 27. 10.3978/j.issn.2304-3865.2014.03.01

[5] M. Pracht, A. Mogha, A. Lespagnol, A. Fautrel, N. Mouchet, F. Le Gall, V. Paumier, C. Lefeuvre-Plesse, N. Rioux-Leclerc, J. Mosser, E. Oger, H. Adamski, M.D. Galibert, T. Lesimple, Prognostic and predictive values of oncogenic BRAF, NRAS, c-KIT and MITF in cutaneous and mucous melanoma. J Eur Acad Dermatol Venereol 29(8) (2015) 1530-1538. 10.1111/jdv.12910

[6] A.K. Eisfeld, S. Schwind, K.W. Hoag, C.J. Walker, S. Liyanarachchi, R. Patel, X. Huang, J. Markowitz, W. Duan, G.A. Otterson, W.E. Carson, 3rd, G. Marcucci, C.D. Bloomfield, A. de la Chapelle, NRAS isoforms differentially affect downstream pathways, cell growth, and cell transformation. Proc Natl Acad Sci U S A 111(11) (2014) 4179-4184. 10.1073/pnas.1401727111

[7] Z. Wang, D.J. Coleman, G. Bajaj, X. Liang, G. Ganguli-Indra, A.K. Indra, RXRalpha ablation in epidermal keratinocytes enhances UVR-induced DNA damage, apoptosis, and proliferation of keratinocytes and melanocytes. J Invest Dermatol 131(1) (2011) 177-187. 10.1038/jid.2010.290

[8] D.J. Coleman, G. Garcia, S. Hyter, H.S. Jang, S. Chagani, X. Liang, L. Larue, G. Ganguli-Indra, A.K. Indra, Retinoid-X-receptors (alpha/beta) in melanocytes modulate innate immune responses and differentially regulate cell survival following UV irradiation. PLoS Genet 10(5) (2014) e1004321. 10.1371/journal.pgen.1004321

[9] M. Mandala, B. Merelli, D. Massi, Nras in melanoma: targeting the undruggable target. Crit Rev Oncol Hematol 92(2) (2014) 107-122. 10.1016/j.critrevonc.2014.05.005

[10] K. Omholt, S. Karsberg, A. Platz, L. Kanter, U. Ringborg, J. Hansson, Screening of N-ras codon 61 mutations in paired primary and metastatic cutaneous melanomas:

mutations occur early and persist throughout tumor progression. Clin Cancer Res 8(11) (2002) 3468-3474.

[11] J. Ackermann, M. Frutschi, K. Kaloulis, T. McKee, A. Trumpp, F. Beermann, Metastasizing melanoma formation caused by expression of activated N-RasQ61K on an INK4a-deficient background. Cancer Res 65(10) (2005) 4005-4011. 10.1158/0008-5472.CAN-04-2970

[12] L. Mansi, E. Viel, E. Curtit, J. Medioni, C. Le Tourneau, [Targeting the RAS signalling pathway in cancer]. Bull Cancer 98(9) (2011) 1019-1028. 10.1684/bdc.2011.1380

[13] V.J. Mar, W. Liu, B. Devitt, S.Q. Wong, A. Dobrovic, G.A. McArthur, R. Wolfe, J.W. Kelly, The role of BRAF mutations in primary melanoma growth rate and survival. Br J Dermatol 173(1) (2015) 76-82. 10.1111/bjd.13756

[14] S. Hyter, G. Bajaj, X. Liang, M. Barbacid, G. Ganguli-Indra, A.K. Indra, Loss of nuclear receptor RXRalpha in epidermal keratinocytes promotes the formation of Cdk4-activated invasive melanomas. Pigment Cell Melanoma Res 23(5) (2010) 635-648. 10.1111/j.1755-148X.2010.00732.x

[15] D.J. Coleman, S. Chagani, S. Hyter, A.M. Sherman, C.V. Lohr, X. Liang, G. Ganguli-Indra, A.K. Indra, Loss of keratinocytic RXRalpha combined with activated CDK4 or oncogenic NRAS generates UVB-induced melanomas via loss of p53 and PTEN in the tumor microenvironment. Mol Cancer Res 13(1) (2015) 186-196. 10.1158/1541-7786.MCR-14-0164

[16] A. Marzuka, L. Huang, N. Theodosakis, M. Bosenberg, Melanoma Treatments: Advances and Mechanisms. J Cell Physiol 230(11) (2015) 2626-2633. 10.1002/jcp.25019

[17] C. Karimkhani, R. Gonzalez, R.P. Dellavalle, A review of novel therapies for melanoma. Am J Clin Dermatol 15(4) (2014) 323-337. 10.1007/s40257-014-0083-7

[18] M.S. Soengas, S.W. Lowe, Apoptosis and melanoma chemoresistance. Oncogene 22(20) (2003) 3138-3151. 10.1038/sj.onc.1206454

[19] D.A. Rao, M.L. Forrest, A.W. Alani, G.S. Kwon, J.R. Robinson, Biodegradable PLGA based nanoparticles for sustained regional lymphatic drug delivery. J Pharm Sci 99(4) (2010) 2018-2031. 10.1002/jps.21970

[20] A. Ali Khan, J. Mudassir, N. Mohtar, Y. Darwis, Advanced drug delivery to the lymphatic system: lipid-based nanoformulations. Int J Nanomedicine 8 (2013) 2733-2744. 10.2147/IJN.S41521

[21] A. Supersaxo, W.R. Hein, H. Steffen, Effect of molecular weight on the lymphatic absorption of water-soluble compounds following subcutaneous administration. Pharm Res 7(2) (1990) 167-169.

[22] Y. Xie, T.R. Bagby, M.S. Cohen, M.L. Forrest, Drug delivery to the lymphatic system: importance in future cancer diagnosis and therapies. Expert Opin Drug Deliv 6(8) (2009) 785-792. 10.1517/17425240903085128

[23] D.N. McLennan, C.J. Porter, S.A. Charman, Subcutaneous drug delivery and the role of the lymphatics. Drug Discov Today Technol 2(1) (2005) 89-96. 10.1016/j.ddtec.2005.05.006

[24] J. Kota, K.K. Machavaram, D.N. McLennan, G.A. Edwards, C.J. Porter, S.A. Charman, Lymphatic absorption of subcutaneously administered proteins: influence of different injection sites on the absorption of darbepoetin alfa using a sheep model. Drug Metab Dispos 35(12) (2007) 2211-2217. 10.1124/dmd.107.015669

[25] K.D. Wilson, S.G. Raney, L. Sekirov, G. Chikh, S.D. deJong, P.R. Cullis, Y.K. Tam, Effects of intravenous and subcutaneous administration on the pharmacokinetics, biodistribution, cellular uptake and immunostimulatory activity of CpG ODN encapsulated in liposomal nanoparticles. Int Immunopharmacol 7(8) (2007) 1064-1075. 10.1016/j.intimp.2007.04.002

[26] S. Mazzaferro, K. Bouchemal, J.F. Gallard, B.I. Iorga, M. Cheron, C. Gueutin, C. Steinmesse, G. Ponchel, Bivalent sequential binding of docetaxel to methyl-beta-cyclodextrin. Int J Pharm 416(1) (2011) 171-180. 10.1016/j.ijpharm.2011.06.034

[27] Y. Iwase, Y. Maitani, Preparation and in vivo evaluation of liposomal everolimus for lung carcinoma and thyroid carcinoma. Biol Pharm Bull 35(6) (2012) 975-979.

[28] W. Saiyin, D. Wang, L. Li, L. Zhu, B. Liu, L. Sheng, Y. Li, B. Zhu, L. Mao, G. Li, X. Zhu, Sequential release of autophagy inhibitor and chemotherapeutic drug with polymeric delivery system for oral squamous cell carcinoma therapy. Mol Pharm 11(5) (2014) 1662-1675. 10.1021/mp5000423

[29] J.M. Chan, P.M. Valencia, L. Zhang, R. Langer, O.C. Farokhzad, Polymeric nanoparticles for drug delivery. Methods Mol Biol 624 (2010) 163-175. 10.1007/978-1-60761-609-2_11

[30] K. Letchford, H. Burt, A review of the formation and classification of amphiphilic block copolymer nanoparticulate structures: micelles, nanospheres, nanocapsules and polymersomes. Eur J Pharm Biopharm 65(3) (2007) 259-269. 10.1016/j.ejpb.2006.11.009

[31] N. Dubey, R. Varshney, J. Shukla, A. Ganeshpurkar, P.P. Hazari, G.P. Bandopadhaya, A.K. Mishra, P. Trivedi, Synthesis and evaluation of biodegradable PCL/PEG nanoparticles for neuroendocrine tumor targeted delivery of somatostatin analog. Drug Deliv 19(3) (2012) 132-142. 10.3109/10717544.2012.657718

[32] X. He, L. Li, H. Su, D. Zhou, H. Song, L. Wang, X. Jiang, Poly(ethylene glycol)-block-poly(epsilon-caprolactone)-and phospholipid-based stealth nanoparticles with

enhanced therapeutic efficacy on murine breast cancer by improved intracellular drug delivery. Int J Nanomedicine 10 (2015) 1791-1804. 10.2147/IJN.S75186

[33] M. Li, H. Chiba, X. Warot, N. Messaddeq, C. Gerard, P. Chambon, D. Metzger, RXR-alpha ablation in skin keratinocytes results in alopecia and epidermal alterations. Development 128(5) (2001) 675-688.

[34] H.R. Marsden, L. Gabrielli, A. Kros, Rapid preparation of polymersomes by a water addition/solvent evaporation method. Polymer Chemistry 1(9) (2010) 1512-1518. 10.1039/c0py00172d

[35] J. Shen, D.J. Burgess, Dissolution Testing Strategies for Nanoparticulate Drug Delivery Systems: Recent Developments and Challenges. Drug Deliv Transl Res 3(5) (2013) 409-415. 10.1007/s13346-013-0129-z

[36] T.C. Chou, P. Talalay, Quantitative analysis of dose-effect relationships: the combined effects of multiple drugs or enzyme inhibitors. Adv Enzyme Regul 22 (1984) 27-55.

[37] S.M. DeAtley, M.Y. Aksenov, M.V. Aksenova, B. Jordan, J.M. Carney, D.A. Butterfield, Adriamycin-induced changes of creatine kinase activity in vivo and in cardiomyocyte culture. Toxicology 134(1) (1999) 51-62.

[38] A. Jamshidzadeh, R. Heidari, S. Mohammadi-Samani, N. Azarpira, A. Najbi, P. Jahani, N. Abdoli, A comparison between the nephrotoxic profile of gentamicin and gentamicin nanoparticles in mice. J Biochem Mol Toxicol 29(2) (2015) 57-62. 10.1002/jbt.21667

[39] S.P. Singh, M. Kumari, S.I. Kumari, M.F. Rahman, M. Mahboob, P. Grover, Toxicity assessment of manganese oxide micro and nanoparticles in Wistar rats after 28 days of repeated oral exposure. J Appl Toxicol 33(10) (2013) 1165-1179. 10.1002/jat.2887

[40] V.S. Carriel, J. Aneiros-Fernandez, S. Arias-Santiago, I.J. Garzon, M. Alaminos, A. Campos, A novel histochemical method for a simultaneous staining of melanin and collagen fibers. J Histochem Cytochem 59(3) (2011) 270-277. 10.1369/0022155410398001

[41] X. Wei, C. Gong, M. Gou, S. Fu, Q. Guo, S. Shi, F. Luo, G. Guo, L. Qiu, Z. Qian, Biodegradable poly(epsilon-caprolactone)-poly(ethylene glycol) copolymers as drug delivery system. Int J Pharm 381(1) (2009) 1-18. 10.1016/j.ijpharm.2009.07.033

[42] S.R. Mudshinge, A.B. Deore, S. Patil, C.M. Bhalgat, Nanoparticles: Emerging carriers for drug delivery. Saudi Pharm J 19(3) (2011) 129-141. 10.1016/j.jsps.2011.04.001

[43] G. Luo, X. Yu, C. Jin, F. Yang, D. Fu, J. Long, J. Xu, C. Zhan, W. Lu, LyP-1-conjugated nanoparticles for targeting drug delivery to lymphatic metastatic tumors. Int J Pharm 385(1-2) (2010) 150-156. 10.1016/j.ijpharm.2009.10.014

[44] S.T. Proulx, P. Luciani, L.C. Dieterich, S. Karaman, J.C. Leroux, M. Detmar, Expansion of the lymphatic vasculature in cancer and inflammation: new opportunities for in vivo imaging and drug delivery. J Control Release 172(2) (2013) 550-557. 10.1016/j.jconrel.2013.04.027

[45] O. Lunov, T. Syrovets, C. Loos, J. Beil, M. Delacher, K. Tron, G.U. Nienhaus, A. Musyanovych, V. Mailander, K. Landfester, T. Simmet, Differential uptake of functionalized polystyrene nanoparticles by human macrophages and a monocytic cell line. ACS Nano 5(3) (2011) 1657-1669. 10.1021/nn2000756

[46] W. Peng, X.Y. Jiang, Y. Zhu, E. Omari-Siaw, W.W. Deng, J.N. Yu, X.M. Xu, W.M. Zhang, Oral delivery of capsaicin using MPEG-PCL nanoparticles. Acta Pharmacol Sin 36(1) (2015) 139-148. 10.1038/aps.2014.113

[47] R. Li, X. Li, L. Xie, D. Ding, Y. Hu, X. Qian, L. Yu, Y. Ding, X. Jiang, B. Liu, Preparation and evaluation of PEG-PCL nanoparticles for local tetradrine delivery. Int J Pharm 379(1) (2009) 158-166. 10.1016/j.ijpharm.2009.06.007

[48] F. Ahmed, D.E. Discher, Self-porating polymersomes of PEG-PLA and PEG-PCL: hydrolysis-triggered controlled release vesicles. J Control Release 96(1) (2004) 37-53. 10.1016/j.jconrel.2003.12.021

[49] P.R. Lockman, R.J. Mumper, M.A. Khan, D.D. Allen, Nanoparticle technology for drug delivery across the blood-brain barrier. Drug Dev Ind Pharm 28(1) (2002) 1-13. 10.1081/DDC-120001481

[50] X. Cheng, L. Kuhn, Chemotherapy drug delivery from calcium phosphate nanoparticles. Int J Nanomedicine 2(4) (2007) 667-674.

[51] X. Xu, C.R. Sabanayagam, D.A. Harrington, M.C. Farach-Carson, X. Jia, A hydrogel-based tumor model for the evaluation of nanoparticle-based cancer therapeutics. Biomaterials 35(10) (2014) 3319-3330. 10.1016/j.biomaterials.2013.12.080

[52] R. Marone, D. Erhart, A.C. Mertz, T. Bohnacker, C. Schnell, V. Cmiljanovic, F. Stauffer, C. Garcia-Echeverria, B. Giese, S.M. Maira, M.P. Wymann, Targeting melanoma with dual phosphoinositide 3-kinase/mammalian target of rapamycin inhibitors. Mol Cancer Res 7(4) (2009) 601-613. 10.1158/1541-7786.MCR-08-0366

[53] C. Posch, H. Moslehi, L. Feeney, G.A. Green, A. Ebaee, V. Feichtenschlager, K. Chong, L. Peng, M.T. Dimon, T. Phillips, A.I. Daud, T.H. McCalmont, P.E. LeBoit, S. Ortiz-Urda, Combined targeting of MEK and PI3K/mTOR effector pathways is necessary to effectively inhibit NRAS mutant melanoma in vitro and in vivo. Proc Natl Acad Sci U S A 110(10) (2013) 4015-4020. 10.1073/pnas.1216013110

[54] M. Karbowniczek, C.S. Spittle, T. Morrison, H. Wu, E.P. Henske, mTOR is activated in the majority of malignant melanomas. J Invest Dermatol 128(4) (2008) 980-987. 10.1038/sj.jid.5701074

[55] W.J. Oh, E. Jacinto, mTOR complex 2 signaling and functions. Cell Cycle 10(14) (2011) 2305-2316.

[56] M. Joerger, Metabolism of the taxanes including nab-paclitaxel. Expert Opin Drug Metab Toxicol 11(5) (2015) 691-702. 10.1517/17425255.2015.983074

[57] M.P. Osborne, V.J. Richardson, K. Jeyasingh, B.E. Ryman, Radionuclide-labelled liposomes--a new lymph node imaging agent. Int J Nucl Med Biol 6(2) (1979) 75-83.

[58] E. Frohlich, The role of surface charge in cellular uptake and cytotoxicity of medical nanoparticles. Int J Nanomedicine 7 (2012) 5577-5591. 10.2147/IJN.S36111

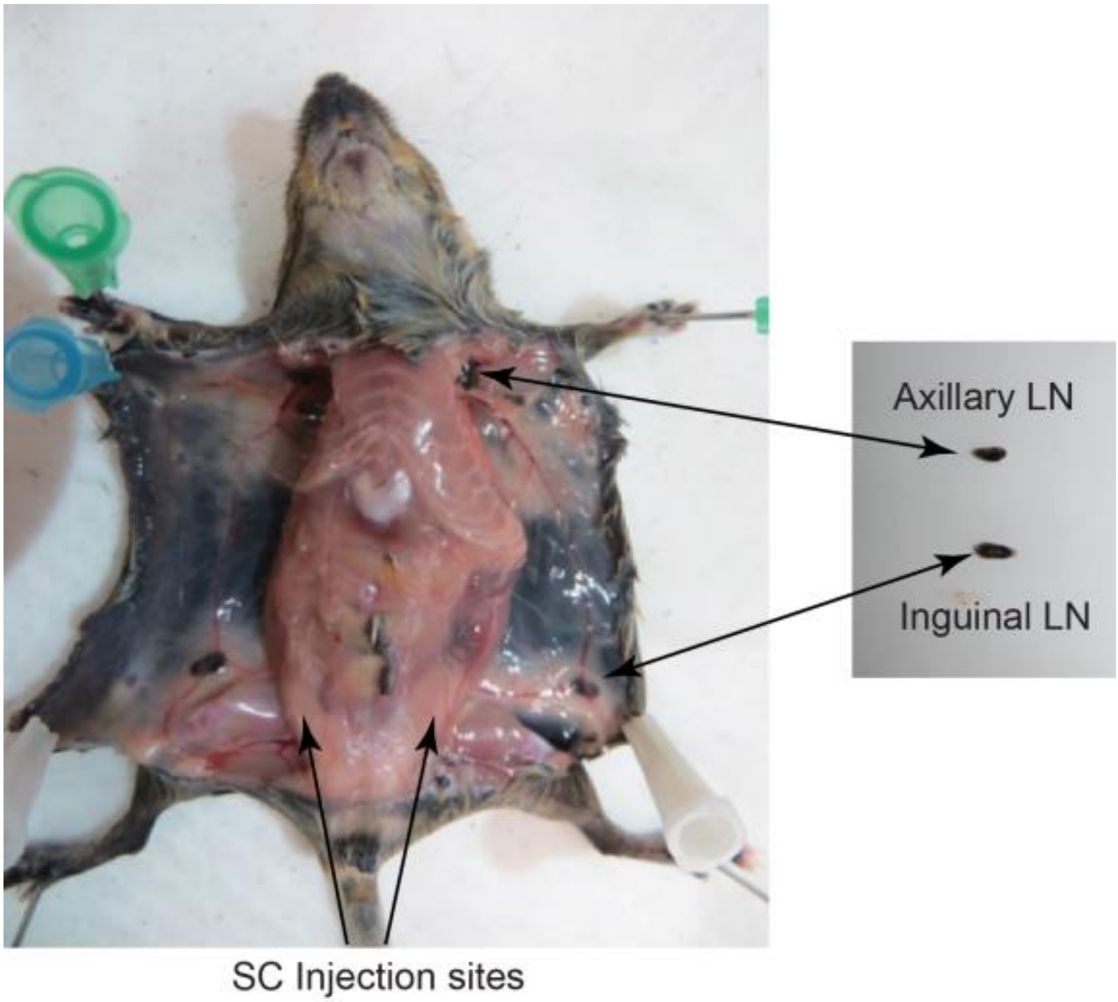

Figure 2.1: Phenotypic appearance of the mouse.

Phenotypic appearance of Tyr NRAS^{Q61K} RXRα$^{L2/L2}$ (RXR+) or Tyr NRAS^{Q61K} RXRα$^{ep-/-}$ (RXR-) with injection site and lymph nodes of interest (Inguinal and Axillary)

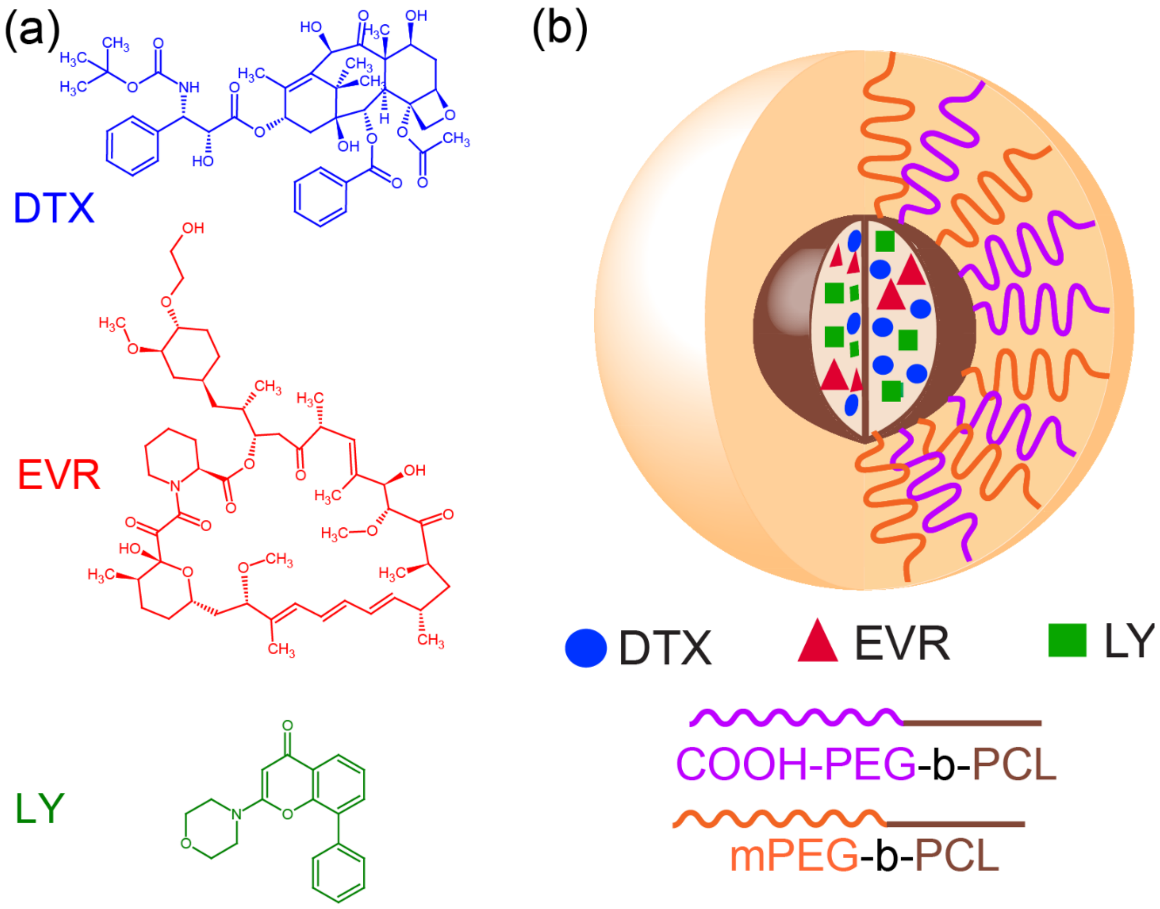

Figure 2.2: Structures of drugs and schematic representation of the nanoparticle.

(a) Structures of DTX, EVR, and LY **(b)** Schematic representation of the three-drug (DTX, EVR and LY) loaded NP

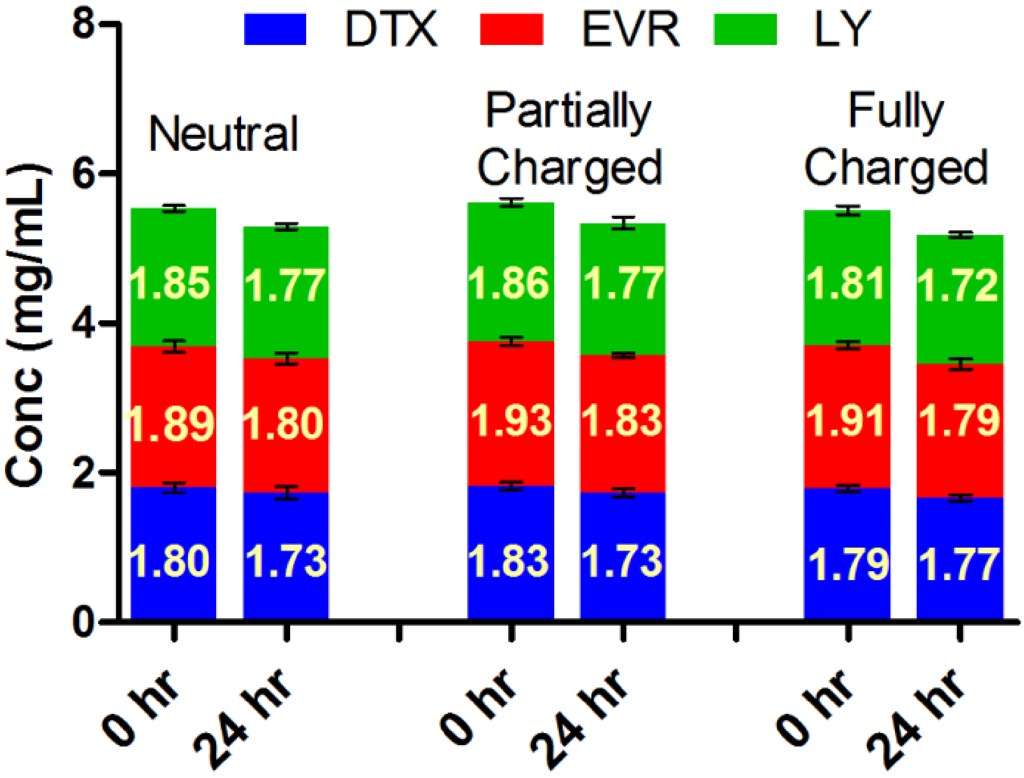

Figure 2.3: Stability data of nanoparticles.

Initial loading and drug retention at 24 h for DTX, EVR, and LY in three-drug neutral, partially charged, and fully charged NP (Mean ± S.D, n = 3). The numbers indicate average loading concentrations for each individual drug in the NP.

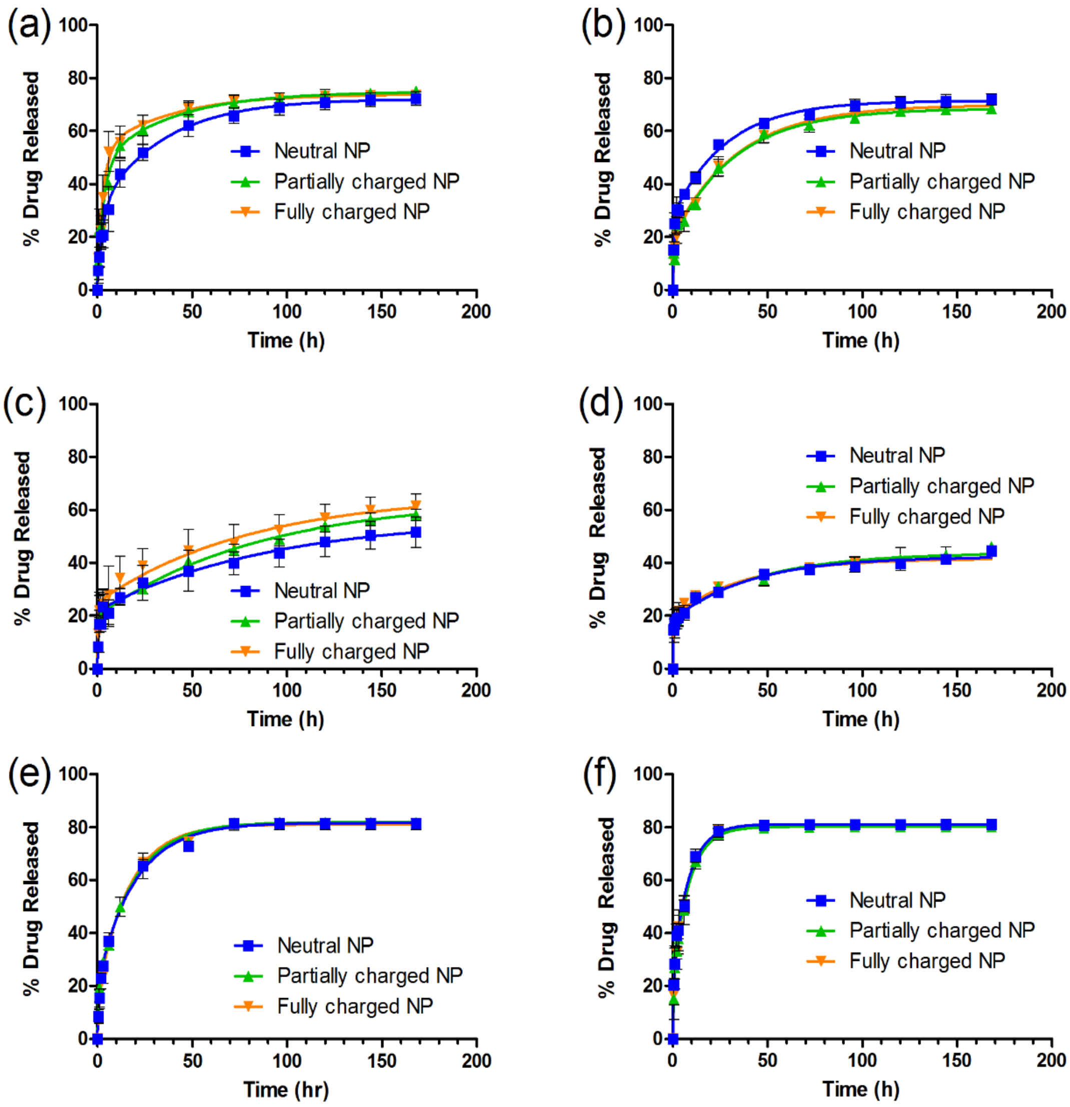

Figure 2.4: In vitro drug release profiles at pH 5.0 and 7.4.

In vitro drug release profiles of **(a)** DTX at pH 7.4, **(b)** DTX at pH 5.0 , **(c)** EVR at pH 7.4 **(d)** EVR at pH 5.0 , **(e)** LY at pH 7.4 **(f)** LY at pH 5.0 from neutral, partially charged, and fully charged NP under sink conditions over 48 h. (Mean % drug release ± S.D, n = 3)

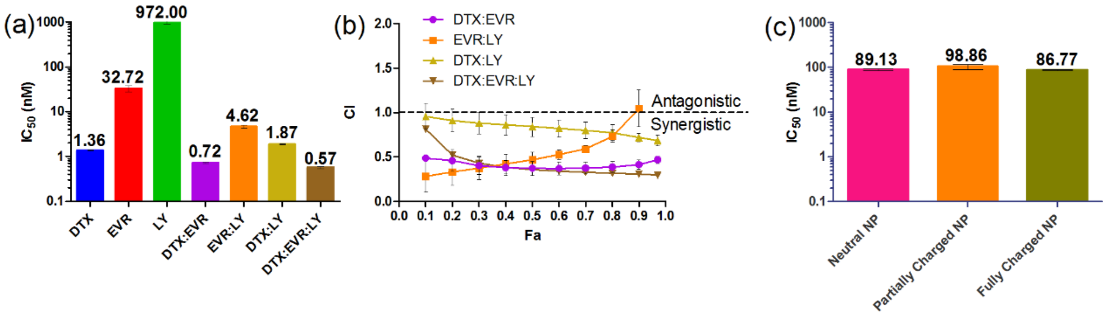

Figure 2.5: IC_{50} values and combination index analysis.

(a) Mean IC_{50} values of DTX, EVR, LY, two- and three-drug combinations in DMSO in A375 metastatic melanoma cells (n = 4). **(b)** Fa vs CI plot of the two- and three- drug combinations in A375 metastatic melanoma cells (n = 4). **(c)** Mean IC_{50} values of three-drug combination neutral, partially charged and fully charged nanoparticles in A375 metastatic melanoma cells (n = 4).

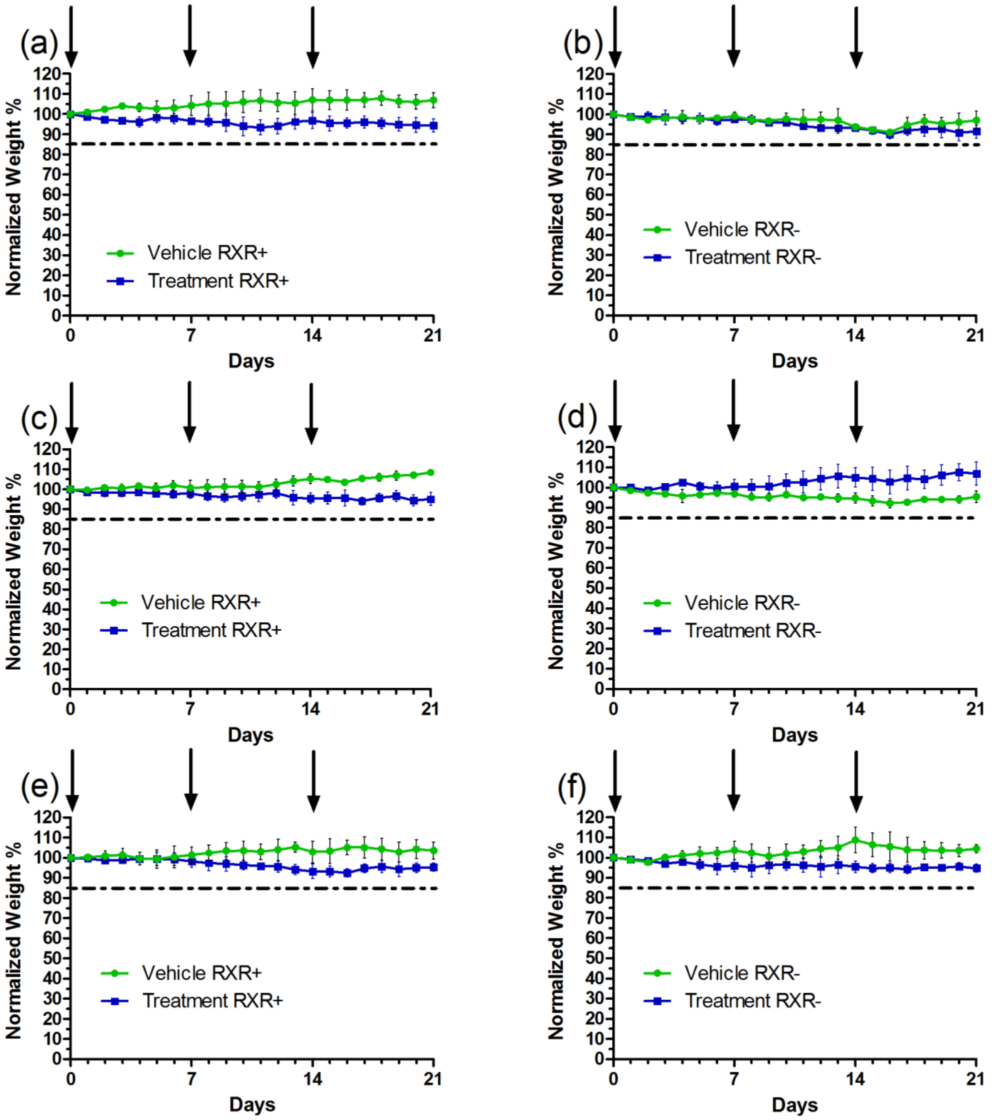

Figure 2.6: Monitoring changes in body weight for toxicity assessment.

Normalized body weight of mice injected subcutaneously with empty or three drug NP in Tyr Nras^{Q61K} RXRα$^{\mathbf{L2/L2}}$ (RXR+) (a, c, and e) and Tyr Nras^{Q61K} RXRα$^{ep-/-}$ (RXR-) (b, d, and f) mice. **(a)** Neutral NP in RXR+ **(b)** and RXR- , **(c)** partially charged NP in RXR+ **(d)** and RXR- mice, **(e)** and fully charged NP in RXR+ **(f)** and RXR- mice. The mice were injected at a dose of 20 mg/kg for each drug in the treatment group and 240 mg/kg of the polymer in all groups. The arrows indicate the days of injection (0, 7, 14). The dashed line depicts the threshold weight loss of 15% which is indicative of acute toxicity. (Mean normalized weight % ± S.D, n=4).

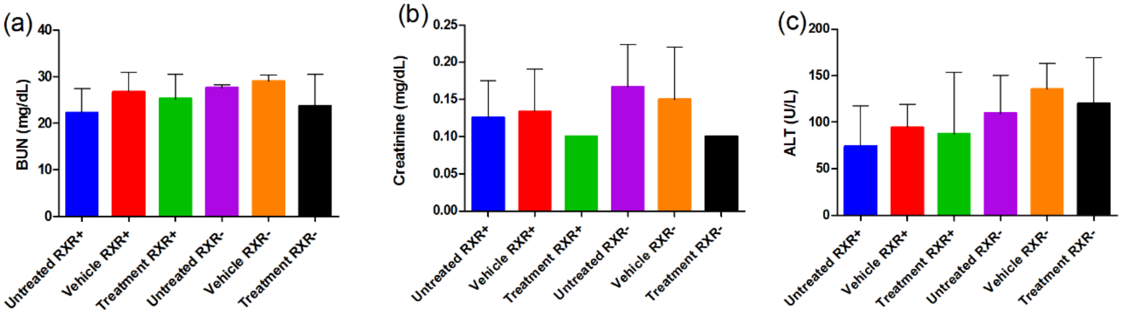

Figure 2.7: Blood panel analysis of mice treated with vehicle and neutral nanoparticles.

Blood panel data from mice injected subcutaneously with vehicle (empty neutral NP) or treatment (three-drug neutral NP) in Tyr NRASs^{Q61K} RXR$\alpha^{L2/L2}$ (RXR+) and Tyr NRAS^{Q61K} RXR$\alpha^{ep-/-}$ (RXR-) mice. **(a)** BUN, **(b)** Creatinine, **(c)** and ALT. Mean parameter value ± S.D, n=4. One way ANOVA with Tukey's Multiple Comparison test was used for statistical analysis at p-value of 0.05.

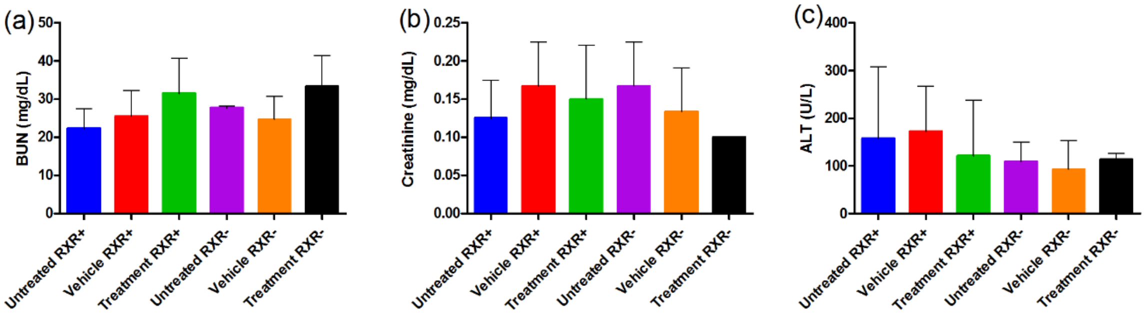

Figure 2.8: Blood panel analysis of mice treated with vehicle and partially charged nanoparticles.

Blood panel data from mice injected subcutaneously with vehicle (empty partially charged NP) or treatment (three-drug partially charged NP) in Tyr NRAS^{Q61K} RXRα$^{L2/L2}$ (RXR+) and Tyr NRAS^{Q61K} RXRα$^{ep-/-}$ (RXR-) mice. **(a)** BUN, **(b)** Creatinine, **(c)** and ALT. Mean parameter value ± S.D, n=4. One way ANOVA with Tukey's Multiple Comparison test was used for statistical analysis at p-value of 0.05.

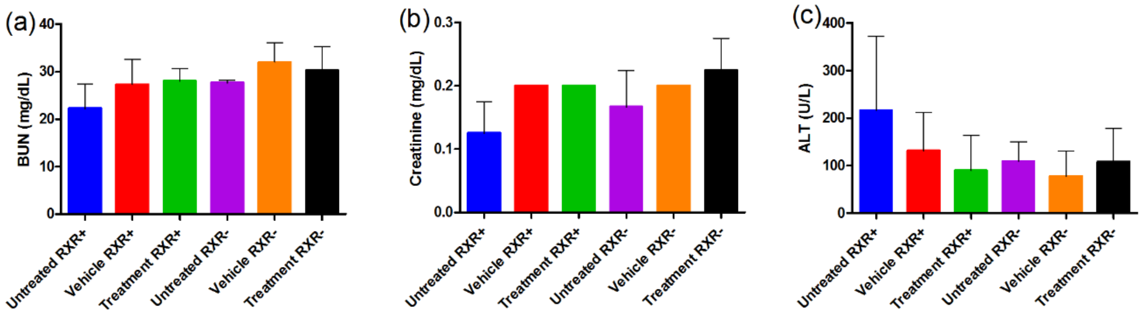

Figure 2.9: Blood panel analysis of mice treated with vehicle and fully charged nano particles.

Blood panel data from mice injected subcutaneously with vehicle (empty fully charged NP) or treatment (three-drug fully charged NP) in Tyr NRAS^{Q61K} RXR$\alpha^{L2/L2}$ (RXR+) and Tyr NRAS^{Q61K} RXR$\alpha^{ep-/-}$ (RXR-) mice. **(a)** BUN, **(b)** Creatinine, **(c)** and ALT. Mean parameter value ± S.D, n=4. One way ANOVA with Tukey's Multiple Comparison test was used for statistical analysis at p-value of 0.05

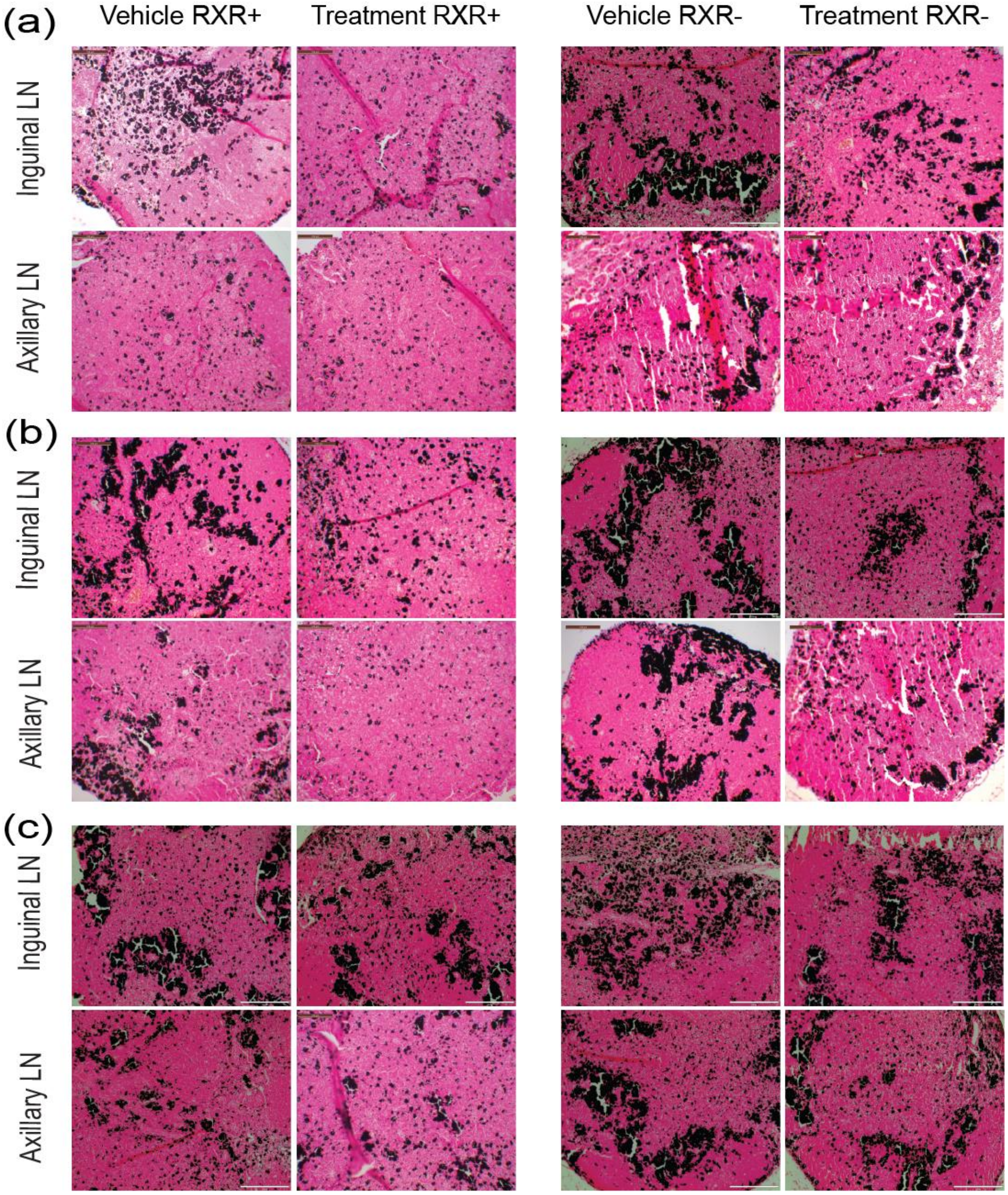

Figure 2.10: Representative images of Fontana Masson staining of lymph node sections.

Representative pictures of FM staining of LN sections after treatment with vehicle (empty NP) or treatment (three-drug NP) in Tyr NRAS^{Q61K} RXR$\alpha^{L2/L2}$ (RXR+) and Tyr NRAS^{Q61K} RXR$\alpha^{ep-/-}$ (RXR-) mice. **(a)** Neutral NP in RXR+ and RXR- mice, **(b)** partially charged NP in RXR+ and RXR- mice, **(c)** and fully charged NP in RXR+ and RXR- mice. The mice were injected at a dose of 20 mg/kg for each drug in the treatment group and 240 mg/kg of the polymer in all groups on days 0, 7, and 14. Scale bar: 100 µm (n = 4).

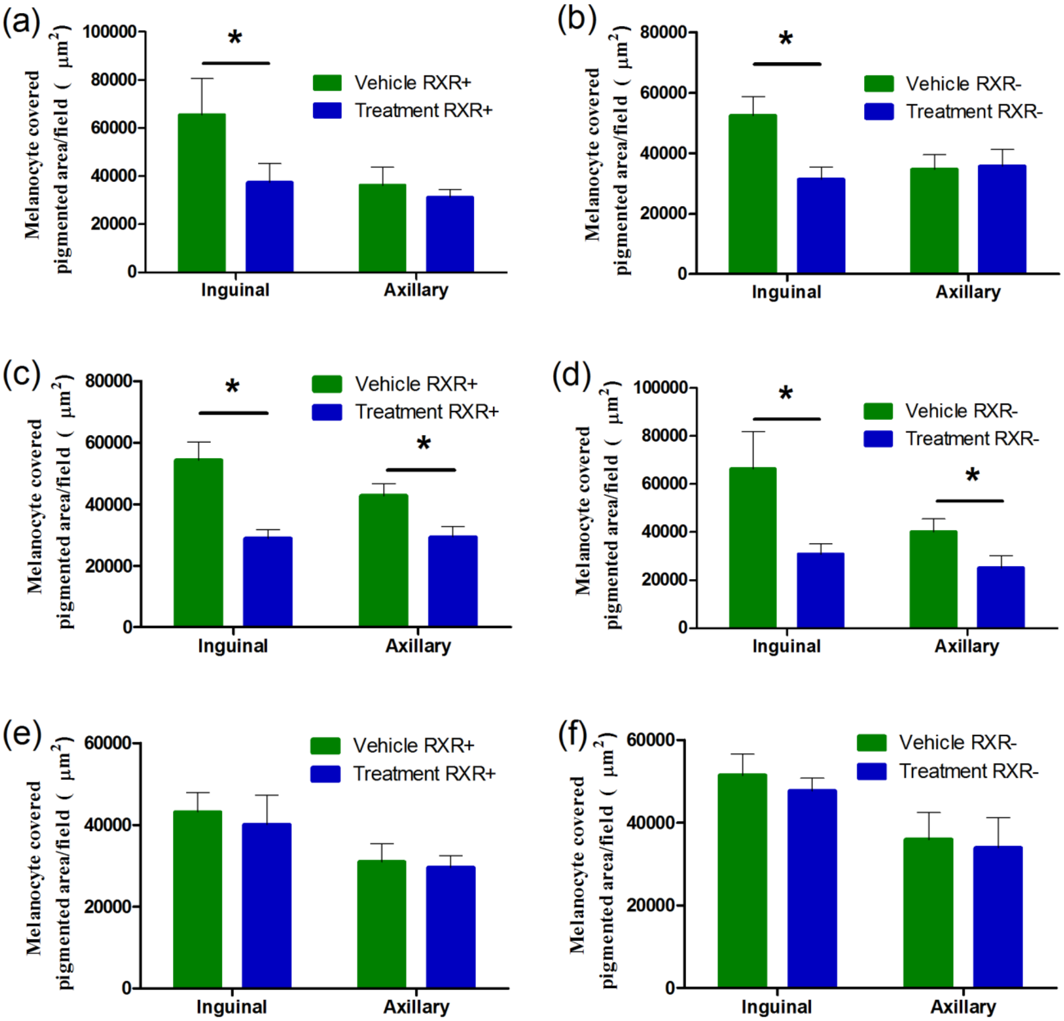

Figure 2.11: Efficacy of the nanoparticles in the two mouse models.

Mean melanocytic pigmented area per field (μm^2) treated with empty or three-drug NP in Tyr NRAS^{Q61K} RXRα$^{L2/L2}$ (RXR+) and Tyr NRAS^{Q61K} RXRα$^{ep-/-}$ (RXR-) negative mice. **(a)** Neutral NP in RXR+ **(b)** and RXR- **(c)** mice, partially charged NP in RXR+ **(d)** and RXR- **(e)** mice, fully charged NP in RXR+ **(f)** and RXR- mice. The mice were injected at a dose of 20 mg/kg for each drug in the treatment group and 240 mg/kg of the polymer in all groups on days 0, 7, and 14. Values are expressed as a mean ± SEM (n =4). *indicates statistical significance as determined by a Student’s two-tailed unpaired t-test with a p-value of 0.05.

	Mean Size ± SD (nm)	PDI ± SD	Mean Zeta Potential (ζ) ± SD (mV)
Neutral NP	48.08 ± 0.31	0.31 ± 0.01	-6.4 ± 0.24
Partially charged NP	48.30 ± 0.42	0.25 ± 0.01	-19.2 ± 2.15
Fully charged NP	48.60 ± 0.66	0.31 ± 0.02	-37.6 ± 1.02

Table 2.1: Particle size and zeta potential of nanoparticles.

Particle Size, PDI, and Zeta potential values for three-drug neutral, partially charged and fully charged NP (Mean ± SD, n = 3)

Drug	% Drug Released at 168 h					
	Neutral NP		Partially Charged NP		Fully Charged NP	
	pH 5.0	pH 7.4	pH 5.0	pH 7.4	pH 5.0	pH 7.4
DTX	72.00 ± 2.16	72.42 ± 2.66	68.55 ± 0.43	75.01 ± 1.78	69.80 ± 1.07	73.60 ± 1.82
EVR	44.58 ± 1.61	51.67 ± 5.83	46.23 ± 0.85	58.23 ± 2.18	48.19 ± 2.85	61.38 ± 4.67
LY	81.18 ± 1.22	81.60 ± 1.39	80.12 ± 1.42	81.90 ± 0.67	80.33 ± 0.52	81.24 ± 2.07

Table 2.2: Percentage drug released at different pH.

The % drug released values for DTX, EVR, and LY in neutral, partially charged, and fully charged NP at pH 5.0 and 7.4 over 168 h. Data presented is Mean ± SD (n = 3)

NP	Drug	pH 5.0			pH 7.4		
		Fast $t_{1/2}$ (h)	Slow $t_{1/2}$ (h)	r^2	Fast $t_{1/2}$ (h)	Slow $t_{1/2}$ (h)	r^2
Neutral NP	DTX	0.42	19.49	0.9924	2.05	23.93	0.9817
	EVR	0.23	28.25	0.9822	0.61	63.20	0.9099
	LY	0.31	5.93	0.9902	0.83	13.72	0.9957
Partially charged NP	DTX	0.42	22.75	0.9865	2.46	26.84	0.9816
	EVR	0.21	31.17	0.9644	0.51	59.53	0.9843
	LY	0.33	5.93	0.9803	0.50	12.83	0.9964
Fully charged NP	DTX	0.53	23.73	0.9936	2.10	25.90	0.9600
	EVR	0.39	27.03	0.9717	0.45	56.38	0.9226
	LY	0.38	5.44	0.9945	0.70	11.41	0.9955

Table 2.3: Release Parameters.

Fast and slow half-lives ($t_{1/2}$) and gTable 1oodness of fit (r^2) values of DTX, EVR, and LY in neutral, partially charged, and fully charged NP at pH 5.0 and 7.4 using a two phase association curve fitting.

CHAPTER 3

Polymeric Micelles as Carriers for Nerve-Highlighting Fluorescent Probe Delivery

Kayla M. Hackman, Bhuvana Shyam Doddapaneni, Connor W. Barth, Igor H. Wierzbicki, Adam G. Alani, Summer L. Gibbs

Molecular pharmaceutics

Published 20 October 2015

12 (12): 4386 - 4394

DOI**:** 10.1021/acs.molpharmaceut.5b00582

3.1 ABSTRACT

Nerve damage during surgery is a common morbidity experienced by patients that leaves them with chronic pain and/or loss of function. Currently, no clinically approved imaging technique exists to enhance nerve visualization in the operating room. Fluorescence image-guided surgery has gained in popularity and clinical acceptance over the last decade with a handful of imaging systems approved for clinical use. However, contrast agent development to complement these fluorescence-imaging systems has lagged behind with all currently approved fluorescent agents providing untargeted blood pool information. Nerve-specific fluorophores are known, however translations of these agents to the clinic has been complicated by their lipophilic nature, which necessitates specialized formulation strategies for successful systemic administration. To date the known nerve-specific fluorophores have only been demonstrated pre-clinically due to the necessity of a dimethyl sulfoxide containing formulation for solubilization. In the current study, a polymeric micellar (PM) formulation strategy was developed for a representative nerve-specific fluorophore from the distyrylbenzene family, BMB. The PM formulation strategy was able to solubilize BMB and demonstrated improved nerve-specific accumulation and fluorescence intensity when the same fluorophore dose was administered to mice utilizing the previous formulation strategy. The success of the PM formulation strategy will be important for moving towards clinical translation of these novel nerve-specific probes as it is nontoxic and biodegradable and has the potential to decrease the necessary dose for imaging while also improving the safety profile.

3.1 INTRODUCTION

Nerve damage following surgery is a continued morbidity experienced by up to 600,000 patients annually in the United States alone. [1] Currently, no clinically approved method exists to enhance nerve visualization in the surgical suite. Fluorescence image-guided surgery has the potential to improve nerve identification and visualization in the operating room as interest in fluorescence image-guided surgery has significantly increased in the past decade. Currently, there are numerous fluorescence image-guided surgery systems in clinical trial or approved for clinical use including an FDA approved fluorescence channel in the da Vinci surgical robot manufactured by Intuitive Surgical. [2-9] However, FDA approved fluorescent contrast agents are limited and the current FDA approved agents are not targeted, but rather act as blood pool agents and do not provide specific fluorescent contrast in nerve tissue.[7]

A limited number of fluorescent contrast agents exist that stain nerve tissue *in vivo*, with varying degrees of nerve-specificity and nerve signal to background ratio reported. Design and development of nerve-specific fluorescent probes is challenging, as the blood nerve barrier (BNB) is a tight junction similar to the blood brain barrier (BBB) where only small molecules less the 500 Daltons can pass freely. Additionally, fluorophores must also have a logarithmic distribution coefficient (Log D at pH 7.4) between 0.5 and 3 to optimally partition from the blood into the nerves. [10] There are currently seven known classes of fluorophores that have been shown to have either nerve or brain specificity when administered systemically, which include nerve-specific peptides and six small molecule fluorophore scaffolds. The nerve-specific peptides are a targeting sequence that largely binds to the epineurium with minimal binding to the endoneurium due to their large size. [11] Nerve-specific contrast is generated using this targeting sequence by conjugating a fluorophore of interest, however fluorescence is only seen on the periphery of nerve tissue diminishing signal to background ratio. Three of the small molecule fluorophores reported to have myelin specificity, including stilbene, coumarin, and tricarbocyanine fluorophores, have only demonstrated specific signal in brain tissue and have not shown nerve-specific fluorescence following systemic administration. [12-14] The small molecule styryl pyridinium fluorophores have been demonstrated to partition into the dorsal nerve root and trigeminal ganglia following systemic administration, but due to the large size of these fluorophores do not highlight all nerve tissue following systemic administration. [15]

To date only two small molecule fluorophore scaffolds have been found to penetrate the BNB and highlight all nerve tissue following systemic administration, which include the distyrylbenzene (DSB) fluorophores and two select oxazine fluorophores. [10,16,17] A library of DSB fluorophore has been previously synthesized and utilized to determine the structure activity relationship of this fluorophore scaffold for nerve specificity (Figure 3.1(a)). [16]

In the current work, 4,4'-[(2-methoxy-1,4-phenylene)-di-(1*E*)-2,1-ethenediyl]bis-benzenamine (BMB), a representative DSB fluorophore was selected for further study. BMB is a small molecule with a molecular weight 342.4 Daltons, Log D of 4.8, and excitation and emission wavelengths of 393 nm and 503 nm, respectively (Figure 3.1(b)).[10] In addition, BMB has an aqueous solubility of 1 µg/mL [18] necessitating a drug delivery system for clinically relevant concentration administration *in vivo*. Initial studies were performed with a co-solvent formulation of 10% dimethyl sulfoxide (DMSO), 5% Cremophor EL, 65% serum, and 20% HEPES buffer to solubilize BMB for intravenous (IV) administration, where nerve-specific fluorescence was demonstrated. [10] However, the co-solvent formulation is not ideal for clinical translation as it is stable at room temperature for less than 30 minutes, and requires the use of DMSO and Cremophor EL, which will hamper future clinical translation due to vehicle toxicity issues. Thus, moving forward a clinically relevant formulation strategy is necessary to fully utilize these derivatives. In the work presented herein a polymeric micellar (PM) formulation strategy has been developed that enhances nerve to muscle ratio over the previously used co-solvent formulation for improved visualization during nerve-sparing surgical procedures.

PM are an excellent drug delivery platform for sparingly soluble compounds. PM are nanoscale colloidal dispersions with particle size between 15–100 nm. [19,20] The building units for PM are amphiphilic block copolymers (i.e., polymers consisting of a hydrophilic segment and a hydrophilic segment) that self-assemble in aqueous environments into spherical structures (micelles) at concentrations equal or above critical micelle concentration. [20] The core of these spherical structures is hydrophobic while the shell is hydrophilic. [21] Sparingly soluble compounds, like BMB, tend to partition into the hydrophobic core of the micelles driven by the hydrophobic interactions between the compound and the polymer hydrophobic segments. [22] Such interactions can significantly increase the water solubility of sparingly soluble small molecules and utilize the core as a depot for these compounds. [23,24] The hydrophilic shell is a physical barrier that prevents micelle aggregation and minimizes micelle-protein interaction (opsonization). Therefore, the shell contributes towards the increased stability, which can then translate into longer blood circulation times for the formulated compound. One of the most common amphiphilic block copolymers that is utilized for PM is methoxy poly (ethylene glycol)-*block*-poly(D,L-lactic acid) (PEG-*b*-PLA) due to its safety, biocompatibility, and biodegradability. Genexol®, a PM formulation of paclitaxel encapsulated in PEG-*b*-PLA is currently in phase II clinical trials for the treatment of advanced non-small cell lung cancer. [25] In this work PEG-*b*-PLA PM has been formulated for the delivery of the BMB fluorophore and compared to the previous co-solvent formulation in *ex vivo* and *in vivo* murine models to evaluate PEG-*b*-PLA PM formulated BMB for nerve-specific imaging capability and feasibility for clinical translation for fluorescence image-guided surgery.

3.3 EXPERIMENTAL SECTION

3.3.1 Materials

Amphiphilic block copolymer PEG(2000)-*b*-PLA(1800) (Mn=3800 Da, MW=4100 Da and PI=1.12) was purchased from Advanced Polymer Materials Inc. (Montreal, Canada). Human Umbilical Vein Endothelial Cells (HUVEC) and endothelial growth medium 2 was purchased from PromoCell (Heidelberg, Germany). Cells were cultured as per the manufacturer instructions and experiments were performed between passages 2 and 6. Abelson murine leukemia virus transformed macrophage cells (RAW 264.7) were purchased from American Type Culture Collection (Manassas, VA). Cell culture supplies including Dulbecco's Modified Eagle medium (DMEM), Fetal Bovine Serum (FBS), Trypsin EDTA, and Penicillin/Streptomycin were purchased from VWR (Radnor, PA). CellTiter-Blue® Cell Viability Assay kit was obtained from Promega Inc. (Madison, WI). All other reagents were of analytical grade and were purchased from VWR International, LLC. (Radnor, PA) or Fisher Scientific Inc. (Fairlawn, NJ) unless stated otherwise below.

3.3.2 Micelle Encapsulation of Nerve-Specific Fluorophore & Release Kinetics

BMB loaded PM were prepared by the solvent casting method. [23] Briefly 2 mg of BMB and 15 mg of PEG-b-PLA were dissolved in 0.5 ml of acetonitrile, which was evaporated under reduced pressure to form a thin dye distributed polymeric film. Micelles were obtained by rehydration of the film with 0.5 ml deionized water. The BMB loading in the micelles was quantified using liquid chromatography mass spectroscopy (LCMS) analysis (Agilent, Santa Clara, CA) as follows. Standard curves for the BMB were obtained using analog signal data from the diode array detector (DAD) at 400 nm to calculate the area under the curve of the identified BMB peak, confirmed by mass to charge ratio from the MS. Briefly, varied concentrations of BMB (10 µL) were injected onto a Poroshell C18 column (Agilent) and separated using a linear gradient from 30% acetonitrile and 70% water to 100% acetonitrile and 0% water over 8 minutes, where BMB had a retention time of 7 minutes. All water and acetonitrile contained 0.1% formic acid. The standard curve was used to convert area under the curve measurements from the DAD into corresponding BMB concentrations. All concentration quantification measurements were performed in triplicate. BMB-PM size was quantified by dynamic light scattering (DLS) using a Malvern Nano ZS (Malvern Instruments Inc., UK). Triplicate samples were prepared for DLS by diluting the micelles 20 fold in DI water to a final concentration of the polymer at 0.1 mg/mL. DLS measurements were collected after equilibration of the micelles in DI water for 2 min.

Freshly prepared BMB-PM samples of 2.5 mL (2 mg/mL) were loaded into a Slide-A-Lyzer® (Thermo Scientific Inc.) 3 mL dialysis cassette with a MWCO of 7,000 g/mol. This MWCO was chosen to enable the free fluorophore along with the unassociated polymer molecules to diffuse freely out of the cassette and thereby ensure sink conditions. Three cassettes were used in each experiment. The cassettes were placed in 2.5 L of 10 mM phosphate buffer at pH 7.4, which was changed every 3 h to ensure sink conditions and the temperature was maintained at 37° C. The sampling time intervals were 0, 0.5, 1, 2, 3, 6, 9, 12, 24, 48 and 72 h. A sample of 100 µL at each time point was withdrawn, and the cassette was replenished with an equal volume of buffer. Samples were analyzed by LCMS for BMB content as described above to quantify free BMB concentration at each time point. The BMB release data from PM was curve-fitted using a two-phase exponential association equation indicative of diffusion and micells dissociation based fluorophore release. The time required to release 50% of the drug ($t_{1/2}$) in two phases, fast and slow, and the goodness of fit (r^2) values of three replicates are presented The curve fitting analysis was performed with GraphPad Prism version 5.04 for Windows, (GraphPad Software, San Diego, CA).

3.3.3 Cell viability studies

HUVEC and RAW 264.7 cell viability in the presence of different concentrations of the BMB-PM solutions was evaluated. HUVEC cells were seeded at the density of 5,000 cells/well in 96-well flat bottom cell culture plates and allowed to attach for 48 h at 37° C. RAW 264.7 cells were seeded, at 10,000 cells/well in a 96-well flat bottom cell culture plates and allowed to attach for 24 h at 5% CO_2 maintained at 37° C. After incubation, cells were treated with different concentrations (10 pM-100 µM) of BMB-PM or Phosphate buffed saline (PBS) as control. Cell viability was determined after 48 h of treatment using 20 µL of CellTiter-Blue® followed by one hour of incubation at 37° C and evaluated for fluorescence at $560_{Ex}/590_{Em}$. All measurements were performed in quadruplicate. The compiled data is presented as mean cell viability ± standard deviation (SD). Significant differences between treatment group means was evaluated using one-way analysis of variance (one-way ANOVA) combined with Dunnette’s post-test analysis, where all columns were compared to the PBS, with a threshold value (p-value = 0.05). The analysis was performed using GraphPad Prism.

3.3.4 Animals

Approval for all animals used in this study was obtained from the Institutional Animal Care and Use Committee (IACUC) at Oregon Health and Science University (OHSU). Male CD-1 mice weighing 22-24g were purchased from Charles River Laboratories (Wilmington, MA). Prior to surgery, mice were anesthetized with an intraperitoneal (IP) injection of a mixture of 9 mg/kg ketamine and 1 mg/kg xylazine (Patterson Veterinary, Devens, MA). All surgeries were terminal and exposed nerve tissues were resected for further analysis by fluorescence microscopy.

3.3.5 Intraoperative Fluorescence Imaging System

A custom-built real-time fluorescence imaging system was used to collect the murine *in vivo* color and nerve-specific fluorescence images. The fluorescence imaging system consisted of a QImaging EXi Blue monochrome camera (Surrey, British Columbia, CA) for fluorescence detection with a removable Bayer filter to collect co-registered color and fluorescence images. A PhotoFluor II (89 North, Burlington, VT) was focused onto the surgical field using a liquid light guide for white light illumination and was filtered for BMB excitation with a 405 ± 20 nm bandpass excitation filter. The emitted light was filtered with a 550 ± 25 nm bandpass emission filter for fluorescence image collection. All filters and beam splitters were from Chroma Technology (Bellows Falls, VT). All fluorescence images were collected using 50 ms exposure time and displayed with equal normalization for quantitative comparison.

3.3.6 Murine Nerve Imaging

BMB dose and biodistribution were previously optimized for mouse studies and utilized herein. [10] BMB (BMB-PM or BMB in the co-solvent) was administered at 0.5 mg/kg IV via tail vein to mice (n=3/group; 5 groups) 4 hours prior to surgical exposure and imaging of the brachial plexus, sciatic nerve, trigeminal ganglia, and optic nerves, as well as the surrounding muscle and adipose tissues. The injection volume in mice varied between 100 – 200 µL. Mice were administered BMB-PM or BMB in the co-solvent formulation as treatments and as controls with blank PM, co-solvent without BMB (blank co-solvent) or were left untreated. [10,16] BMB containing formulations were assessed for nerve signal to background ratio while the BMB negative formulations including untreated mice were used to determine autofluorescence in the nerve, muscle, and adipose tissues. Region of interest analysis was performed at each nerve site to determine the nerve to muscle ratio (N/M) as well as the nerve to adipose ratio (N/A). The mean N/M and N/A ratios for the brachial plexus, sciatic, trigeminal ganglia and optic nerves were calculated from six nerves for each nerve site (2 per mouse) as well as surrounding areas of muscle and adipose tissue for each site.

3.3.7 Ex Vivo Fluorescence Microscopy on Resected Nerve Tissues

Following completion of imaging experiments, the sciatic and brachial plexus nerves from mice (n=3/group; 5 groups) were harvested, fixed with 2% paraformaldehyde (PFA) for 12 hours, snap frozen in optimal cutting temperature (OCT) compound with liquid nitrogen, and stored at -80° C for *ex vivo* studies. Cryosections were cut at 10 µm onto superfrost plus slides (Fisherbrand, Fisher Scientific), mounted with Fluoromount-G (Southern Biotech, Birmingham, AL) and cover slipped prior to microscopy. Images were acquired on an Axio Observer inverted fluorescence microscope (Zeiss, Thornwood, NY) at 20x magnification. A Photofluor II was used for phase contrast images as well as filtered using a 405 ± 20 nm bandpass excitation filter for BMB excitation. Images were collected using an Axiocam 506 camera (Zeiss) where a 550 ± 25 nm bandpass emission filter was used for fluorescence image collection. All images were collected at 1000 ms exposure time and displayed with equal normalization. A group of 10 representative regions of nerve and background were analyzed for each brachial plexus and sciatic nerve image to calculate the nerve to background ratio and standard deviation for each administration group.

3.3.8 Ex Vivo Nerve-Specific BMB Staining

Ex vivo nerve-specific BMB staining was completed as previously reported, [10,16] and is described briefly as follows. Brachial plexus and sciatic nerve tissue from untreated mice were collected, fixed with 2% PFA for 12 hours and then snap frozen in OCT with liquid nitrogen. 10 μm tissue sections were cut onto super frost plus slides. The tissue sections were washed once with PBS (2 minutes), fixed with 2% PFA (15 minutes), and then again washed with PBS (3 x 5 minutes). The tissue sections were incubated with BMB in the co-solvent formulation (n=3) or BMB-PM (n=3) at 100 μM for 20, 40, and 60 minutes at room temperature. A mixture of co-solvent formulation not containing BMB was used to wash the sections following fluorophore incubation (2 x 5 minutes) followed by additional washes with PBS (2 x 5 minutes). All stained slides were mounted using Fluoromount-G and imaged with the microscope as described above. All images were acquired at 10 ms exposure time and displayed with equal normalization.

3.3.9 Statistical Analysis

Significant differences between treatment group means was evaluated using one-way ANOVA to compared all *in vivo* mean N/M and N/A ratios as well as the *ex vivo* mean nerve to background ratio from the resected tissues using GraphPad Prism. The means were compared between groups including BMB-PM, BMB in co-solvent, blank micelle, blank co-solvent, and untreated. Significant differences between the mean nerve to background ratio from the *ex vivo* nerve-specific staining using the BMB-PM vs. the BMB in co-solvent were compared using unpaired two sided t-tests. All statistical analysis was performed with GraphPad Prism.

3.4 RESULTS

3.4.1 Micelle Encapsulation of Nerve-Specific Fluorophore & Release Kinetics

PEG-*b*-PLA PM were formulated and loaded with BMB. The BMB-PM micelles were able to solubilize BMB at 2.00 ± 0.55 mg/mL (100% loading efficiency). BMB-PM were stable at 25° C for more than 30 days with more than 99% of the fluorophore retained in solution. BMB-PM were sized at 21.99 ± 0.06 nm (PDI = 0.113 ± 0.013). BMB-PM micelles demonstrated unimodal distribution with PDI values of less than 0.2. BMB release from the BMB-PM micelles was assessed by dialysis in phosphate buffer over 72 h under sink conditions where 73.7% ± 2.6% of the fluorophore release occurred within 72 h (Figure 3.2(a)). Based on the two phase exponential association curve fitting the initial phase shows rate constant of 1.93. h^{-1} and half-life of 0.96 h while for the second phase has rate constant of 0.018 h^{-1} and half-life of 38.77 h with r^2 value of 0.9934. In addition we anticipate that the release *in vivo* will be faster due to the presence of plasma proteins.

3.4.2 Cell Viability Status

The effect of the BMB-PM on cell viability was assessed in HUVEC and RAW 264.7 cells (Figure 3.2(b) and 3.2(c)). No significant effect on HUVEC cell viability was seen until a 1 μM concentration of BMB was achieved. While in RAW 264.7 cells there was no effect on cell viability until the BMB concentration of 100 μM was achieved. *In vivo* fluorophore concentrations reaching 100 μM are not anticipated due to the dynamic clearance mechanisms.

3.4.3 Murine Nerve Imaging

Previous dose and biodistribution studies using BMB demonstrated maximum N/M ratio four hours after administration of 0.5 mg/kg BMB per mouse. [10] Mice were IV administered a 0.5 mg/kg dose of BMB in the co-solvent formulation (Figure 3.3(a)) or BMB-PM (Figure 3.3(b)). Four hours after IV fluorophore administration, the brachial plexus, sciatic nerve, trigeminal ganglia, and optic nerves were exposed for imaging. Color and fluorescence images of each nerve site were collected at 50 ms exposure time for equal comparison across nerve sites and formulations. Higher nerve fluorescence intensity was seen at all selected nerve sites for the BMB-PM as compared to BMB in the co-solvent (Figures 3.3(a) and 3.3(b)).

To determine if any tissue specific fluorescence signal was contributed by the formulations, mice were IV administered equivalent amounts of blank co-solvent formulation (Figure 3.3(c)) or blank PM (Figure 3.3(d)) 4 hours prior to imaging. Autofluorescence at each of the nerve sites was also imaged on untreated control mice to quantify the contribution of tissue autofluorescence at the imaged wavelengths (Figure 3.3(e)). Minimal nerve autofluorescence was seen in the blank co-solvent formulation (Figure 3.3(c)), blank PM (Figure 3.3(d)), and untreated control mice (Figure 3.3(e)). Of note, nerve fluorescence was found to be nearly equivalent across the four nerve structures for control mice with blank PM, blank co-solvent and untreated mice demonstrating the neither formulation strategy contributed to nerve-specific fluorescence.

The N/M and N/A fluorescence ratios were quantified for each administration group at each nerve site including the brachial plexus, sciatic, trigeminal ganglia and optic nerves. The N/M ratio was significantly higher at all nerve sites for the BMB-PM injected mice than for the BMB in co-solvent injected mice ($p < 0.0001$, Figure 3.4(a)). In the BMB-PM injected mice the N/M ratio was highest for the sciatic nerve (5.21 ± 0.68) followed by the trigeminal ganglia (4.86 ±0.92), brachial plexus (4.10 ± 0.59) and optic nerves (3.57 ± 0.27). In the BMB in co-solvent injected mice the N/M ratio was highest for the trigeminal ganglia (2.83 ± 0.53), followed by the sciatic nerve (2.47 ± 0.54), optic nerve (2.40 ± 0.27) and brachial plexus (2.23 ± 0.54). When the N/M ratio was compared to average fluorescence intensity in the control blank PM, blank co-solvent and untreated animals across nerve sites the BMB-PM was 3x higher than control autofluorescence while the BMB in co-solvent was 1.7x higher than control autofluorescence (Figure 3.4(a)). Little fluorescence difference was seen between the three control groups with no statistically significant difference between the mean N/M fluorescence. The N/A fluorescence ratio was similar between the two formulation strategies ($p = 0.77$, Figure 3.4(b)). In both the BMB PM and BMB in co-solvent the N/A ratio was highest in the trigeminal ganglia (BMB in co-solvent = 1.20 ± 0.41, BMB PM = 1.18 ± 0.37) followed by the optic nerve (BMB in co-solvent = 1.01 ± 0.30, BMB PM = 0.93 ± 0.23), brachial plexus (BMB in co-solvent = 0.56 ± 0.14, BMB PM = 0.73 ± 0.15) and sciatic nerve (BMB in co-solvent = 0.61 ± 0.08, BMB PM = 0.53 ± 0.16).

3.4.4 Ex Vivo Fluorescence Microscopy.

Following completion of the *in vivo* nerve imaging studies, all brachial plexus and sciatic nerve tissues were resected and flash frozen for *ex vivo* quantification by fluorescence microscopy. Representative phase contrast and fluorescence images of the brachial plexus and sciatic nerve tissues from mice administered BMB in the co-solvent formulation and BMB-PM as well as mice administered the blank co-solvent, blank PM, and untreated control are shown in Figure 3.5(a). In untreated mice and blank controls a weak fluorescence background signal was seen in the nerve tissues, while significant nerve fluorescence was seen in the BMB injected animals. Fluorescence intensity was quantified in both the brachial plexus and sciatic nerves for each formulation group. Similar to the *in vivo* results, nerve to background fluorescence was significantly higher in the BMB-PM mice as compared to the BMB in the co-solvent injected mice ($p < 0.0001$) with little autofluorescence seen in the blank co-solvent, blank PM or untreated control mouse nerve tissues (Figure 3.5(b)).

3.4.5 Ex Vivo Nerve-Specific Staining of Micelle Encapsulated vs. Co-solvent Formulated Fluorophore

Brachial plexus and sciatic nerve tissue from untreated mice was used to examine the difference in fluorescence intensity following *ex vivo* BMB staining when BMB-PM or BMB in the co-solvent were used. Nerve tissues were stained using the previously developed *ex vivo* staining assay, [10,16] where the fluorophore incubation time was varied to include 20, 40, and 60 minutes to examine the effect of incubation time on the fluorescence intensity. Significantly greater nerve-specific fluorescence was seen using the BMB-PM as compared to BMB in the co-solvent in both the brachial plexus and sciatic nerve tissue sections (p = 0.01) as demonstrated by the lack of visible fluorescence in the BMB in co-solvent incubated slides when images were acquired with the same exposure time and displayed with equal normalizations (Figure 3.6(a) and 3.6(b)). Nerve to background ratio was quantified for both nerves at each incubation time and found to linearly increase with incubation time for both formulations (Figure 3.6(c) and 3.6(d)). The nerve to background ratio was 5-10x greater for the BMB-PM as compared to BMB in the co-solvent formulation at all three incubation times.

3.5 DISCUSSION

Nerve damage is a major morbidity experienced by patients that undergo numerous surgical procedures. This difficulty stems from the nature of the nerve tissue, which is generally small and translucent as well as the fact that nerves are typically protected deep within layers of surrounding tissue making them difficult to detect and visualize prior to injury or transection in surgery. Currently no clinically available imaging tool exists to enhance nerve visualization in the operating room. With the increased focus on fluorescence image-guided surgery as well as the approval of a select few imaging systems for clinical use, there is an opportunity to improve nerve visualization though fluorescence imaging in the surgical suite. However, few nerve-specific fluorescent contrast agents exist and given the lipophilic nature of nerve tissue, systemic administration of these agents has proven challenging. To date, two select small molecule fluorophore scaffolds have been demonstrated to provide nerve-specific fluorescence in all nerve tissue following systemic administration in a co-solvent formulation that is not suited for clinical translation due to its potential toxicity and reliance on DMSO, which is not FDA approved. [10,16,17,26] Development of a formulation strategy with the potential for nontoxic clinical translation would significantly improve the prospects of using specific probes from either of these nerve-specific fluorophore scaffold families for fluorescent nerve-specific image-guided surgery.

In the current work, the previously used DMSO containing co-solvent formulation was compared to a nontoxic PM formulation *in vivo* and *ex vivo* to assess the effect of formulation strategy on nerve-specific fluorophore accumulation. The previously characterized co-solvent formulation containing Cremophore EL and DMSO is capable of solubilizing BMB at 5 mg/mL but is not a viable clinical option for surgical use. [26] BMB-PM was formulated in a biodegradable, biocompatible polymer, which has an extensively documented safety profile in humans. [20,21] *In vitro* release profile of the BMB from the PM (Figure 3.2(a)) and the curve fitting analysis shows that BMB release form the polymeric micelles is bi-phasic which is consist of initial phase involving burst/rapid release of the BMB followed by a more sustained release pattern at later state. This biphasic release pattern exhibited by polymeric micelles and nanoparticales has been well documented in the literature. The initial burst release is primarily driven by the desorption and diffusion of surface adsorbed drug, while the secondary phase of drug release is driven by the dissociation of the polymeric matrix and drug diffusion processes. *In vitro* cell viability assessment in the presence of BMB-PM in two primary cell lines indicated that no effect on viability was seen below 100 µM depending on the sensitivity of the cells (Figure 3.2(b) and 3.2(c)). Systemic administration of the BMB-PM for *in vivo* study is at a lower concentration, thus the accumulated concentration in any one cell is less than the determined toxic dose of the BMB PM formulation. Consequently, we do not anticipate systemic toxicity *in vivo* due to the dynamic nature of clearance mechanisms and the unlikelihood of a tissue being exposed to toxic levels of BMB-PM concentrations prior to clearance from the body. Therefore, the BMB-PM formulation offers a safer, and more effective alternative to the previously utilized co-solvent system.

In addition to its improved safety profiles, the BMB-PM significantly improved nerve-specific accumulation of the fluorophores. *In vivo* studies comparing BMB-PM and BMB in the co-solvent demonstrated increased nerve-specific fluorescence in the BMB-PM group following administration of the same dose of fluorophore in both formulations (Figure 3.3 and 3.4). Interestingly the nerve fluorescence was greatly increased in the BMB-PM injected animals as compared to the BMB in co-solvent injected animals while the muscle fluorescence remained largely the same in both cohorts, accounting for the increased N/M ratio in the BMB-PM group. By comparison the adipose fluorescence also increased in the BMB-PM injected animals, thus the N/A ratio was found to be similar between the BMB-PM and BMB in co-solvent injected groups. Although the PM formulation strategy did not improve the N/A ratio, it did not significantly alter it from what was seen in the BMB in co-solvent administered group. The adipose accumulation seen using both formulation strategies likely has little to do with the formulation strategy itself and is rather a property of the fluorophore, which has a lipophilic Log D (Log D = 4.8 at pH 7.4) accounting for the adipose accumulation. By comparison the BMB-PM demonstrated 3x the N/M contrast over control tissue autofluorescence while the BMB in co-solvent had only 1.7x the N/M contrast over control tissue. This increase in nerve-specific fluorophore accumulation may stem from a potentially longer blood circulation time of the fluorophore when PM encapsulated vs. solubilized in the co-solvent. Thus, overall the N/M fluorescence was significantly increased in the BMB-PM group as compared to BMB in the co-solvent group ($p < 0.0001$) without an increase in fluorophore dose (Figure 3.4). Future study will be performed to evaluated the blood circulation and biodistribution of the BMP-PM, this data will give us a better insight about the BMB stability and distribution in the body

As expected, when the resected nerve tissue was examined microscopically, nerve to background fluorescence was significantly higher in the BMB-PM group as compared to BMB in the co-solvent group ($p < 0.0001$, Figure 3.5). Of note, when *ex vivo* staining was performed a linear increase in fluorescence intensity was seen in both the BMB-PM and BMB in co-solvent groups, however the fluorescence intensity of the BMB-PM group was significantly greater than that of the BMB in co-solvent group ($p = 0.01$, Figure 3.6). Again a possible explanation for this observation is improved availability of the fluorophore to the nerve tissue through improved solubility using the PM over the co-solvent formulation which was demonstrated both in the blood (*in vivo*) as well as in solution (*ex vivo* staining study).

In summary, a micellar formulation for BMB has been successfully developed and characterized improving the feasibility of clinical translation of this nerve specific fluorophore for fluorescence image-guided surgery through an improved safety profile. Another attractive feature of the PM formulation strategy for clinical translation is the enhanced N/M ratio following administration of BMB-PM as compared to BMB in the co-solvent formulation without increasing fluorophore dose, an important consideration for clinical safety. The increase in N/M ratio provides the opportunity to lower fluorophore dose while creating equivalent N/M ratio of that seen with the co-solvent formulation further improving the safety profile. Future work lies in scaling up the formulation, studies in larger animal model such as swine, translation of the formulation strategy to other promising nerve-specific fluorophores within the two known nerve-specific families and fully characterizing the formulation for complete pre-clinical assessment.

3.6 ACKNOWLEDGEMENTS

We would like to thank Brandon Lei for experiment assistance. This study was supported by grants from the National Institute of Health NIBIB K01EB010201 (SLG), the Oregon Clinical and Translational Research Institute (SLG) at Oregon Health and Science University and Oregon State University Start-up Funding (AGA).

3.7 REFERENCES

[1] Burke, S. & Shorten, G.D. When pain after surgery doesn't go away. *Biochem Soc Trans* **37**, 318-322 (2009).

[2] Keereweer, S. et al. Optical image-guided surgery--where do we stand? *Molecular imaging and biology : MIB : the official publication of the Academy of Molecular Imaging* **13**, 199-207 (2011).

[3] Frangioni, J.V. New technologies for human cancer imaging. *Journal of clinical oncology : official journal of the American Society of Clinical Oncology* **26**, 4012-4021 (2008).

[4] van Dam, G.M. et al. Intraoperative tumor-specific fluorescence imaging in ovarian cancer by folate receptor-alpha targeting: first in-human results. *Nature medicine* **17**, 1315-1319 (2011).

[5] Gioux, S., Choi, H.S. & Frangioni, J.V. Image-guided surgery using invisible near-infrared light: fundamentals of clinical translation. *Molecular imaging* **9**, 237-255 (2010).

[6] Ntziachristos, V., Yoo, J.S. & van Dam, G.M. Current concepts and future perspectives on surgical optical imaging in cancer. *Journal of biomedical optics* **15**, 066024 (2010).

[7] Gibbs, S.L. Near infrared fluorescence for image-guided surgery. *Quantitative imaging in medicine and surgery* **2**, 177-187 (2012).

[8] Vahrmeijer, A.L., Hutteman, M., van der Vorst, J.R., van de Velde, C.J. & Frangioni, J.V. Image-guided cancer surgery using near-infrared fluorescence. *Nature reviews. Clinical oncology* **10**, 507-518 (2013).

[9] Keereweer, S. et al. Optical image-guided cancer surgery: challenges and limitations. *Clinical cancer research : an official journal of the American Association for Cancer Research* **19**, 3745-3754 (2013).

[10] Gibbs-Strauss, S.L. et al. Nerve-highlighting fluorescent contrast agents for image-guided surgery. *Molecular imaging* **10**, 91-101 (2011).

[11] Whitney, M.A. et al. Fluorescent peptides highlight peripheral nerves during surgery in mice. *Nature biotechnology* **29**, 352-356 (2011).

[12] Wang, C. et al. In situ fluorescence imaging of myelination. *The journal of histochemistry and cytochemistry : official journal of the Histochemistry Society* **58**, 611-621 (2010).

[13] Wang, C. et al. Longitudinal near-infrared imaging of myelination. *The Journal of neuroscience : the official journal of the Society for Neuroscience* **31**, 2382-2390 (2011).

[14] Wu, C. et al. Molecular probes for imaging myelinated white matter in CNS. *Journal of medicinal chemistry* **51**, 6682-6688 (2008).

[15] Gibbs-Strauss, S.L. et al. Molecular imaging agents specific for the annulus fibrosus of the intervertebral disk. *Molecular imaging* **9**, 128-140 (2010).

[16] Gibbs, S.L. et al. Structure-activity relationship of nerve-highlighting fluorophores. *PloS one* **8**, e73493 (2013).

[17] Park, M.H. et al. Prototype nerve-specific near-infrared fluorophores. *Theranostics* **4**, 823-833 (2014).

[18] ACD/Labs in Advanced Chemistry Development, Edn. Version 14.0.0 (ACD/Labs, Toronto, Ontario, Canada; 2014).

[19] Torchilin, V.P. Structure and design of polymeric surfactant-based drug delivery systems. *Journal of controlled release : official journal of the Controlled Release Society* **73**, 137-172 (2001).

[20] Kwon, G.S. Polymeric micelles for delivery of poorly water-soluble compounds. *Critical reviews in therapeutic drug carrier systems* **20**, 357-403 (2003).

[21] Adams, M.L., Lavasanifar, A. & Kwon, G.S. Amphiphilic block copolymers for drug delivery. *Journal of pharmaceutical sciences* **92**, 1343-1355 (2003).

[22] Lu, Y. & Park, K. Polymeric micelles and alternative nanonized delivery vehicles for poorly soluble drugs. *International journal of pharmaceutics* **453**, 198-214 (2013).

[23] Mishra, G.P., Doddapaneni, B.S., Nguyen, D. & Alani, A.W. Antiangiogenic effect of docetaxel and everolimus as individual and dual-drug-loaded micellar nanocarriers. *Pharmaceutical research* **31**, 660-669 (2014).

[24] Mishra, G.P., Nguyen, D. & Alani, A.W. Inhibitory effect of paclitaxel and rapamycin individual and dual drug-loaded polymeric micelles in the angiogenic cascade. *Molecular pharmaceutics* **10**, 2071-2078 (2013).

[25] Ahn, H.K. et al. A phase II trial of Cremorphor EL-free paclitaxel (Genexol-PM) and gemcitabine in patients with advanced non-small cell lung cancer. *Cancer chemotherapy and pharmacology* **74**, 277-282 (2014).

[26] Montaguti, P., Melloni, E. & Cavalletti, E. Acute intravenous toxicity of dimethyl sulfoxide, polyethylene glycol 400, dimethylformamide, absolute ethanol, and benzyl alcohol in inbred mouse strains. *Arzneimittel-Forschung* **44**, 566-570 (1994).

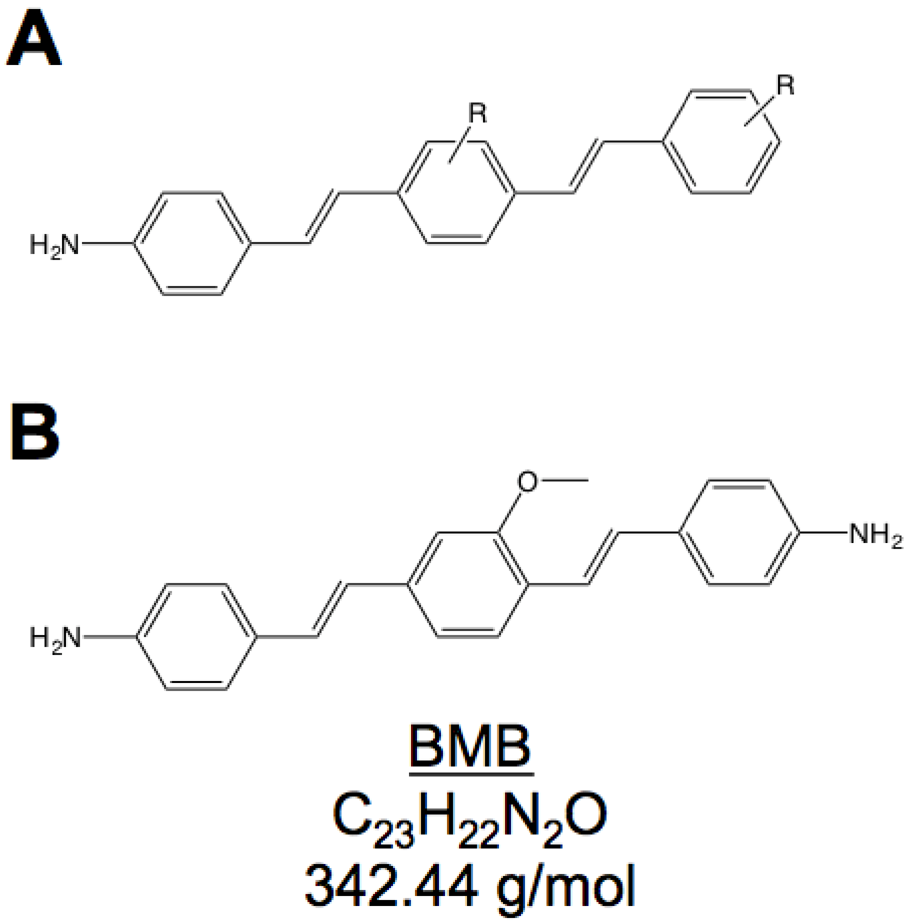

Figure 3.12: Structure of DSB and BMB.

(a) The DSB fluorophore scaffold has been investigated for nerve-specificity with fluorophores of the para-configuration showing the highest nerve-specific accumulation. [16] **(b)** BMB is an example of a para-configuration of DSB and was utilized in the current study.

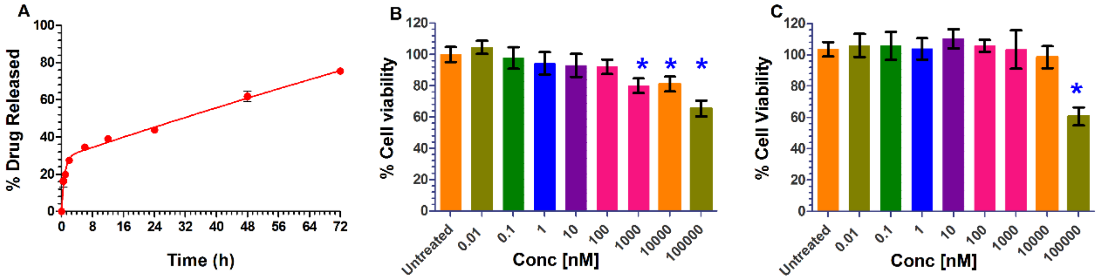

Figure 13.2: Release Data and In-vitro toxicity assessment.

(a) Release kinetics of the BMB from PM measured over 72 hours (n=3). BMB micelle toxicity was assessed using Cell Titer Blue® assay for concentrations of BMB ranging from 10 pM – 100 µM in **(b)** HUVEC and **(c)** RAW 264.7 cells.

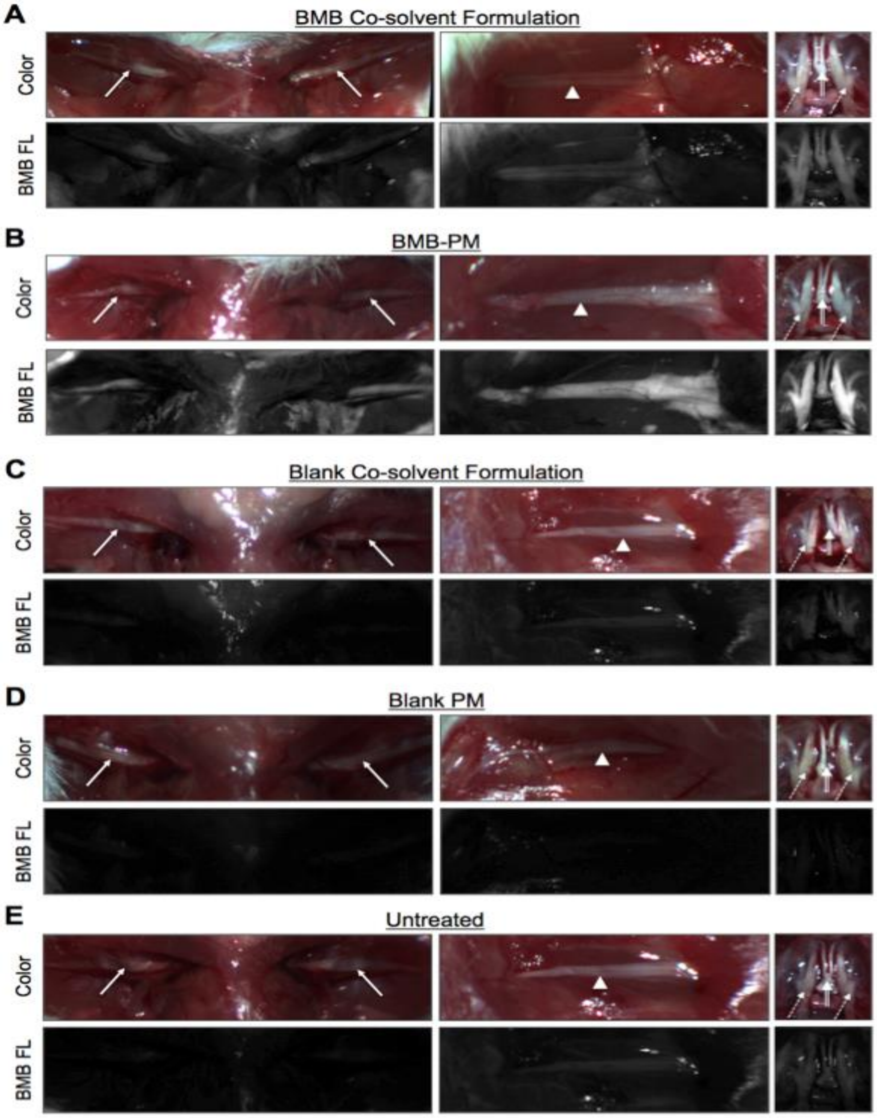

Figure 3.3: Representative fluorescent images before and after administration of BMB micelles and BMB in DMSO.

Representative color and fluorescence images (BMB FL) of mice administered 0.5 mg/kg BMB in **(a)** the co-solvent formulation or **(b)** BMB-PM. Representative color and fluorescence images of mice administered **(c)** blank co-solvent formulation and **(d)** blank PM. **(e)** Representative color and fluorescence images of untreated control mice. All images are representative of data collected for n=3 mice per administration strategy. All fluorescence images were collected using 50 ms exposure time and are displayed with equal normalization. Brachial plexus = arrow, sciatic nerve = arrowhead, trigeminal ganglia = dashed arrow, optic nerve = double lined arrow.

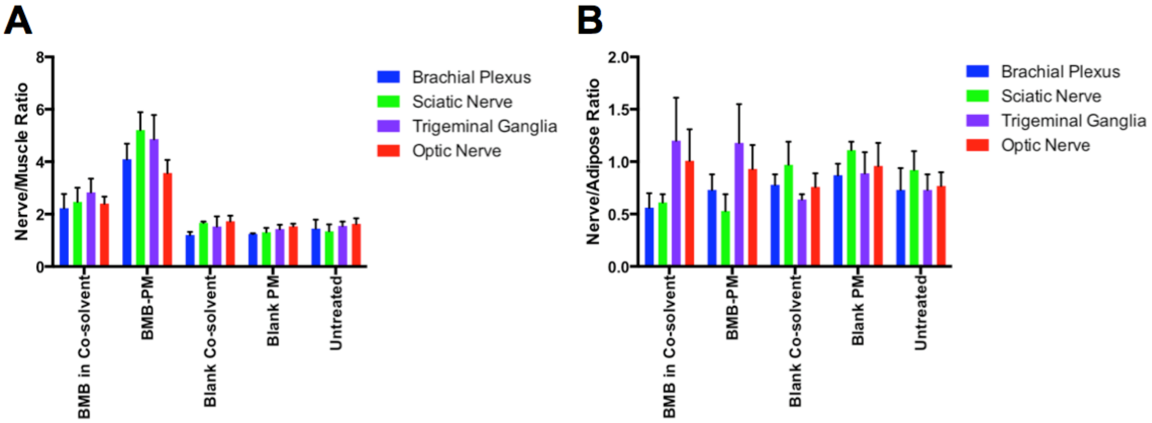

Figure 3.4: Nerve to muscle (N/M) and nerve to adipose (N/A) ratios.

(a) The mean nerve to muscle (N/M) ratio and standard deviation and **(b)** mean nerve to adipose (N/A) ratio and standard deviation were calculated at using region of interest analysis for the brachial plexus, sciatic nerve, trigeminal ganglia, and optic nerves for each animal.

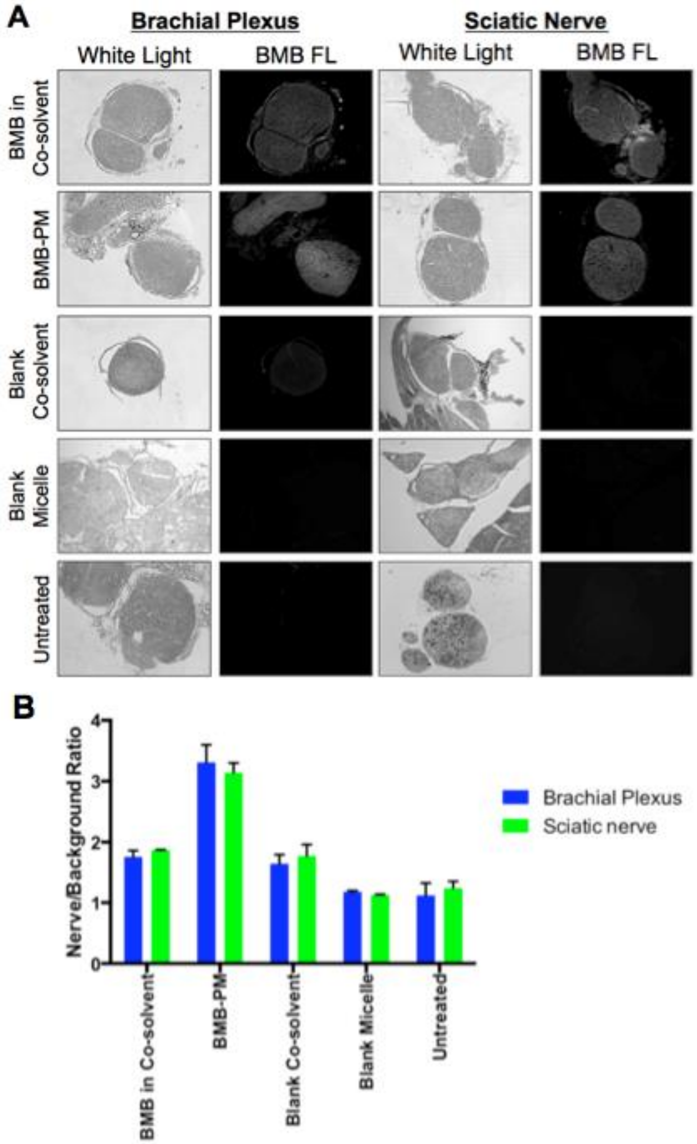

Figure 3.5: Representative fluorescent images and nerve to background ratio.

All brachial plexus and sciatic nerve tissue was resected from n=3 mice per administration group. **(a)** Representative white light and fluorescence images (BMB FL) of a brachial plexus and sciatic nerve from each administration group are shown. All fluorescence images were collected at 1000 ms exposure time and are displayed with equal normalization. **(b)** Nerve to background ratio was calculated for each mouse and for each formulation strategy. The average and standard deviation of the nerve to background ratio is shown for the brachial plexus and sciatic nerves.

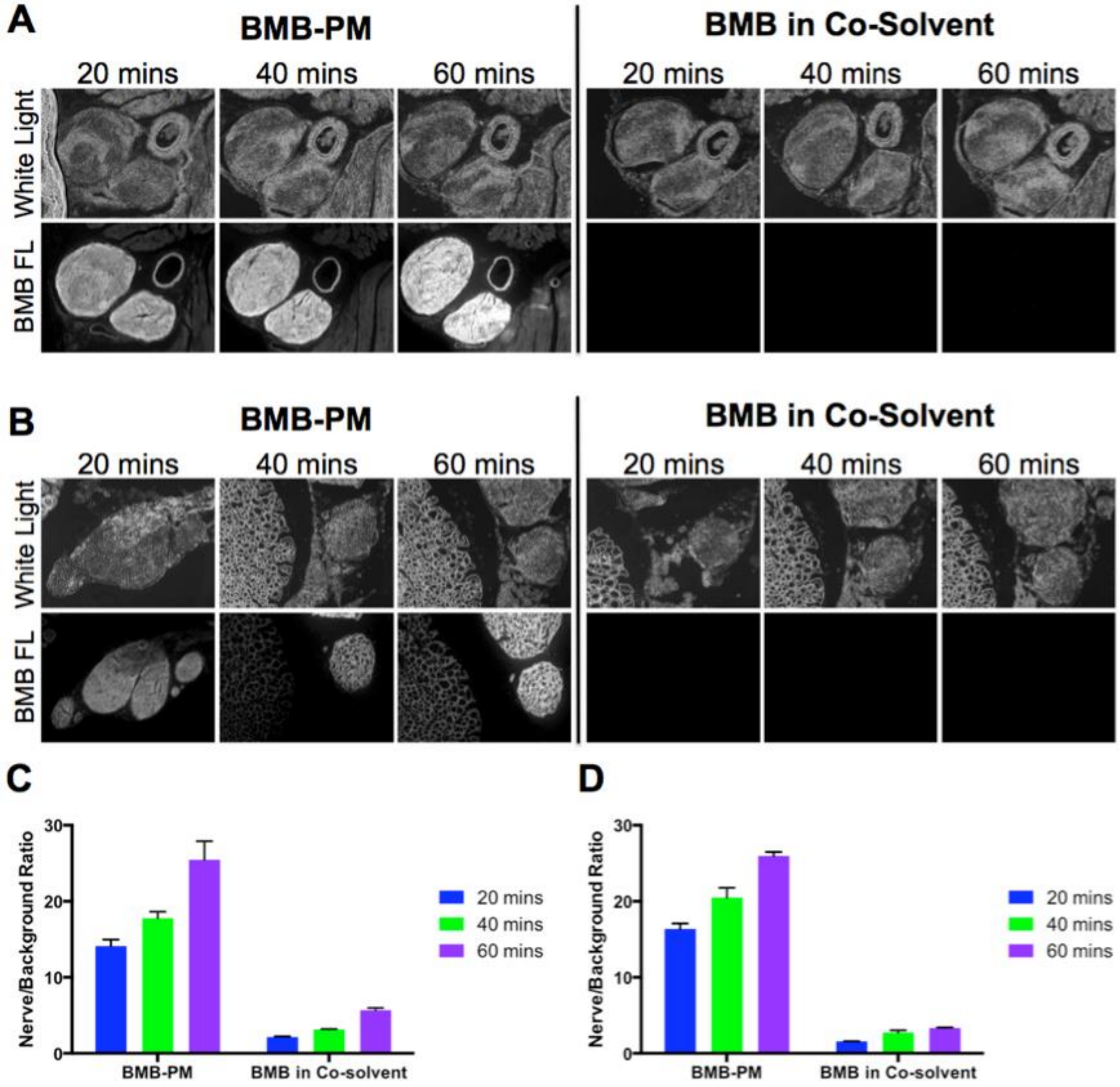

Figure 3.6: Effectiveness of the BMB micelle over its DMSO formulation.

Resected unstained mouse **(a)** brachial plexus and **(b)** sciatic nerve tissue was stained using 100 μM micelle encapsulated or co-solvent formulated BMB. Nerve sections were incubated with BMB for 20, 40, or 60 minutes. White light and fluorescence images (BMB FL) were collected. All fluorescence images were collected at 10 ms exposure time and are displayed with equal normalization. Nerve to background ratio was calculated for the micelle encapsulation vs. the co-solvent formulation incubated for 20, 40 or 60 minutes on the **(c)** brachial plexus or **(d)** sciatic nerve tissue sections.

CHAPTER 4

A Combinatorial therapy targeting HIF and mTOR signaling pathways for treating angiogenesis and ovarian cancer

Bhuvana S. Doddapaneni, Kinser Reed, Adel Fatease, Deepa A. Rao, Adam W. G. Alani

(Submitted to Nanoscale)

4.1 ABSTRACT

Mutations in the tumor protein (TP53) and the mammalian target of rapamycin (mTOR) pathway have been elucidated as driver mutations in ovarian carcinomas that transform into an invasive phenotype under hypoxic conditions. Chetomin (CHE) targets the hypoxic pathway while Everolimus (EVR) acts on the mTOR pathway. Poor aqueous solubilities of both compounds limits their clinical applications. Diblock copolymer nanoplatforms of methoxy poly(ethylene glycol)$_{2000}$-*block*-poly (lactic acid)$_{1800}$ (mPEG$_{2000}$-*b*-PLA$_{1800}$) and (mPEG$_{4000}$-*b*-PLA$_{2200}$) were used to formulate individual and dual drug loaded micelles (DDM) using the solvent evaporation method. The CHE micelles (CHE-M) had a size of 21 nm with CHE loading of 0.5 mg/mL while the EVR micelles (EVR-M) and the DDM had a size around 35 and 39 nm respectively with EVR loading up to 2.3 mg/mL. The anti-proliferative effects of these micelles have been tested *in vitro* in three ovarian cell lines (ES2, OVCAR3 and TOV21G) with the DDM exhibiting a strong synergistic anti-proliferative effect in the ES2 and the TOV21G cells. The DDM were able to significantly induce tumor regression in ES2 ovarian xenograft mouse models by inhibiting angiogenesis and inducing apoptosis when compared to the individual micelles. The inhibition of Hypoxia inducible factor (HIF) and the mTOR pathways has been elucidated using immunohistochemistry studies. In conclusion, we have developed mPEG-*b*-PLA based micellar nanoplatform that could prevent drug resistance by delivering multiple drugs at therapeutically relevant concentrations for effectively treating ovarian carcinomas.

4.2 INTRODUCTION

Ovarian cancer (OC) is one of the leading causes of cancer death among women, [1,2] with an estimated diagnosis of 220,000 new cases per year around the world with 14,000 of them in the U.S alone. [3] A majority of the diagnosed ovarian cancers (90%) comprise of epithelial ovarian carcinomas (EOC's) that are believed to originate from the gynecological epithelia. [2] EOC's are further classified into serous, clear cell and mixed carcinomas based on their histological subtypes, [4,5] with a majority of them belonging to the serous subtype (65-70%). [6] These carcinomas are highly lethal as they are diagnosed at an advanced stage of the disease. [5] The severity of the disease is categorized from Stage I – IV based on the metastatic spread of tumor cells from the ovaries, [7] with tumor cells confined to ovaries in Stage I while they spread to distal organs in Stage IV. The older population (40-65 years) is more susceptible to these carcinomas. [7]

Poor prognosis is touted to be the primary cause for the high mortality rate associated with OC as zero to no symptoms are observed until the latter stages of the disease. [3,8] The current standard of care for OC treatment is surgery followed by chemotherapy. [1,8] Surgical removal of the tumor involves two steps, the first step (staging) to estimate the metastatic spread of tumor cells and the second step (debulking) to remove the tumor mass. [5] Chemotherapy often involves delivering large doses of chemotherapeutic drugs into systemic circulation, thereby exposing healthy tissues to these toxic doses, causing severe side effects and dose limiting toxicities. [8,9] Platinum based compounds and taxanes are currently being administered for chemotherapy cycles for OC treatment. [1,9] The major problem with the current treatment option is that 90% of the patients showed relapse of cancer and the tumors were taxane or platinum resistant upon relapse. [8,10] One of the primary reasons for the development of chemo resistance include the inability to deliver therapeutic concentrations of chemotherapeutic drugs to the tumor site. [10] The tumor cells spontaneously upregulate alternate pathways when a particular pathway is targeted using a single chemotherapeutic agent. [11] This is where combination therapies play a key role in preventing the drug resistance to a particular chemotherapeutic agent by acting on multiple mechanisms involved in tumor progression. [9,12] Therefore, the combination needs to be carefully chosen in order to achieve maximum synergistic and beneficial effects against tumor progression.

Tumor protein (TP53) constitutes the major genetic mutation found in majority of the OC tumors (90%) while the lesser known mutations include BRAF, KRAS, PTEN and PIK3CA. [7,13] TP53 is inactivated or mutated in a majority of these EOC's. One of the study revealed that TP53 inhibition can activate the mTOR signaling cascade. [14] Hypoxic conditions were reported significantly in a variety of cancers including ovarian cancer. [15] Newer treatment regimens targeting both the hypoxic conditions and the mTOR pathway therefore may provide the solution for effectively treating OC. Hypoxia (inadequate oxygen levels) or hypoxic conditions upregulate HIF-1α, a transcription factor that plays an important role in cellular response to systemic oxygen levels. HIF-1α undergoes conformational changes upon response to hypoxic conditions thereby inducing the transcription of a variety of genes involved in cell proliferation, survival, growth and angiogenesis. [16,17] Therefore targeting this pathway would be highly beneficial in controlling the tumor growth and reducing its metastatic spread. Chetomin is a metabolite of a fungal species chaetomium and it prevents the interaction of HIF-1α with the transcriptional co-activator p300, thereby preventing the transcription of downstream signaling moieties. [18,19] CHE is a member of the epidithiodiketopiperazine (ETP) family and its mechanism of action is proposed as ejecting the zinc ion from the CH1 domain of p300 thereby preventing its interaction with the HIF-1α. [20] Recent studies have reported the use of Everolimus in the treatment of OC. [21,22] It binds to the protein receptor FKBP12 that interacts with the mammalian target of rapamycin (mTORC1) sub-unit and inhibits downstream signaling. The mTOR pathway is upregulated in a variety of cancers including ovarian cancer. [21] mTOR integrates the input from upstream amino acids, growth factors, and acts as a downstream effector in inducing cell proliferation, protein synthesis and transcription of various genes. [23] Thus, targeting the mTOR pathway can have inhibiting effects on tumor spread. Previous studies have reported the upregulation of HIF- 1α when mTOR pathway was inhibited. [24,25] Therefore the combination of these two drugs inhibits both the major pathways involved in OC and also helps prevent the development of drug resistance. Hence a versatile nanocarrier that can load and deliver both drugs simultaneously at therapeutically relevant concentrations can be beneficial in treating OC.

The use of polyester (PEG-*b*-PLA) based diblock copolymer nano-platforms for cancer therapy has received tremendous response in the past decade due to their abilities to a) reduce unwanted systemic toxicities, b) improve the solubility and pharmacokinetic profiles of encapsulated drugs, c) prolong the circulation times by reducing their renal clearance and d) decrease the drug exposure to proteins/albumins and blood components.[26,27] The diblock copolymers self-assemble into micellar structures in aqueous media above the critical micelle concentration, with a narrow size ranging from 10-100 nm, and exhibit a core-shell like structure with a hydrophilic corona and a hydrophobic core. [28] The core solubilizes the hydrophobic drug molecules, thus increasing their aqueous solubility while the hydrophilic corona shields the core from any interactions with opsonins or blood components. [29] CHE and EVR are poorly soluble in water with aqueous solubilities of < 40 µg/mL for CHE (Percepta, ACD Labs) and 9.6 µg/mL for EVR. [30] Thus, incorporation of CHE and EVR in the DDM can significantly enhance their aqueous solubilities to therapeutically relevant concentrations by solubilizing these drugs in the hydrophobic PLA core, thereby allowing us to evaluate their chemotherapeutic potential. These diblock copolymers are biocompatible and biodegradable as they undergo hydrolysis in biological systems to non-toxic monomers. [31] These micelles can be passively targeted to the tumor site via the Enhanced Permeation and retention effect (EPR) courtesy of their nano size range and long circulation times. [33, 34] Numerous studies have already reported the use of these diblock copolymer micelles for the co-delivery of multiple chemotherapeutic drugs. [28, 32] The objective of this work is to develop a micellar nano platform for co-delivering CHE and EVR and evaluate its safety and efficacy *in vitro* and *in vivo* in ovarian cancer models. We hypothesize that CHE and EVR loaded PEG-*b*-PLA micelles when injected i.v. act synergistically in reducing the tumor volume by targeting the major pathways involved in OC and also prevent the development of drug resistance in relevant ovarian xenograft tumors.

4.3 MATERIALS AND METHODS

4.3.1 Materials, cell lines, and animals

CHE was purchased from Sigma Aldrich (St Louis, MO), and EVR was purchased from LC Laboratories (Woburn, MA). The diblock copolymers methoxy poly(ethylene glycol)$_{2000}$-*block*-poly(lactic acid)$_{1800}$ (mPEG$_{2000}$-*b*-PLA$_{1800}$)[M_n = 3800; PDI = 1.1] and methoxy poly(ethylene glycol)$_{4000}$-*block*-poly(lactic acid)$_{2200}$ (mPEG$_{4000}$-*b*-PLA$_{2200}$)[M_n = 6160; PDI = 1.12] were purchased from Advanced Polymer Materials Inc. (Montreal, CAN). The three ovarian cancer cell lines ES2 (ATCC® CRL-1978™), TOV21G (ATCC® CRL-11730™), and OVCAR-3 (ATCC® HTB-161™) were purchased from Ame2.rican Type Culture Collection (ATCC) (Manassas, VA). Roswell Park Memorial Institute (RPMI) media, Fetal Bovine Serum (FBS), Trypsin, and the antibiotics were obtained from Corning CellGro (Manassas, VA). Slide-A-Lyzer™ 20 k MWCO dialysis cassettes were acquired from Thermo Scientific (Rockford, IL). The cell viability assay Cell Titer Blue® was purchased from Promega (Madison, WI). Histology supplies were obtained from Electron Microscopy Sciences (Hatfield, PA). Rabbit monoclonal antibodies Phospho-4EBP1 (236B4), Cleaved Caspase-3 (D175) and Carbonic anhydrase IX (D10C10) were obtained from Cell Signaling Technology (Beverly, MA) while the CD31 rabbit polyclonal antibody (ab28364) was purchased from Abcam (Cambridge, MA). Cy3-AffiniPure Donkey Anti-Rabbit IgG (H+L) antibody was purchased form Jackson Immune Research (West Grove, PA). Female athymic nude mice were obtained from Frederick National Laboratory for Cancer Research (Frederick, MD). All other reagents and supplies were purchased from VWR (Radnor, PA) or Fisher Scientific (Fairlawn, NJ).

4.3.2 Preparation and Characterization of individual and DDM

Solvent evaporation method was used for the preparation of individual CHE-M (Chetomin micelles), EVR-M (Everolimus micelles) and the dual drug loaded micelles (DDM). [29, 36, 37] The micelles were prepared with CHE: EVR at a molar ratio of 1:50. The two di-block copolymers mPEG$_{2000}$-*b*-PLA$_{1800}$ or mPEG$_{4000}$-*b*-PLA$_{2200}$ have been used to formulate micelles in this study. Briefly, 15 mg of the mPEG-*b*-PLA polymer was solubilized in acetonitrile (ACN) and the stock solutions of CHE and EVR (in ACN) were added to the polymer solution to obtain the required concentrations. The contents were transferred to a 5 mL round bottomed flask (RBF) and the organic solvent was evaporated by using a roto evaporator. The evaporation cycle consisted of 2 segments with the first segment lasting for 5 minutes at 260 mbar pressure and the second segment for 3 minutes at 100 mbar. The RBF was set to rotate at a speed of 100 rpm and the temperature of the water bath was set to 45 ^{0}C. A thin film was achieved upon complete evaporation of the organic solvent. The film was rehydrated with 0.5 mL of deionized water (18.6 MΩ) at 60 ^{0}C and is completely solubilized to form the polymeric micelles. The micelles were then collected into a centrifuge tube and were spun at 5000 rpm for 3 minutes, and filtered through a 0.2 µm sterile nylon filter.

The formulated micelles were characterized for size by Dynamic light scattering (DLS) using a Malvern Nano ZS (Malvern Instruments Inc, U.K.). All measurements were performed in triplicate and data is presented as the mean z-average diameter ± SD (nm) and polydispersity index (PDI ± SD). The drug loading for the individual and DDM was determined by reverse phase high performance liquid chromatography (RP-HPLC) using a Shimadzu HPLC system consisting of LC-20 AT pump and SPD M20 diode array detector. The analysis was performed using a Zorbax C8 Column (4.6 ×75mm, 3.5 µm) in isocratic mode with methanol/water (74/26) containing 0.1% phosphoric acid at a flow rate of 1mL/min and an injection volume of 10 µL with the column temperature at 40 ^{0}C. The CHE and the EVR peaks were monitored at 203 nm and 279 nm with a retention times of 1.4 min and 12.4 min respectively. All measurements were performed in triplicate and the loading data is presented as mean drug loading (mg/mL) ± SD.

4.3.3 *In vitro* drug release from individual and DDM

Slide-A-Lyzer Dialysis cassettes were used to analyze the release pattern of CHE and EVR from the individual and the DDM. Briefly, 3 dialysis cassettes were each loaded either with 3 mL of freshly prepared CHE-M, EVR-M or the DDM. Cassettes with a MWCO of 20,000

Da were chosen to ensure unobstructed diffusion of the free drugs and any unassociated polymer molecules from the cassettes into the buffer. The cassettes were placed in 2.5 L of 10 mM phosphate buffer pH 7.4 at 37 ^{0}C for 72 h and the buffer was replaced every 3 h to evaluate the release profiles under sink conditions by dialysis. [33] γ – Globulins at a concentration corresponding to plasma concentration of 15 mg/mL were added to the release buffer to replicate *in vivo* conditions. [30,39] A sample volume of 20 µL was withdrawn from each cassette at 0, 0.5, 1, 2, 3, 6, 12, 24, 48 and 72 h and was replaced with equal volume of fresh buffer. The collected samples were analyzed for drug content using RP-HPLC after diluting 50 fold with the mobile phase. The data is presented as mean % drug release ± SD. A two phase exponential association equation (GraphPad Prism 5 software) was used to curve fit the data and the time required for 50% drug release (t½) across the slow and fast phases along with the goodness of fit (r^2) values are presented in Table 4.1. Statistical analysis was performed using GraphPad Prism 5 software.

4.3.4 *In vitro* cell viability study and Combination Index analysis in ES2, TOV21G and OVCAR3 cells

The anti-proliferative effects of CHE-M, EVR-M and DDM was evaluated in three sub-types of ovarian carcinomas (TOV21G, ES2 and OVCAR-3). ES2 cells represent the high grade serous subtype, [34] TOV21G cell line represents the clear cell subtype, [35] while the OVCAR3 cell line represents a mixed subtype. [35] TOV21G and OVCAR-3 cells were seeded at 5000 cells/well in 96 well flat bottom plates while ES2 cells were seeded at 2000 cells/well. The cells were allowed to attach for 3 h at 37 ^{0}C and then treated with either CHE-M, EVR-M or the DDM at a CHE:EVR molar ratio of 1:40. The concentration range for CHE-M and the DDM was 0.01-1000 nM while the concentration for the EVR-M was from 500-50000 nM. After 72 h of incubation, cell viability was determined by using the CellTiter Blue® assay. Briefly, 20 µL of the CellTiter Blue reagent was added to each well and was allowed to incubate for 2 h. The fluorescence intensities were measured at $560_{EX}/590_{EM}$ nm using a plate reader. The concentration required to inhibit 50% growth (IC_{50}) was calculated by using GraphPad Prism software (Version 5.0, San Diego, USA) wherein the data was fitted into a nonlinear pattern using a log (inhibitor) vs response –

variable slope equation. The concentrations are reported for the most potent drug (CHE) for the DDM. The combination effect of CHE and EVR in micelles was evaluated by using the CompuSyn software (Version 1.0, ComboSyn Inc., USA). The software is based on the Chou and Talalay median-effect principle, [36] and generates Combination Index (CI) values at various cell fractions (F_a) that are affected. CI values of <1, 1, and >1 indicate synergism, additive effect and antagonism respectively. The F_a vs CI plot provides information about the combination effects at various doses tested. The data is presented as F_a vs CI plot.

4.3.5 *In vivo* acute toxicity study

6-8 weeks old healthy female athymic nude mice were categorized into 5 groups with four animals in each group (n = 20). Each group was injected with either saline (no treatment), vehicle (empty micelles at a polymer concentration of 300 mg/kg), CHE-M at 0.5 mg/kg, EVR-M at 25 mg/kg, or DDM at (0.5 mg/kg CHE + 25 mg/kg EVR) on days 0, 7, and 14. The mice were injected via tail vein with the total volume of injection was no more than 1% of the animal's body weight in volume, approximately 200 µL, with the dose adjusted according to the weight of each mice. The mice were regularly monitored for signs of acute toxicity that included noticeable changes in appearance or behavior, loss in body weight of ≥ 15% or death throughout the study. The body weights of the mice in different groups was monitored for 21 days and the data is presented as mean (%) normalized body weight ± SD. All of the animal work was performed in compliance with NIH guidelines and Institutional Animal Care and Use Committee Policy (IACUC) at Oregon State University for End-Stage Illness and Pre-emptive Euthanasia, based on Humane Endpoints Guidelines.

4.3.6 *In vivo* assessment of efficacy in ES2 ovarian xenograft model

ES2 cells (1×10^6) were injected subcutaneously into the right flank of female athymic nude mice to develop the ovarian cancer xenograft model to be used in this study. The animals were 6-8 weeks old, weighed an average of 20-25 g, provided with free access to food and water, and were maintained at a controlled temperature and humidity in ventilated cages throughout the experiment. Upon reaching a tumor volume of 75 – 100 mm^3, mice were categorized into 5 groups with 3 animals in each group (n=15). The tumor volume was calculated using the formula $\pi/6$ x length x $width^2$. The groups comprised of untreated control group (saline), empty micelle treated group (vehicle), CHE-M treated group, EVR-M treated group and the DDM treated group. Micelles were injected through the tail vein with either a polymer dose of 300 mg/kg, CHE dose of 0.5 mg/kg, EVR dose of 25 mg/kg or a DDM dose of (0.5 mg/kg CHE + 25 mg/kg EVR) once a week for 3 cycles. The injection volume, approximately 200 µL, was adjusted according to the weight of the mouse. The untreated control group was injected with saline. The mice were injected on day 0, 7 and 14 and the tumor volume was measured every 3 days for 21 days, one week post last injection. One-way ANOVA at 5% significance level with Tukey's Multiple Comparison post-test with groups compared at 5% significance level was used for the analysis of tumor data. The weights and the tumor volumes of mice on the last day of the study (21st day) one week post last injection, were measured and the animals were humanely euthanized in the CO_2 chamber. Immediately post-euthanasia, the tumors were collected and were soaked in 4% paraformaldehyde overnight and were embedded in paraffin blocks. 5 µm thick tumor samples were sectioned from the paraffin blocks onto glass slides using the Microtome. The sections were stained using different antibodies for detecting the micro vessel density (CD31 antibody), apoptosis (Cleaved caspase-3 antibody), involvement of the mTOR pathway (P-4EBP1 antibody) and the HIF pathway (Carbonic AnhydraseIX antibody). Antibodies against CD31 were used to label the blood vasculature in the tumor tissues and NIH Image J software was used for quantifying the micro vessel density. Goat anti-rabbit CY3 was used as the secondary antibody (red) with DAPI as the nuclear stain (blue). Zeiss AXIO ImagerZ1 with a digital AxioCam HRm was used to capture the images and they were processed using AxioVision 4.7 (Carl Zeiss Microscopy, LLC) and Adobe Photoshop CS5 software. All the pictures were taken at 20X magnification. The counting tool in Adobe Photoshop was used to count the CA9 positive cells, the cleaved caspase positive cells, and the P-4EBP1 positive cells in the analyzed tumor sections with at least 5 random fields (0.55 mm^2) per tumor being counted for each tumor sample. A minimum of 5 random fields ($0.55mm^3$)/tumor were quantified to measure the micro vessel density.

All of the animal work was performed in compliance with NIH guidelines and Institutional Animal Care and Use Committee Policy (IACUC) at Oregon State University for End-Stage Illness and Pre-emptive Euthanasia, based on Humane Endpoints Guidelines. Significance for immunohistochemistry data was determined using one-way ANOVA at 5% significance level with Tukey's Multiple Comparison post-test with groups compared to each other at 5% significance level. All statistical analyses are performed using GraphPad Prism software version 5.04 for Windows, GraphPad Software, San Diego, California USA.

4.4 RESULTS AND DISCUSSIONS

4.4.1 Preparation and characterization of individual and DDM

The structures of CHE, EVR and a depiction of the DDM is presented in (Figure 4.1). CHE-M formulated using the $mPEG_{4000}$-*b*-PLA_{2200} were able to solubilize up to 0.42 mg/mL of CHE while the EVR-M formulated using $mPEG_{2000}$-*b*-PLA_{1800} increased the solubility of EVR to 2.25 mg/mL. The DDM prepared from the $mPEG_{2000}$-*b*-PLA_{1800} copolymer were able to co-solubilize 0.41 mg/mL of CHE and 2.21 mg/mL of EVR respectively. These micelles were not stable post 6 h at room temperature as indicated by drug precipitation and a loss of > 10 % of initial drug loading. CHE-M formulated using $mPEG_{2000}$-*b*-PLA_{1800} copolymer were stable for more than 48 h, and exhibited similar CHE loading efficiencies as the $mPEG_{4000}$-*b*-PLA_{2200} CHE-M (Figure 4.2). The polymer drug compatibility might be the primary reason for such behavior. Meanwhile, EVR-M and the DDM prepared using the $mPEG_{4000}$-*b*-PLA_{2200} copolymer demonstrated excellent stability for more than 48 h at room temperature and their loading efficiencies are depicted in (Figure 4.2). It has been well documented in the literature that block copolymers with higher molecular weight allow for higher drug loading efficiencies and form more stable micelles. [31] The higher stability of these micelles can be attributed to the core compatibility of the encapsulated drugs along with interactions between encapsulated drugs among themselves and this phenomenon has been previously reported. [28,32,37] Therefore mPEG$_{2000}$-*b*-PLA$_{1800}$ was used to formulate CHE-M while mPEG$_{4000}$-*b*-PLA$_{2200}$ copolymer was used for formulating the EVR-M and the DDM hereafter. CHE and EVR are poorly soluble in water with aqueous solubilities of < 40 µg/mL for CHE (Percepta, ACD Labs) and 9.6 µg/mL for EVR. [30] EVR-M and DDM increased the aqueous solubility of EVR by 240 fold while the CHE-M and DDM increased the solubility of CHE by 13.0 fold thereby allowing us to access their efficacies at clinically relevant concentrations. Our observed phenomenon of increased aqueous solubility and stability of hydrophobic drugs when incorporated in mPEG-*b*-PLA micelles is in accordance with published literature. [28,29] The size of the CHE-M was 21.14 ± 0.37 with a PDI of 0.13 ± 0.0041. The EVR-M and the DDM had a size of 34.36 ± 0.38 and 39.66 ± 0.83 with a PDI of 0.14 ± 0.0036 and 0.13 ± 0.0021 respectively. The slight increase in micelle size for the EVR-M and the DDM can be attributed to the higher molecular weight of the mPEG$_{4000}$-b-PLA$_{2200}$ di-block copolymer used, the copolymer block length and the PEG/PLA composition when compared with the copolymer used for formulating CHE-M. The ratio of the PEG: PLA block and the length of the PLA block were considered as significant factors that could control the size of the micelles formed. [31] A micelle size ranging from 10 – 100 nm was commonly reported when mPEG-*b*-PLA di-block copolymers were used in multiple studies. [32, 37, 38] Our formulated micelles were in the same range supporting the existing literature.

4.4.2 *In vitro* drug release from individual and DDM

The drug release profiles of CHE and EVR from the individual and the DDM in the presence of γ - globulins is shown in (Figure 4.3). Micelles come in contact with serum components, albumins and globulins once they enter the blood stream after *in vivo* injections. [44] The interaction between micelles and blood components/proteins plays a major role in their biodistribution pattern. [39] Globulins interact with the micelles, increasing their size and trigger opsonization and phagocytosis by macrophages leading to their disintegration before reaching the target sites. [29] Therefore to replicate these conditions *in vitro*, γ – globulins were added into the release buffer at concentrations similar to plasma concentrations. The release profiles thus obtained *in vitro* can be somewhat correlated with the micelle's *in vivo* release although factors such as dilution of the micelles, presence and interaction of other blood components like albumins, amongst others need to be taken into consideration. [40] CHE displayed a similar release pattern from both the individual and the DDM with approximately 77% of the drug being released at 72 h. The core component (PLA) that solubilizes CHE in both the individual and the DDM was comparatively similar which resulted in the micelles exhibiting a similar release pattern in spite of using different block copolymers for their formulation. 70% of EVR was released from both the individual and the DDM with similar release patterns at 72 h, indicating that the release profile and the amount of drug released were similar for both CHE and EVR from the individual and the DDM. The release profiles were curve fitted using a two phase exponential association equation and the fast and the slow half-lives (t½) along with the goodness of fit (r^2) values were calculated and presented in (Table 4.1). The individual and the DDM released CHE and EVR in a biphasic pattern with an initial burst release phase that was followed by a sustained release pattern. The initial burst release can be attributed to the diffusion of the surface adsorbed drug into the buffer while the sustained release effect maybe driven by the dissociation of the drug from the biodegradable PLA core. The following sustained release pattern was also dependent on the strength of interactions between the encapsulated drug and the PLA core with stronger drug-core interactions causing slower release patterns. [41] EVR had a stronger interaction with the PLA core compared to CHE as evident from its slower release pattern in both the individual and the DDM. Also, higher drug loading in the case of EVR-M can lead to crystallization of the drug in the core of the micelles leading to slower drug release when compared with a lower drug loading (molecular dispersion) in CHE-M that readily diffuses into the outer aqueous environment. [42] The release pattern of CHE and EVR from the individual and the DDM is therefore primarily diffusion driven with dissociation of the core also playing a minor role and this is in accordance with published literature. [31, 43]

4.4.3 *In vitro* cell viability study and Combination Index analysis in ES2, TOV21G and OVCAR3 cells

The IC_{50} values of CHE-M, EVR-M and the DDM in the three different cell lines are represented in (Figure 4.4). CHE exhibited higher potency among the two drugs in the three cell lines as depicted in Figure 4.4(a) and 4.4(b). A molar ratio of 1:1 of CHE:EVR in the DDM would thus only exhibit the anti-proliferative effects of just Chetomin as higher doses of EVR was required to show efficacy in the DDM. Therefore, to achieve significant anti-proliferative effects of the less potent EVR drug and thereby represent a combination effect, we decided to treat the cells at a molar ratios of 1:40 of CHE: EVR. The individual micelles of CHE and EVR showed similar efficacy in all the three cell lines as seen in (Figure 4.4(a) and 4.4(b)) while the DDM was highly potent in ES2 cells, followed by OVCAR3 cells and finally in TOV21G cells as depicted in (Figure 4.4(c)). It is noteworthy that the ES2 subtype (high grade serous subtype) represents majority of the ovarian carcinomas and therefore our DDM could be effectively used in treating a majority of the patients displaying this phenotype. The effects of two drug interactions (synergistic, additive, or antagonistic) in the three different cell lines was evaluated using the CompuSyn software and the data is depicted in (Figure 4.4(d)). The dual drug combination (CHE+EVR) was strongly synergistic at all the concentrations tested for both the ES2 and the TOV21G cell lines but the synergism was stronger in the ES2 cell line comparatively as seen in (Figure 4.4(d)). The drug interactions were synergistic at lower concentrations in the OVCAR3 cell line but slowly turned additive and eventually antagonistic at higher concentrations. This pattern of synergistic behavior in one cell line and antagonistic behavior in another cell line is in accordance with the existing literature with a different drug combination tested. [44] The antagonistic effects of this drug combination in the OVCAR3 cells may be attributed to upregulation of a positive feedback loop when the HIF and the mTOR pathways were targeted. Further studies are required to elucidate the exact mechanisms involved. Our data suggest that the combination micelles have high anti-proliferative effects and both CHE and EVR act synergistically in the ES2 and the TOV21G cell lines at all the concentrations tested. We have successfully demonstrated for the first time that the CHE and EVR in combination act synergistically *in vitro* in the ES2 and the TOV21G ovarian carcinoma subtypes as this combination has not been previously reported. DDM was more potent against ES2 cells than TOV21G cells as depicted in (Figure 4.4(c)). In addition the high grade serous carcinomas represent about 65-70% of epithelial ovarian cancers, [6] and therefore hereafter, we have decided to use the ES2 cells (High grade serous subtype) to develop a xenograft model to test the safety and efficacy of these individual and DDM in relevant animal models.

4.4.4 *In vivo* acute toxicity study

Dose limiting toxicity (DLT) studies were performed to evaluate the maximum tolerated doses (MTD) of CHE-M, EVR-M and the DDM in female athymic nude mice. Mice (n=4) injected with CHE-M at 2 mg/kg could not survive past Day 1, and therefore a new group (n=4) of mice were injected with 1 mg/kg of CHE-M once a week for 3 weeks i.v. The mice showed no changes in behavior, did not lose weight > 15% indicating that they were healthy and the dose was well tolerated. We then tried to determine the DLT of EVR-M by injecting mice (n=4) with doses up to 35 mg/kg once a week for 3 weeks. Unfortunately, the dose was well tolerated and we could not determine the DLT. However, our lab has previously demonstrated a MTD of 50 mg/kg for EVR-M when formulated in PEG_{4000}-*b*-PLA_{2200} micelles.[32] We therefore decided to go with a CHE dose of 1 mg/kg and EVR dose at 50 mg/kg so that we could maintain the 1:4 molar ratio of CHE:EVR. In order to keep the injection volume of the micelle to less than 1% of the mouse's body weight in volume, we had to load high amounts of EVR into the micelles to achieve 50 mg/kg which resulted in forming unstable micelles. Therefore we had to scale down the CHE dose to 0.5 mg/kg and EVR dose to 25 mg/kg so that we could form stable DDM while maintaining the 1:4 molar ratio of CHE:EVR and also stay below an injection volume of 1% of the mouse body weight. The changes in weight of mice treated with saline, vehicle, the individual and the DDM is shown in (Figure 4.5). None of the mice in the different treatment groups lost more than 15% of their body weight nor did they show any abnormal behavior including death, indicating that the doses were well tolerated. The DDM also showed no toxicity demonstrating its ability to safely deliver multiple drugs at higher doses simultaneously.

4.4.5 *In vivo* assessment of efficacy in ES2 ovarian cancer xenograft model

The dose range for CHE-M, EVR-M and the DDM have been determined as described above. The tumor volumes of mice in the different groups is represented in (Figure 4.6(a)). There was no significant difference observed between the tumor volumes of vehicle treated and saline groups upon statistical analysis indicating that the vehicle by itself has no effect on tumor reduction. The CHE-M treated group showed a significant reduction in tumor volume when compared to the saline group. This is in accordance with the published literature as CHE micelles have been previously shown to reduce tumor burden and inhibit tumor angiogenesis in transgenic zebrafish and mouse xenograft models. [45] This reduction in tumor volume may be attributed to inhibiting the CAIX enzyme thereby suppressing the HIF pathway. [46] The tumor however continued to grow back after the third injection (last dose) on day 14 indicating a possibility of developing drug resistance by upregulating alternate pathways. [47] EVR-M treated group had a similar trend where the tumor reduction was significant when compared with the saline group, but the tumor kept growing after the last injection rendering the treatment ineffective in preventing the relapse of the cancer. It has been previously reported that EVR exerts anti-proliferative and anti-angiogenic effects by inhibiting the mTOR pathway. [35] However, the DDM treated group showed a statistically significant reduction in tumor volume when compared with the saline group, the CHE-M, and the EVR-M, with the DDM treated group showing the highest reduction in tumor volume. More importantly, it prevented the growth of the tumor after the treatment ended on day 14 implying that it has the scope to prevent tumor regression.

The results from immunohistochemical analysis for measuring micro vessel density and quantifying apoptotic cells is depicted in (Figure 4.6(b)) and (Figure 4.6(c)) respectively. A reduction in the blood vasculature implied lower micro vessel density (MVD) and significant inhibition of angiogenesis in that treatment group. The vehicle treated group had the same MVD as the saline group indicating that the empty micelles had no effect on angiogenesis. The CHE-M and the EVR-M reduced the MVD significantly when compared to the saline group whereas, it is the DDM treated group that had the highest reduction in MVD when compared to the saline group. The DDM group even has a significant MVD reduction when compared to the individual micelle groups indicating that CHE and EVR are acting synergistically in inhibiting angiogenesis in the tumor tissue. Anti-angiogenic effects of CHE and EVR individually have been documented elsewhere, [35,49] but we for the first time have shown a synergistic anti-angiogenic effect of their combination in ovarian xenograft models.

The apoptotic cells were quantified by using antibodies against Cleaved caspase- 3. Caspase-3 plays a major role in executing apoptosis and is often considered as an effector caspase that is responsible for the initiation of the cell death cascade. [48] Therefore the cleaved caspase levels can be used as an indicator of apoptosis. The highest volume of apoptotic cells were found in the DDM treatment when compared with the saline and the individual treatment groups indicating that this treatment regimen acts synergistically and therefore achieves higher apoptotic cell death when compared to the individual treatments.

The results for the determination of pathways involved are represented in (Figure 4.7). Carbonic anhydrase (CAIX) enzyme is upregulated in hypoxic conditions in a variety of tumors and plays a major role in tumor progression, invasiveness and impaired response to chemotherapy. [50] CAIX enzymes are primarily responsible for maintaining an alkaline intracellular pH (pHi) favorable for tumor cell survival and also contribute to creating an acidic extracellular environment for tumor cells to turn into more aggressive phenotypes. [46] Inhibition or knockdown of these enzymes using small molecules or siRNA has shown to reduce tumor proliferation and growth, and also improved the response to chemotherapeutic strategies. [49] Therefore low number of CAIX positive cells indicated significant reduction in hypoxic conditions by inhibiting the HIF pathway. A highly significant reduction in the CA9 positive cells in the CHE-M treated group was observed when compared to the saline group as depicted in (Figure 4.7(a)) indicating that HIF-1 pathway is being primarily targeted and inhibited to certain effect. No significant difference was observed between the saline and the vehicle treated groups as expected. The EVR-M treated group and the DDM treated group also had significantly fewer number of CAIX positive cells indicating the inhibition of hypoxic conditions and thereby targeting the HIF pathway. It has been previously reported that EVR also targets the HIF pathway along with the mTOR pathway. [50] The elf4E-binding proteins (4E-BP1) belong to a class of repressor proteins that bind to the translation initiation factor (elf4F) complex and inhibits translation based on its phosphorylated state. [51] Hypo phosphorylated 4EBP1 binds strongly to the elf4F complex in normal cells. The mTOR pathway (external stimuli) signals directly to 4EBP1 and hyper phosphorylates it preventing its binding to the elf4F complex and thereby triggering uncontrolled translation. [52] Reduction in the phosphorylated (P-4EBP1) cells therefore implies reduction or inhibition of the mTOR pathway. The saline and the vehicle groups displayed no significant difference in the number of P-4EBP1 cells as depicted in (Figure 4.7(b)) while the EVR-M treated group displayed a significant reduction in the number of P-4EBP1 cells when compared to the saline group indicating that the mTOR pathway was prominently targeted and inhibited. The CHE-M treated group also had significant difference from saline group but the difference was more prominent in the EVR-M treated group when compared with the CHE-M or the DDM treated groups. We could therefore confirm that the two major pathways HIF and the mTOR were targeted causing apoptotic induction and angiogenesis inhibition thereby helping in reducing the tumor volume in ovarian xenograft tumor models.

4.5 CONCLUSION

In conclusion, we have developed a mPEG-*b*-PLA based micellar platform that could co-deliver multiple therapeutic drugs (CHE and EVR) and exhibit synergistic effects *in vitro* and *in vivo* in ovarian cancer models. The DDM exhibited the highest efficacy in reducing the tumor volume and preventing proliferation in the *in vivo* model and the *in vitro* cell culture studies than the individual drug loaded micelles. We were able to prove that our formulation targeted the two major pathways (HIF and mTOR) involved in the progression of OC. We also confirmed that DDM exhibited a synergistic effect by inducing apoptosis and inhibiting angiogenesis in the tumor models. No signs of toxicity were observed *in vitro* or *in vivo* indicating the safety profile of these polymeric micelles and their potential application as delivery vehicles in future treatment strategies.

4.6 ACKNOWLEDEGEMENT

This study was supported by the grant from AACP New Pharmacy Faculty Research Award Program, Medical Research Foundation of Oregon New Investigator Grant and Oregon State University-Startup fund.

4.7 REFERENCES

[1] S. Banerjee and S. B. Kaye, *Clin Cancer Res*, 2013, **19**, 961-968.

[2] C. Della Pepa, G. Tonini, D. Santini, S. Losito, C. Pisano, M. Di Napoli, S. C. Cecere, P. Gargiulo and S. Pignata, *Cancer Treat Rev*, 2015, **41**, 136-143.

[3] R. McCorkle, J. Pasacreta and S. T. Tang, *Holist Nurs Pract*, 2003, **17**, 300-308.

[4] T. Kaku, S. Ogawa, Y. Kawano, Y. Ohishi, H. Kobayashi, T. Hirakawa and H. Nakano, *Med Electron Microsc*, 2003, **36**, 9-17.

[5] W. G. McCluggage, *J Clin Pathol*, 2008, **61**, 152-163.

[6] J. D. Seidman, I. Horkayne-Szakaly, M. Haiba, C. R. Boice, R. J. Kurman and B. M. Ronnett, *Int J Gynecol Pathol*, 2004, **23**, 41-44.

[7] W. G. McCluggage, *Pathology*, 2011, **43**, 420-432.

[8] T. S. Kristedja, R. J. Morgan and M. Cristea, *Womens Health (Lond Engl)*, 2010, **6**, 679-694.

[9] L. Cai, G. Xu, C. Shi, D. Guo, X. Wang and J. Luo, *Biomaterials*, 2015, **37**, 456-468.

[10] E. C. McClung and R. M. Wenham, *Int J Womens Health*, 2016, **8**, 59-75.

[11] G. Deppe and P. Baumann, *Curr Opin Oncol*, 2000, **12**, 481-491.

[12] D. Wang, M. Wang, N. Jiang, Y. Zhang, X. Bian, X. Wang, T. M. Roberts, J. J. Zhao, P. Liu and H. Cheng, *Oncotarget*, 2016, DOI: 10.18632/oncotarget.7549.

[13] J. Madore, F. Ren, A. Filali-Mouhim, L. Sanchez, M. Kobel, P. N. Tonin, D. Huntsman, D. M. Provencher and A. M. Mes-Masson, *J Pathol*, 2010, **220**, 392-400.

[14] L. Galluzzi, O. Kepp and G. Kroemer, *Aging (Albany NY)*, 2010, **2**, 535-537.

[15] H. Jiang and Y. Feng, *Int J Gynecol Cancer*, 2006, **16 Suppl 1**, 405-412.

[16] G. Powis and L. Kirkpatrick, *Mol Cancer Ther*, 2004, **3**, 647-654.

[17] A. Staab, J. Loeffler, H. M. Said, D. Diehlmann, A. Katzer, M. Beyer, M. Fleischer, F. Schwab, K. Baier, H. Einsele, M. Flentje and D. Vordermark, *BMC Cancer*, 2007, **7**, 213.

[18] J. Kessler, A. Hahnel, H. Wichmann, S. Rot, M. Kappler, M. Bache and D. Vordermark, *BMC Cancer*, 2010, **10**, 605.

[19] A. Horiuchi, T. Hayashi, N. Kikuchi, A. Hayashi, C. Fuseya, T. Shiozawa and I. Konishi, *Int J Cancer*, 2012, **131**, 1755-1767.

[20] A. L. Kung, S. D. Zabludoff, D. S. France, S. J. Freedman, E. A. Tanner, A. Vieira, S. Cornell-Kennon, J. Lee, B. Wang, J. Wang, K. Memmert, H. U. Naegeli, F. Petersen, M. J. Eck, K. W. Bair, A. W. Wood and D. M. Livingston, *Cancer Cell*, 2004, **6**, 33-43.

[21] A. R. van der Bilt, A. G. Terwisscha van Scheltinga, H. Timmer-Bosscha, C. P. Schroder, L. Pot, J. G. Kosterink, A. G. van der Zee, M. N. Lub-de Hooge, S. de Jong, E. G. de Vries and A. K. Reyners, *Clin Cancer Res*, 2012, **18**, 6306-6314.

[22] N. Husseinzadeh and H. D. Husseinzadeh, *Gynecol Oncol*, 2014, **133**, 375-381.

[23] S. Vemulapalli, A. Mita, Y. Alvarado, K. Sankhala and M. Mita, *Target Oncol*, 2011, **6**, 29-39.

[24] P. K. Majumder, P. G. Febbo, R. Bikoff, R. Berger, Q. Xue, L. M. McMahon, J. Manola, J. Brugarolas, T. J. McDonnell, T. R. Golub, M. Loda, H. A. Lane and W. R. Sellers, *Nat Med*, 2004, **10**, 594-601.

[25] R. T. Abraham, *Curr Top Microbiol Immunol*, 2004, **279**, 299-319.

[26] S. R. Croy and G. S. Kwon, *Curr Pharm Des*, 2006, **12**, 4669-4684.

[27] S. Biswas, P. Kumari, P. M. Lakhani and B. Ghosh, *Eur J Pharm Sci*, 2016, **83**, 184-202.

[28] H. C. Shin, A. W. Alani, D. A. Rao, N. C. Rockich and G. S. Kwon, *J Control Release*, 2009, **140**, 294-300.

[29] J. Lu, S. C. Owen and M. S. Shoichet, *Macromolecules*, 2011, **44**, 6002-6008.

[30] Y. Iwase and Y. Maitani, *Biol Pharm Bull*, 2012, **35**, 975-979.

[31] M. Alibolandi, F. Sadeghi, S. H. Sazmand, S. M. Shahrokhi, M. Seifi and F. Hadizadeh, *Int J Pharm Investig*, 2015, **5**, 134-141.

[32] G. P. Mishra, B. S. Doddapaneni, D. Nguyen and A. W. Alani, *Pharm Res*, 2014, **31**, 660-669.

[33] J. Shen and D. J. Burgess, *Drug Deliv Transl Res*, 2013, **3**, 409-415.

[34] A. L. Kwok, O. G. Wong, E. S. Wong, O. K. Tsun, K. K. Chan and A. N. Cheung, *J Clin Pathol*, 2014, **67**, 921-922.

[35] S. Domcke, R. Sinha, D. A. Levine, C. Sander and N. Schultz, *Nat Commun*, 2013, **4**, 2126.

[36] T. C. Chou and P. Talalay, *Adv Enzyme Regul*, 1984, **22**, 27-55.

[37] H. C. Shin, A. W. Alani, H. Cho, Y. Bae, J. M. Kolesar and G. S. Kwon, *Mol Pharm*, 2011, **8**, 1257-1265.

[38] K. Letchford and H. Burt, *Eur J Pharm Biopharm*, 2007, **65**, 259-269.

[39] H. Chen, S. Kim, W. He, H. Wang, P. S. Low, K. Park and J. X. Cheng, *Langmuir*, 2008, **24**, 5213-5217.

[40] S. M. Krishnan and N. M. Dixit, *PLoS Comput Biol*, 2011, **7**, e1001072.

[41] L. Zhao, C. Yang, J. Dou, Y. Xi, H. Lou and G. Zhai, *J Biomed Nanotechnol*, 2015, **11**, 436-446.

[42] Y. Li, X. R. Qi, Y. Maitani and T. Nagai, *Nanotechnology*, 2009, **20**, 055106.

[43] L. Yang, A. El Ghzaoui and S. Li, *Int J Pharm*, 2010, **400**, 96-103.

[44] B. Cote, L. J. Carlson, D. A. Rao and A. W. Alani, *J Control Release*, 2015, **213**, 128-133.

[45] Q. Wu, G. Li, S. Deng, L. Ouyang, L. Li, L. Liu, N. Luo, X. Song, G. He, C. Gong and Y. Wei, *Nanoscale*, 2014, **6**, 11940-11952.

[46] P. C. McDonald, J. Y. Winum, C. T. Supuran and S. Dedhar, *Oncotarget*, 2012, **3**, 84-97.

[47] S. T. Pan, Z. L. Li, Z. X. He, J. X. Qiu and S. F. Zhou, *Clin Exp Pharmacol Physiol*, 2016, DOI: 10.1111/1440-1681.12581.

[48] X. Gao, B. Wang, X. Wei, K. Men, F. Zheng, Y. Zhou, Y. Zheng, M. Gou, M. Huang, G. Guo, N. Huang, Z. Qian and Y. Wei, *Nanoscale*, 2012, **4**, 7021-7030.

[49] B. P. Mahon, M. A. Pinard and R. McKenna, *Molecules*, 2015, **20**, 2323-2348.

[50] S. Faivre, G. Kroemer and E. Raymond, *Nat Rev Drug Discov*, 2006, **5**, 671-688.

[51] A. C. Gingras, S. P. Gygi, B. Raught, R. D. Polakiewicz, R. T. Abraham, M. F. Hoekstra, R. Aebersold and N. Sonenberg, *Genes Dev*, 1999, **13**, 1422-1437.

[52] G. J. Brunn, C. C. Hudson, A. Sekulic, J. M. Williams, H. Hosoi, P. J. Houghton, J. C. Lawrence, Jr. and R. T. Abraham, *Science*, 1997, **277**, 99-101.

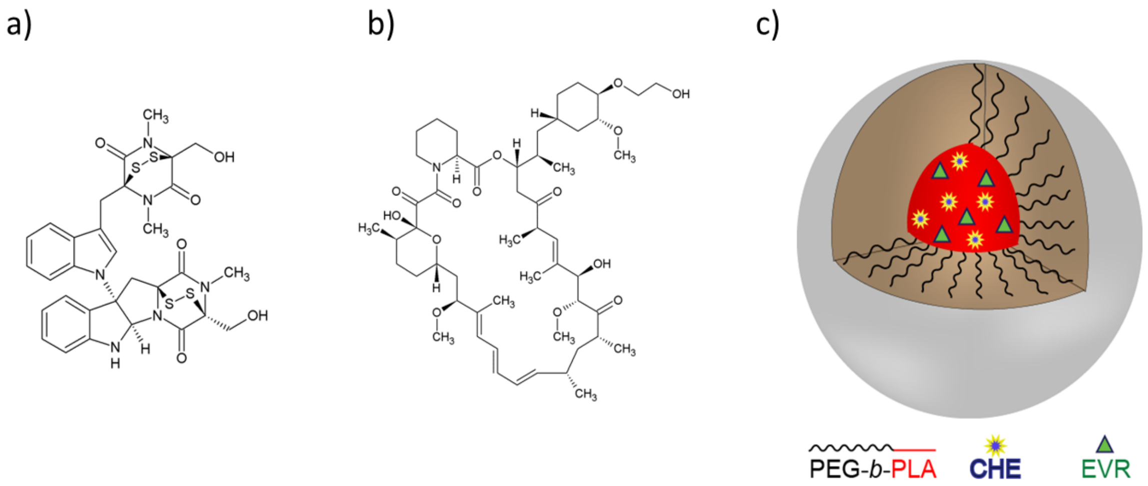

Figure 4.1: Structures of CHE, EVR and schematic representation of the micelle. **(a)** Structures of CHE, **(b)** EVR **(c)** and schematic representation of the DDM.

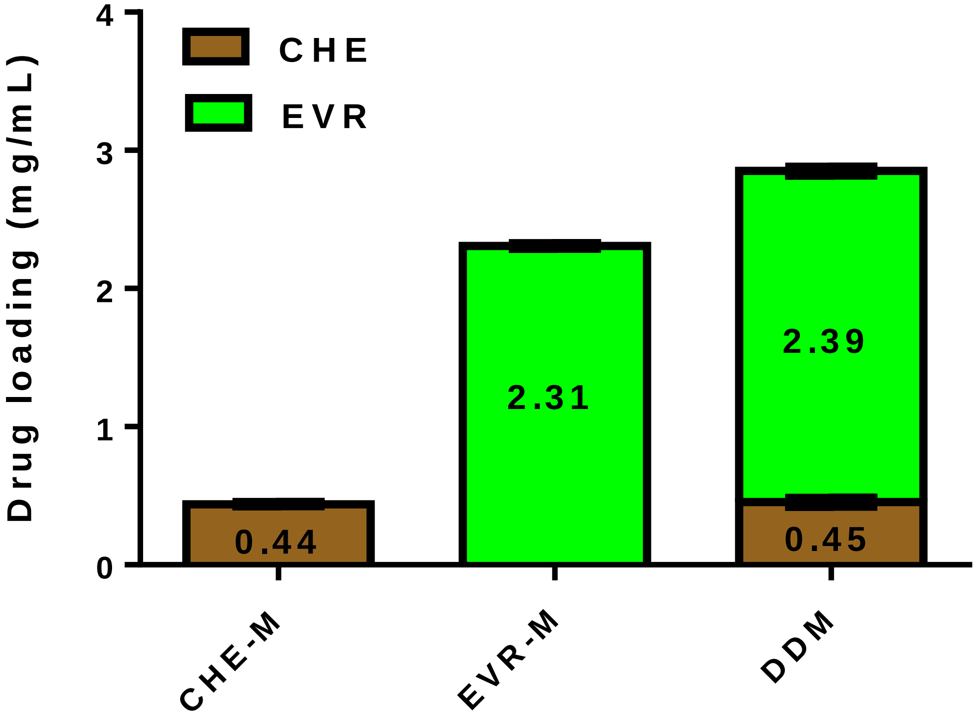

Figure 4.2: Loading efficiency of the micelles.

Drug loading of CHE, and EVR in CHE-M, EVR-M and the DDM prepared using mPEG-b-PLA block copolymers (Mean ± SD, n = 3)

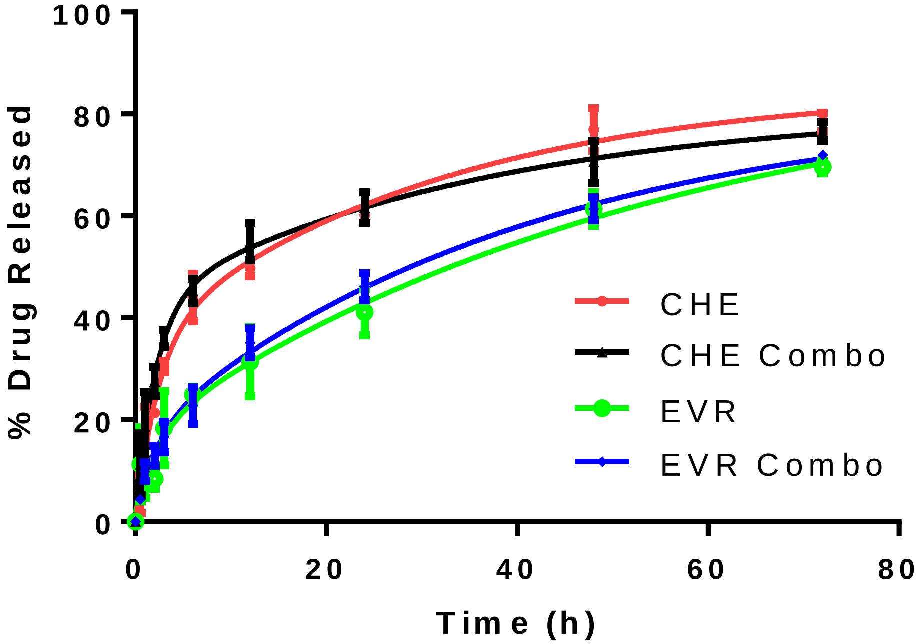

Figure 4.3: Drug release profiles of CHE and EVR.

In vitro drug release profiles of CHE and EVR from the individual and DDM over 72 h. (Mean % drug release ± SD, n = 3).

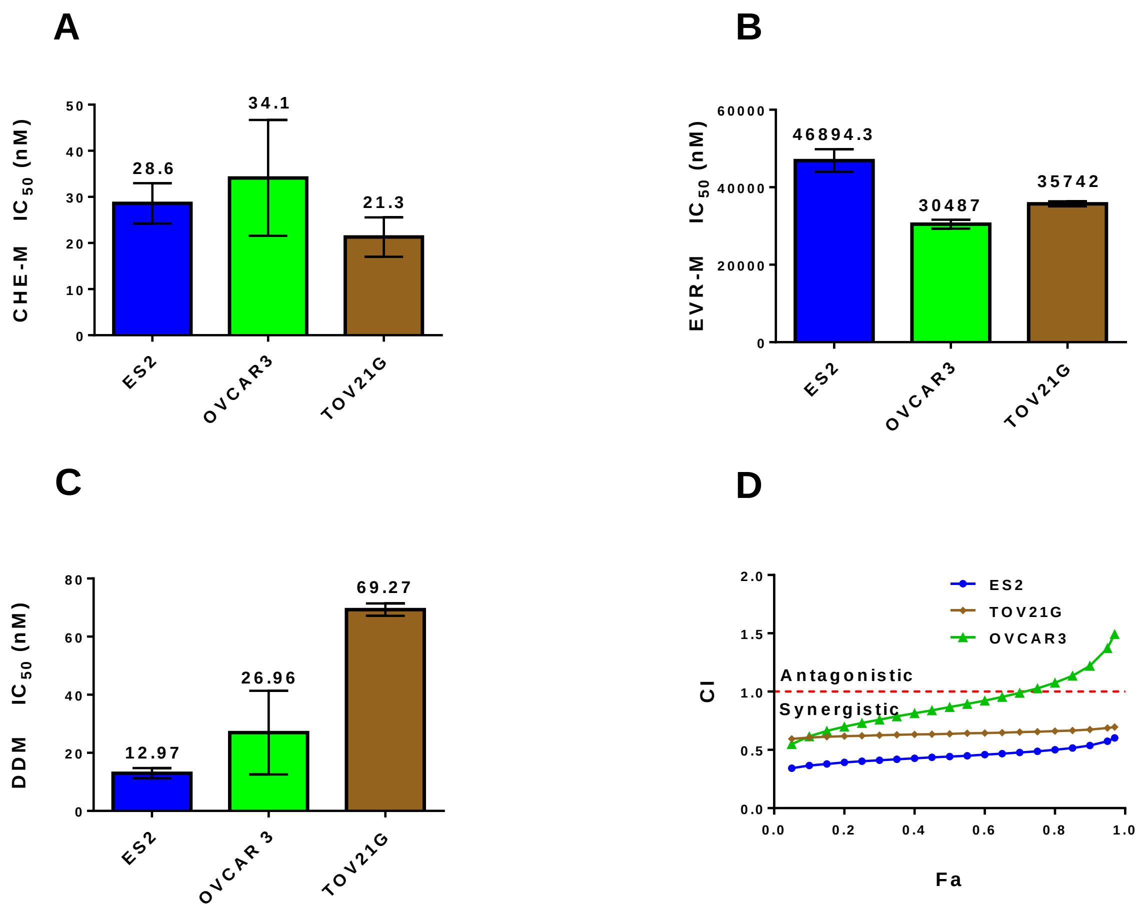

Figure 4.4: IC$_{50}$ data and combination index analysis.

(a) IC$_{50}$ values of CHE-M, **(b)** EVR-M **(c)** and the DDM **(d)** in ES2, OVCAR3 and TOV21G cell lines, Fa vs CI plot for the three cell lines (Mean IC$_{50}$ ± SD, n = 4).

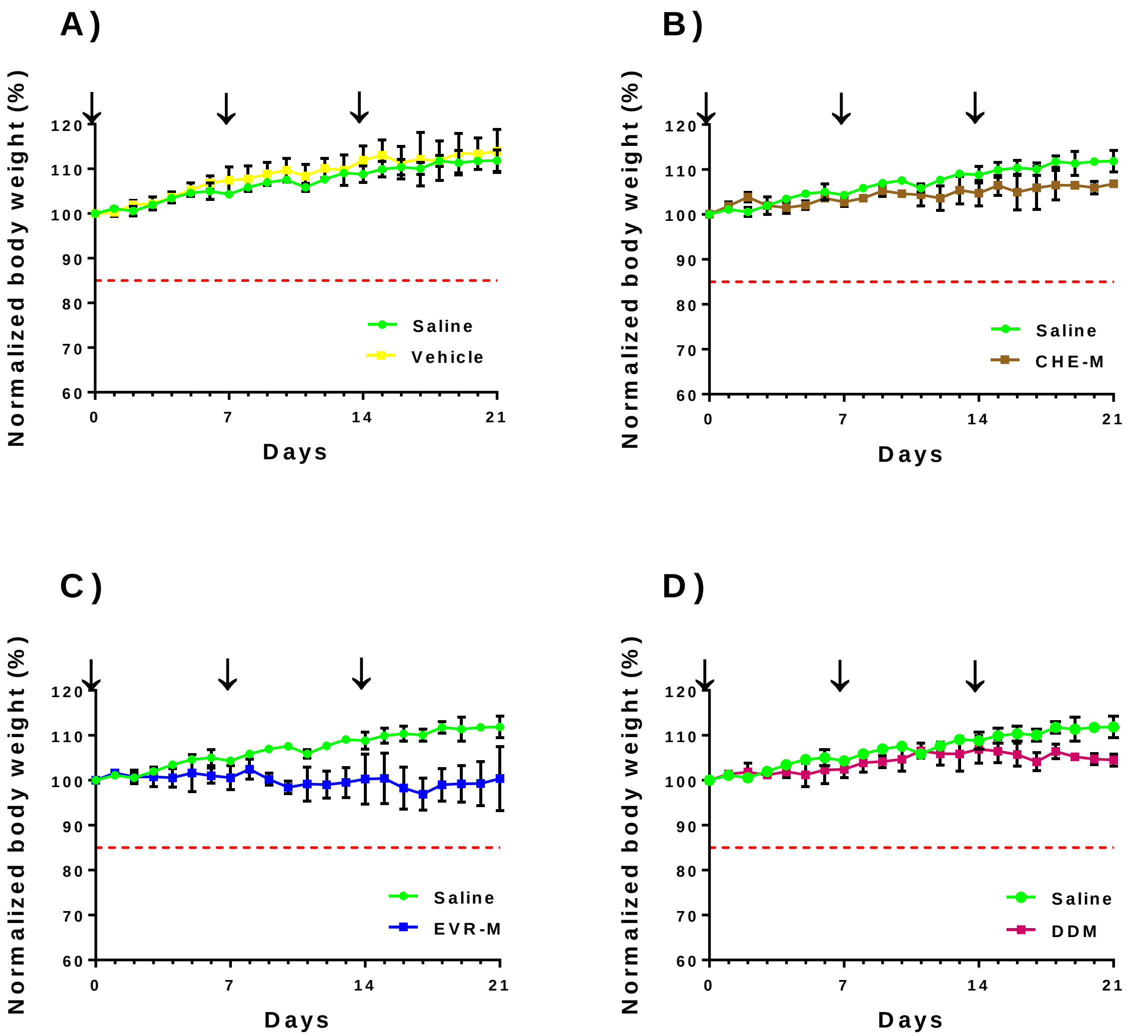

Figure 4.5: Monitoring body weight to access toxicity.

(a) Normalized body weight of mice over time after injections with individual or combination micelles of CHE & EVR on day 0, 7 and 14 as indicated by the arrows. The mice were injected with Saline as a negative control and Vehicle (empty micelles) **(b)** CHE-M **(c)** EVR-M **(d)** and DDM. The red dashed line represents the 15% limit for weight loss as an indication of toxicity.

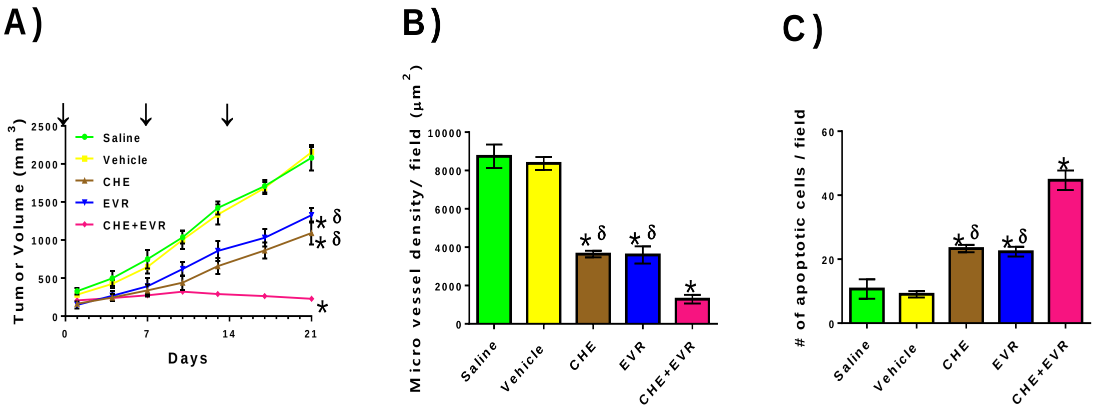

Figure 4.6: Efficacy of the micellar formulation.

(a) Xenograft tumor volume reduction in mice over time after i.v. injection of saline (control), Empty-M, CHE-M, EVR-M, or DDM with CHE at 0.5 mg/kg, and EVR at 25 mg/kg on days 0, 7, and 14 as indicated by arrows (n = 3/treatment, Mean ± SD), **(b)** quantification of micro vessel density in tumor tissue by counterstaining with anti-CD31 antibody, **(c)** quantification of apoptotic cells in tumor tissue by counterstaining with anti-Caspase3 antibody. * Represents significant difference from control (saline), δ represents significant difference from DDM (Mean ± SD, n=3). Significant differences between treatment group means is evaluated using one way ANOVA with Tukey's Multiple Comparison Test (compare all pairs of columns) using a significant level (α) of 0.05. Analysis is performed with GraphPad Prism version 5.04 for Windows, GraphPad Software, San Diego California USA.

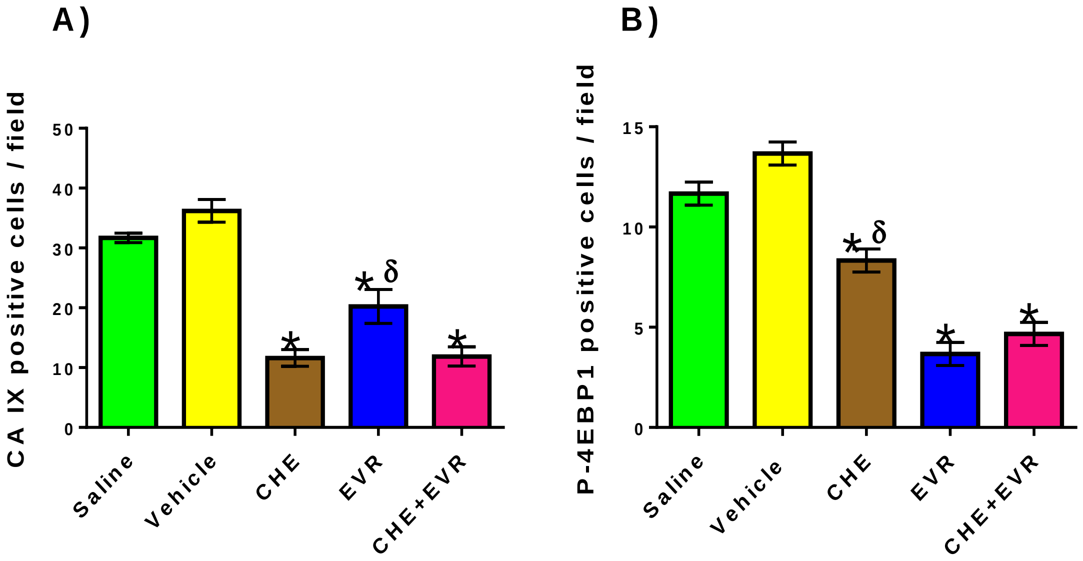

Figure 4.7: Mechanisms involved in tumor progression.

(a) Quantification of CAIX positive cells using anti-CAIX antibody for identifying the involvement of HIF pathway, **(b)** quantification of Phospho-4EBP1positive cells for mTOR pathway involvement by using anti-P-4EBP1 antibody in tumor tissue of mice injected i.v. with saline (control), Vehicle (empty micelles), CHE-M, EVR-M, or DDM with CHE at 0.5 mg/kg, and EVR at 25 mg/kg. * Represents significant difference from control (saline), δ represents significant difference from DDM (Mean ± SD, n=3). Significant differences between treatment group means is evaluated using one way ANOVA with Tukey's test (compare all pairs of columns) using a significant level (α) of 0.05. Analysis is performed with GraphPad Prism version 5.04 for Windows, GraphPad Software, San Diego California USA

Micelle	Fast $t_{½}$ (h)	Slow $t_{½}$ (h)	r^2
CHE	1.598	21.59	0.9881
EVR	1.644	37.90	0.9722
CHE Combination	1.493	24.82	0.9853
EVR Combination	1.494	27.99	0.9934

Table 4.1: Release parameters.

Fast and slow half-lives ($t_{½}$) and goodness of fit (r^2) values for CHE and EVR in individual and DDM using a two phase association curve fitting

CHAPTER 5

GENERAL CONCLUSIONS

The use of polyester diblock copolymers for drug delivery applications has tremendously increased courtesy of their wide range of applications. Certain properties of these copolymers such as chemical composition, molecular weight and size can be modified according to our needs thereby tailoring these corresponding micelles and nanoparticle structures for specific purposes. The size of these nanostructures makes them ideal candidates for delivery of therapeutic and hydrophobic moieties. The ability of these block copolymers to form well defined core-shell nanostructures upon aqueous exposure has huge potential and this attribute has been thoroughly exploited in developing various nanostructures that include micelles, nanoparticles, and polymersomes. The nanostructures can solubilize multiple drug moieties at therapeutically relevant concentrations thereby providing an opportunity to explore their therapeutic potential in treating metastatic diseases. These polyester structures are biodegradable and are already being tested in clinical trials. We have successfully developed a micellar and a nanoparticle system based on polyester diblock copolymers and we demonstrated their diagnostic and therapeutic applications hereafter.

High mortality rates associated with majority of the cancers is primarily because of the metastatic spread of the disease. Majority of the metastasis occurs through the lymphatic system wherein the treatment is given systemically thereby causing unwanted systemic toxicity. The inability to deliver therapeutic concentrations of drug moieties to the lymphatics eventually leads to the development of drug resistance. Nanostructures with certain parameters such as size < 100 nm and a slight negative surface charge have been reported to be selectively up taken into the lymphatics compared to neutral or positively charged particles. We therefore developed a PEG-b-PCL surface modified nanoparticle system that when injected subcutaneously accumulates specifically in the lymphatics and delivers multiple drug moieties simultaneously at therapeutic levels to significantly inhibit the melanocyte proliferation and thereby prevent further metastasis. We tested the efficacy of these nanoparticles in relevant metastatic melanoma mouse models. The surface properties of these nanostructures such as size and charge need to be adequately tailored to achieve locally acting nanoparticles or those that travel to distal sites within the lymphatics. The developed nanoparticle platform can be loaded with multiple hydrophobic moieties and can be used in the treatment of other diseases that metastasize through lymphatics. We have so far been successful in developing and characterizing this nanoparticle system but further work needs to be done in elucidating the biodistribution of these nanoparticles after subcutaneous injections *in vivo*.

mPEG-*b*-PLA micellar platform was developed to demonstrate the diagnostic applications of the micelles. Nerve damage occurs in majority of the surgeries due to lack of a contrasting agent. Traditional formulations for the delivery of fluorescent probes used DMSO in their formulation which caused unwanted toxicities. The delivery of BMB in our polymeric micellar biodegradable platform displayed enhanced accumulation in the nerves possibly due to the longer circulation times associated with polymeric micelles. The PEG coating of these micelles prevent their opsonization by macrophages and also increases their size such that they can no longer be excreted renally. The nerve highlighting micellar formulation is a first of its kind as no clinically approved nerve highlighting agents are available. This platform therefore has a potential clinical application in operating rooms for the delivery of various kinds of nerve highlighting fluorophores.

The mPEG-*b*-PLA platform can also be used for therapeutic applications wherein we incorporated two drug moieties that targeted the major pathways involved in ovarian cancer. These micelles after being injected i.v. selectively accumulate in the tumor site via the EPR effect, courtesy of their nano size. The combination of the incorporated drugs needs to be carefully selected so as to achieve synergistic effects in preventing cell proliferation. The aqueous solubilities of both drug moieties has been tremendously increased to therapeutic concentrations by incorporating them in the hydrophobic micellar cores.

In conclusion, micellar and nanoparticle structures developed from polyester diblock copolymer platforms have tremendous applications in the formulation industry and their diagnostic and therapeutic applications have been demonstrated in this work.